

INTERACTION OF SPHERICAL
PARTICLES OWING TO STEADY
STREAMING INDUCED BY
ULTRASOUND

Javeria Jalal

A thesis submitted for the degree of
Doctor of Philosophy

March 2018

Abstract

Steady streaming in a fluid is the generation of a mean flow by an acoustic wave. Any wave passing through a fluid causes to and fro oscillations of the fluid and any suspended particles. According to linear theory, there is no net displacement of the fluid or particles after the passage of each wave. However, it is known theoretically and experimentally that a non-linear effect creates a mean flow. The flow is created by the viscous forces, and non-zero time-averaged values of the quadratic acoustic terms arising in the equations of conservation of momentum.

The main objective of this study is to find out the role of steady streaming once two spheres come close to each other, in making them attract or repel. This work involves solution of the Navier-Stokes equation for an incompressible fluid using two numerical methods: a Direct Numerical Simulation (DNS), based on a spectral element method, and a Weakly Non-linear Formulation (WNF), based on a finite element method.

First, a single sphere problem was modelled and compared qualitatively and quantitatively against the literature using DNS. Then, the results

using WNF and DNS were also compared, qualitatively and quantitatively. The comparison was made in terms of size of the inner vortices, and peaks of drag coefficients, for increasing Reynolds number. These results compare well with the works of Blackburn (2002), and Klotsa (2009), for different ranges of parameters involved: i.e. the Reynolds number, $Re = \frac{A\omega D}{\nu}$, and the relative amplitude of the oscillation of the sphere, ϵ . Here, A and ω are the amplitude and frequency of the oscillating flow, respectively, D is the diameter of the sphere, and ν is the kinematic viscosity.

Results for a wider range of parameters than in previous studies i.e. $1 \leq Re \leq 500$ and $0.01 \leq \epsilon \leq 5$, have been obtained using the DNS. These results were classified into various regimes that were laid out by Riley (1967). Few results have been published on steady streaming generated for amplitudes $\epsilon > 1$. DNS data showed presence of a different flow regime for high amplitudes $1 \leq \epsilon \leq 5$.

However, DNS is limited to steady flows around a single sphere unless it is extended to three dimensions. This extension is likely to be very time consuming. In comparison, the task of computing steady streaming flows around single and two spheres can be achieved much more quickly using WNF. It has the added flexibility of imposing oscillation at any given angle to the axis on which the spheres are placed.

For steady streaming around two spheres, a new problem was defined along with its set of parameters. WNF was used to obtain the results in three different configurations, depending on the alignment of the spheres with respect to the axis of oscillation. The new parameters are: L , the dis-

tance between centers of the two spheres, θ , the angle between the axis of oscillation and the axis joining the centers of the spheres, and Stokes number, $\Omega = \frac{\omega D^2}{4\nu}$. It was possible to visualize the flows, as well as calculate the forces exerted on the spheres by steady streaming. The most important out of the three configurations discussed turned out to be the lateral configuration, in which the spheres are positioned perpendicular to the axis of imposed oscillation. When the spheres are placed in the lateral configuration, it was found that the spheres attract each other for high frequencies and repel for low frequencies. For intermediate frequencies, the spheres stay at an equilibrium distance apart.

Based on the forces thus calculated, trajectories of the spheres were computed, mainly to find out initial conditions that would lead the spheres to touch, and the time it took, for the practical application noted below. Trajectory paths for $0.1 \leq \Omega \leq 100$ were calculated, when the angle θ_0 and spacing L between the spheres were allowed to vary between $0^\circ \leq \theta_0 \leq 360^\circ$ and $1 \leq \frac{L}{D} \leq 20$. If Ω is considered to be a measure of the size of the particles, it was found that spheres of large size attract and touch each other. The spheres of small size repel and stay suspended in the fluid.

This research is part of an ARC linkage project with Geoffrey Gardiner Dairy Foundation, where the dairy industry is interested in milk fat separation using ultrasound. For the dairy industry, skimming milk fat from milk is very important. Milk fat content in milk may vary depending on the source it is coming from and on the season as well. To make sure that the

percentage of milk fat is the same in all packages of a certain product, the industry has to skim milk first and then re-add it in the desired quantity, for each and every product. The current technology involves use of centrifuges whereas the use of ultrasound can perform the same job involving simpler devices that have no moving parts. The ultrasound is applied by piezoelectric transducers. An application of the present thesis is to investigate how the steady streaming affects tiny fat particles, Milk Fat Globules (MFGs), to make them attract or repel each other. If attraction of the particles causes them to touch, then they will rise out of milk faster, which is the desired outcome. It was found experimentally that particles of small size do not get removed from milk Leong *et al.* (2016). In this work, an explanation for why the smaller sized particles stay suspended in the milk has been achieved. Furthermore, theoretical and computational methods have been developed that permit ultrasonic separation processes to be designed with less reliance on trial-and-error experimentation.

Acknowledgments

Alhamdulillah, I am blessed to be able to witness this proud moment in my life.

Firstly, I would like to thank my supervisors Richard Manasseh and Justin Leontini who have been exceptionally co-operative and kind from the very first day. I have nothing but respect for you for how supportive you have been to make it all easy for me. I have learned by observing you about almost every aspect of life. It has changed the way I think and perceive things. Also, I must mention the rest of the team involved in the project; Linda Johansson, Thomas Leong, Sally McArthur at Swinburne, Pablo Juliano, Raymond Mawson, Kai Knoerzer at CSIRO, and Aaron Gosling at Geoffery Gardiner Dairy Foundation (GGDF), who have been very helpful and considerate with an inexperienced PhD student during our weekly and bi-monthly meetings. I would like to acknowledge Faculty of Science, Engineering and Technology at Swinburne for providing the support and financial resources in the form of Faculty Scholarship and HDR Support funding.

It has been a tough time leaving my city for the first time to move overseas and settle here for a new learning experience. I would not have done it without my friends at Swinburne. Special thanks to Sabah, Hasnat and

Abbey, who have been there for me whenever I needed help in any respect. We have a special bond that is going to last for sure. I would like to mention Afsana, Maimuna, Ferial, Sarah, Yasmin, Zubeda, Afia and Wajeeha who are part of our famous “Break from study” group, where we could share little joys in life apart from the stressful PhD life. All those little discussions about the candidature helped resolve many issues that came along during these four years. Another special group of friends, Shafqat, Neelofar, and Sehrish, who made this part of the world feel like a home away from home. We have spent amazing time together and will hold delightful memories for life.

Last but not the least, it is all because of the efforts and prayers of my parents, family and my new family in the form of in-laws. I owe gratitude to my husband, Tahir, who has sacrificed so much for the sake of my studies since the day we are related. We have been through thick and thin and I fully acknowledge that without your support, I would not have made it.

Declaration

The work presented in this thesis entitled “Interaction of spherical particles owing to steady streaming induced by ultrasound” has been carried out in the Department of Mathematics at Swinburne University of Technology in Melbourne between March 2013 and May 2017. The thesis contains no material that has been accepted for the award of any other degree or diploma. To the best of my knowledge, the thesis contains no material previously published or written by another author, except where due reference is made in the text of the thesis.

A handwritten signature in cursive script, reading "Javeria", enclosed within a thin rectangular border.

Javeria Jalal

May, 2017

Contents

List of Figures	xii
List of Tables	xxii
1 Introduction	2
1.1 Background	2
1.2 Types of Streaming in Fluid	3
1.2.1 Acoustic streaming effects	4
1.2.2 Steady streaming effects	6
1.2.3 Radiation force effects	7
1.2.4 Multiple scattering effects	9
1.2.5 Summary	10
1.3 Motivation: Milk Separation Project	11
1.4 Thesis Outline	13
2 Literature Review	15
2.1 Introduction	15
2.2 Steady Streaming around Single Oscillating Spheres	16
2.3 Steady Streaming Flow around Two Spheres	26

2.4	Transport and Organization of Multiple Particles	28
2.5	Review Summary	31
3	Methodology	34
3.1	Introduction	34
3.2	The Governing Equations	35
3.2.1	Non-dimensionalization of the Navier-Stokes equations	36
3.2.2	Dimensionless parameters	38
3.3	Numerical Methods Employed	40
3.3.1	DNS: Direct Numerical Simulation	42
3.3.2	WNF: Weakly Non-linear Formulation	48
3.4	Summary	53
4	Verification of DNS for a Single Sphere	55
4.1	Introduction	55
4.1.1	Model for steady streaming around a single sphere . . .	56
4.2	Comparison of DNS with Literature	56
4.2.1	Comparison of DNS with Blackburn (2002)	59
4.2.2	Comparison of DNS with Alassar (2008)	62
4.3	Steady Streaming Flows in Relative and Absolute Frames . . .	64
4.3.1	Streaming flow around a stationary sphere in an oscillatory flow	66
4.3.2	Streaming flow around an oscillatory sphere in a quiescent flow	67
4.4	Summary	68

5	Steady Streaming around a Single Sphere using DNS and WNF	70
5.1	Introduction	70
5.1.1	Model for steady streaming around a single sphere using WNF	71
5.2	Comparison of Results from WNF with DNS	73
5.2.1	Comparison of size of the inner vortices	74
5.2.2	Comparison of peak coefficients of drag	77
5.3	Classification of Flow Regimes	80
5.4	Summary	82
 6	 Steady Streaming around Two Spheres	 86
6.1	Introduction	86
6.2	Numerical Setup	87
6.3	Verification of Results for Two Equisized Spheres	88
6.3.1	Streaming flows around two spheres	91
6.3.2	Discussion	101
6.4	Summary	102
 7	 Trajectories of Oscillating Spheres	 104
7.1	Introduction	104
7.2	Method Employed for Calculating Trajectories of Oscillating Spherical Particles	105
7.2.1	Algorithm for integration of forces	106
7.2.2	Tracing trajectories of spherical particles using streaming forces	107

7.3	Validity of the Numerical Model Employed for Calculating Trajectories	108
7.4	Trajectories of Two Equisized Oscillating Spheres	111
7.4.1	Estimating particle behaviour around conditions leading to equilibrium	113
7.4.2	Trajectories of particles in milk separation	117
7.5	Summary	118
8	Conclusion	120
	Bibliography	124

List of Figures

2.1	A quadrupole-like streaming around a linearly translating particle when the particle is moving vertically. The image is reproduced from Longuet-Higgins (1998), by permission of the Royal Society.	17
2.2	Sketch of the inner streaming vortices around a horizontally vibrating cylinder and a spherical particle. Reprinted with permission from Lane (1955). Copyright 1955, Acoustic Society of America.	18
2.3	Streamlines of flow around a single sphere oscillating in a vertical direction for (a) $Re \ll 4\Omega \ll 1$, and (b) $4\Omega \gg 1$ and $Re_s \ll 1$. Reproduced from Riley (1966) by permission of Oxford University Press.	21
2.4	Steady streaming around a sphere oscillating vertically. $L = 1.4$ cm is the radius of the sphere. Reprinted with permission from Springer Nature, Kotas <i>et al.</i> (2006), Copyright 2006. . .	23

2.5	Parameter spaces for various studies conducted for steady streaming flows around a single sphere, where the entire domain shown is the parameter space used in this study. Re_s is the product, and M^2 is the ratio of dimensionless parameters Re and ϵ , respectively. The shaded regions for Riley (1966, 1967) is depicting region where $\epsilon \ll 1$	32
3.1	Schematic of the one sphere problem for the DNS.	42
3.2	Spectral element mesh developed similar to that used by Blackburn (2002). Size of the elements is measured in terms of diameter of the sphere D . The colored edges of the mesh depict the boundary conditions explained in section 3.3.1. The sphere is positioned at the center of the bottom boundary, but is difficult to see due to the large size of the domain. (Inset) Detail of mesh around the sphere with fewer elements than that were actually used in the mesh, to depict the structure of the cells adjacent to the sphere.	44
3.3	Schematic of the two sphere problem adapted from Fabre <i>et al.</i> (2017).	48
3.4	Half of the axisymmetric mesh generated for a single sphere using FreeFem++. The green inner region is more refined than the outer region. The center of the mesh is zoomed in the inset.	52

3.5 Two-dimensional mesh for two spheres placed in a lateral configuration at the center of the domain, generated using FreeFem++. The green inner region is more refined close to the spheres than the outer region. 53

4.1 Streaming flows generated using DNS showing size of the inner vortices for a) $Re = 20$, when $\epsilon = 2.00$, and b) $Re = 100$, when $\epsilon = 0.25$. The flow is oscillating in the axial direction depicted by the bold black arrow. Rings of vortices are formed in a direction perpendicular to the axis of oscillation, along the axis of symmetry, which when sliced through a plane shows up as a pair of vortices. The colour represents azimuthal component of vorticity relative to the plane of the page, ranging from -0.01 (blue, directed inwards) to 0.01 (red, directed outwards). 57

4.2 (Top) Mean velocity field showing steady streaming beyond the boundary layer region of a sphere, for dimensionless parameters $Re = 200$, $\epsilon = 0.25$. The colour contour represents azimuthal component of vorticity relative to the plane of the page, ranging from -1 to 1 . The black arrow represents axis of oscillation of the fluid in the axial (x -) direction. The streamlines start at user-selected points. (Bottom) Qualitative comparison of simulation (above) with theoretical predictions of Lane (1955) using relevant half of Figure 2.2. Reprinted with permission from Lane (1955). Copyright 1955, Acoustic Society of America. 58

4.3	Comparison of peak coefficients of drag force, C_d , for a sphere which is placed stationary in an oscillating flow. Blackburn (2002); - \blacklozenge , DNS; $\text{---}\bullet$. For $\epsilon \leq 1$, both numerical methods match Basset (1888).	59
4.4	Location of the first zero-crossing of radial velocity on the line $x = 0$, r_{cross} , as a function of Reynolds number Re , for $\epsilon=0.05$, and $\epsilon=5.0$. Blackburn (2002); $\text{---}\bullet$ $\epsilon = 0.05$, $\text{---}\bullet$ $\epsilon = 5.0$. DNS; \bullet $\epsilon = 0.05$, \bullet $\epsilon = 5.0$	60
4.5	d_b denotes the size of inner vortices varying with θ , and measured from the center of the sphere. Here, $\epsilon = 0.5/S$, where S is the inverse Strouhal number. This Figure will be used to make a comparison with the results in Figure 4.6. Reprinted from Alassar (2008), Copyright (2008), with permission from Elsevier.	62
4.6	Size of the inner vortex, r_{cross} , measured (above) over the x -axis corresponding to $\theta = 0^\circ$, and (below) over the r -axis corresponding to $\theta = 90^\circ$. Alassar (2008); $\text{---}\bullet$ $Re = 25$, $\text{---}\bullet$ $Re = 200$. DNS; $\text{---}\blacklozenge$ $Re = 25$, $\text{---}\blacklozenge$ $Re = 200$	64
4.7	Streaming around a sphere in an oscillating flow, for $Re = 50$, $\epsilon = 0.20$. The contours represent azimuthal component of vorticity.	66
4.8	Mean streaming for a sphere oscillating in a quiescent flow initially, for $Re = 50$, $\epsilon = 0.20$. The contours represent azimuthal component of mean vorticity.	67

4.9 Comparison of peak coefficients of drag force, C_d , for a sphere oscillating in a quiescent flow. Blackburn (2002); - \blacklozenge , DNS; $\text{---}\bullet$. For $\epsilon < 1$, both numerical methods match Basset (1888). 68

5.1 Steady streaming around a single sphere oscillating in the direction of the bold black arrow, for $\Omega = 1$ (left), and $\Omega = 100$ (right), using WNF. Recall that the basis of WNF is that $\epsilon \rightarrow 0$. Rings of vortices form perpendicular to the axis of oscillation and show up as a pair of vortices when sliced through in two-dimensions. The contours represent the azimuthal component of vorticity, as explained in section 4.1.1. 71

5.2 Flows generated using: (left) DNS for $\text{Re} = 100$, when $\epsilon = 0.25$, and (right) WNF for $\Omega = 100$, when $D = 1$ in both cases. Contours represent azimuthal component of vorticity as described in section 4.1.1. Streamlines are generated from user-selected points, hence can not be exactly replicated in another attempt. The bold black arrow depicts the imposed oscillating flow in the axial direction. Recall that WNF is based on infinitesimal amplitude, however, vorticity in the flow can be scaled. The aspect ratio of the images was made slightly different so that the spheres would appear of the same size, owing to the use of axisymmetric and Cartesian domains for the DNS and WNF respectively. 74

5.3 Symbols denoting DNS data for length of inner vortices, r_{cross} , plotted against Ω , and its comparison with WNF data. (above) Parallel to the direction of the imposed oscillation (x -axis); (below) perpendicular to the direction of the imposed oscillation (over the r -axis). (Insets) Same plots for $40 \leq \Omega \leq 600$ 75

5.4 Comparison of peaks of drag coefficients C_d for DNS and WNF, when a stationary sphere is placed in an oscillatory flow. As ϵ is reduced, the DNS results tend to the WNF result where $\epsilon \rightarrow 0$ 77

5.5 Comparison of peaks of drag coefficients, C_d , for DNS and WNF, for an oscillating sphere placed in a quiescent flow. Parts of DNS curves for $\epsilon = 0.01$ and $\epsilon = 0.05$ are overlapping each other. 78

5.6 The comparison of DNS data on a log-log plot and a semi-log plot of r_{cross} as a function of Ω replicating variables defined by Klotsa (2009). (Inset) The same plot on a log-log scale for the range of data presented in Klotsa (2009). Klotsa (2009), $75/\Omega$; - -, Kotas *et al.* (2006), $46/\Omega$; - - 79

5.7 Distributing flow regimes into zones, explained in Table 5.2, according to different trends followed by the steady streaming flow simulated around a sphere in an oscillating flow using DNS, and its comparison with WNF. Recall from section 5.2.1 that WNF is only comparable for $25 < \Omega < 60$ 83

5.8	Steady streaming around a single sphere in four different zones when the imposed flow is oscillating in the direction of the bold black arrow. Colour represents azimuthal component of vorticity, between -0.01 (blue) to 0.01 (red), as described in section 4.1.1.	84
6.1	Schematic of the two sphere problem as shown in Figure 3.3. .	87
6.2	Pressure isolevels, between -0.01 (blue) to 0.01 (red), for $\Omega = 1$ in the (a) lateral, (b) axial, and (c) oblique configurations, when $L/D = 2$	88
6.3	Pressure isolevels, between -0.01 (blue) to 0.01 (red), for $\Omega = 100$ in the (a) lateral, (b) axial, and (c) oblique configurations, when $L/D = 2$	89
6.4	Time-averaged force, F_L , as a function of space between the spheres, L/D , after normalizing the parameters defined by Klotsa <i>et al.</i> (2007). Klotsa; $\text{---}\bullet$, (WNF) $\Omega = 17.85$; $\text{---}\bullet$. Positive and negative F_L represent attraction and repulsion between the spheres, respectively. The WNF curve is rescaled for a comparison.	90
6.5	Equilibrium distance between the center of the spheres, L/D , as a function of frequency, Ω , in a lateral configuration, when spheres are positioned perpendicular to the axis of imposed oscillation. The total number of data points is 43.	91

6.6 Steady streaming around two spheres in a lateral configuration, when $L/D=2$. The imposed flow is oscillating in the direction of the bold black arrow. Colour represents azimuthal component of vorticity -0.01 (blue) to 0.01 (red). 93

6.7 Steady streaming around two spheres in an axial configuration, when $L/D=2$. The imposed flow is oscillating in the direction of the bold black arrow. Colour represents azimuthal component of vorticity between -0.01 (blue) to 0.01 (red). . . 95

6.8 Steady streaming around two spheres in an oblique configuration, when $L/D=2$. The imposed flow is oscillating in the direction of the bold black arrow. Colour represents azimuthal component of vorticity between -0.01 (blue) to 0.01 (red). . . 97

6.9 Forces, F_{TT} , F_{AA} , and F_{AT} , exerted on spheres by steady streaming in the (a) lateral configuration, (b) axial configuration, and (c) oblique configuration, respectively, as a function of distance L/D in between them for different values of Ω . The equilibrium distance occurs whenever a force curve crosses 0.0. 99

6.10 Distance where net force experienced by the sphere(s) is zero
i.e. the equilibrium distance as a function of Ω , in a lateral
configuration. The black horizontal line shows where the two
spheres touch, at $L/D = 1$. The solid line, —, shows the
location of the stable equilibrium for the intermediate values
of Ω . If the two-sphere flow could be found by simply super-
imposing the flows around two individual spheres, this curve
would coincide with the dashed line, - -, the distance to the
stagnation point in the single sphere case. 100

6.11 Attraction between two spheres changing to a repulsion for
 $\Omega = 5$ in a lateral configuration. Colour represents pressure
 -0.05 to 0.05 . The imposed flow is oscillating in the direction
of the bold black arrow. 102

7.1 Trajectories when a small velocity in the axial direction is
added, for $\Omega = 4$. (a) Undisturbed case, where $U_{Stream} \simeq$
 $\mathcal{O}(10^{-3})$, (b) velocity of 10^{-6} added, and (c) velocity of 10^{-5}
added. 109

7.2 Comparison of the streaming and particle velocities, U_{Stream}
and $U_{Particle}$, respectively, when $L_0 = 2.3D$, and $\theta_0 = \pi/2$ rad.
 $U_{Particle}$ is measured for a time $t = 0.015$ 110

7.3 (a) Trajectories of spheres over dimensionless time, t , for frequencies $0.10 \leq \Omega \leq 100$, when $L_0 = 1.836$ and $\theta_0 = \pi/2$ rad i.e. lateral configuration. The black horizontal dashed line shows $L/D = 1$. (b) Time, t_{MIN} , taken to reach the absolute minimum L_{MIN} for $L_0 = 1.836$ and $\theta_0 = \pi/2$ rad. 112

7.4 Contour plot for L_{MIN} showing convergence and divergence trends for $\Omega = 5$, for a range of L_0 and θ_0 close to the point of equilibrium $L_0 = 1.836$ and $\theta_0 = \pi/2$ rad, represented by black circle. 114

7.5 Force, F_{TT} , for $\Omega = 5$. The first equilibrium is at $L/D = 1.926$ and, the second, at $L/D = 3.2$ for the smoothed force (reducing noise). (Inset) Data extracted out of Figure 7.4, along $\theta_0 = \pi/2$ rad. 115

7.6 Contour plot for L_{MIN} trends for $\Omega = 10$, for a range of L_0 and θ_0 showing mostly convergent trend close to the corresponding point of equilibrium $L_0 = 0.630$ and $\theta_0 = \pi/2$ rad. 116

7.7 Trajectories of spheres over dimensionless time, t , for frequencies $0.10 \leq \Omega \leq 100$, when $L_0 = 2.3$ and $\theta_0 = \pi/2$ rad i.e. lateral configuration. The black horizontal dashed line shows $L/D = 1$. $L_0 = 2.3$ is equilibrium distance for $\Omega \approx 4$ 118

1 Vibration of particles, X , with mass ratio, m , when $\epsilon = 0.05$. . 136

List of Tables

3.1	List of variables used in section 3.2.1	37
3.2	Meshes used for mesh analysis, M1 – M5, along with the total number of elements comprising them. The parameters varying in these meshes are length of the square, number of layers of elements from circle to the square, length of the domain upstream and downstream of square rear edge, number of elements from square front/rear edge to inlet/outlet, and number of total elements in the mesh, respectively.	45
3.3	The distance from the surface of the sphere to the stagnation points, r_{cross} , measured using DNS with different meshes for a single sphere, M1 – M5 given in Table 3.2, for $Re = 1$, $Re = 40$, and $Re = 100$ when $\epsilon = 0.05$ and $\epsilon = 5.0$. Some meshes were under resolved and thus could not come up with a value of r_{cross}	45
3.4	Maximum drag force, F_d , measured using DNS with different meshes for a single sphere, M1 – M5 given in Table 3.2, for $Re = 1$, $Re = 40$, and $Re = 100$ when $\epsilon = 0.05$ and $\epsilon = 5.0$. . .	46

3.5	r_{cross} measured using DNS with mesh M4 given in Table 3.2, for $\epsilon = 0.05$ and $\epsilon = 1.00$, when n_T and n_{Av} are varied. Here, n_T is the number of periods before averaging, and n_{Av} is the number of periods over which the averaging is done.	46
3.6	F_d measured using DNS with mesh M4 given in Table 3.2, for $\epsilon = 0.05$ and $\epsilon = 1.00$, when n_T and n_{Av} are varied. Here, n_T is the number of periods before averaging, and n_{Av} is the number of periods over which the averaging is done.	47
3.7	Meshes used for mesh analysis, M1 – M5 , along with the parameters used, where r_{in} , r_{out} , n_{in} and n_{out} represent the radii and number of elements used for the inner and outer meshes, respectively.	52
3.8	Forces measured using WNF with different meshes, M1 – M5 given in Table 3.7, for $\Omega = 0.1$ and $\Omega = 100$. F_{AA} , F_{TT} , and F_{AT} are as defined in section 3.3.2.	53
5.1	Parameter space used for both the DNS and WNF. As defined in section 2.2, $4\Omega = Re/\epsilon$, $Re_s = \epsilon Re$, and $\delta = \sqrt{\nu/\omega}$	72
5.2	Distribution of oscillatory flow regimes around a single sphere into zones.	82

Chapter 1

Introduction

1.1 Background

Fluctuations in a fluid can be generated either by a wave or an applied oscillating body force. When a fluid is subjected to enforced oscillations, a net mean flow is generated (Riley, 2001). It is a non-linear effect. According to linear theory, there is no net displacement of the fluid or particles after the passage of each wave. However, it is known theoretically and experimentally, that in the presence of a source a non-linear effect creates a mean mass flow (Nyborg, 1953; Riley, 2001). Regardless of how this mean flow is generated, a non-zero time-averaged flow in the fluid is termed steady streaming, a term that will be clarified in the text that follows. A brief history of the streaming phenomenon and its various types are given in the next section.

1.2 Types of Streaming in Fluid

The first thorough theoretical description of streaming in a Kundt's tube was given by Lord Rayleigh in 1883, where he explained streaming for a standing wave between two parallel walls. His analysis showed that the motion of air was caused by a non-linear second-order effect (Rayleigh, 1883). In a lecture on the topic of acoustic streaming, Lighthill (1978) emphasised that this streaming, which he termed 'Rayleigh's law of streaming', was applicable to two kinds of streaming:

- (a) 'acoustic streaming' induced by standing waves, that was associated with the attenuation of the sound waves through the fluid owing to viscosity,
- (b) 'steady streaming' as a result of a solid body oscillating in a fluid at rest, due to friction at its boundary (Riley, 1967).

Lighthill (1978) also mentioned that it was Stuart (1966) who did the pioneering work for calculating streaming based on Rayleigh's law of streaming.

The same non-linear phenomenon is responsible for the formation of rip currents in the ocean (Mei, 1985). In another context, acoustic streaming in liquids may play a crucial role in the hearing process due to time independent motion induced in the cochlear fluid within the ear (Lighthill, 1991).

Zaremba (1971) identified three types of acoustic streaming according to the length of the scale of streaming:

- Eckart Streaming

- Rayleigh Streaming
- Schlichting Streaming

These are phenomena in which particles move relative to the fluid. However, there are also phenomena occurring between particles owing to an oscillatory body force. Each one of these effects are discussed in the following subsections.

1.2.1 Acoustic streaming effects

The history of studies of acoustic streaming dates back more than a hundred years. Though there is a substantial amount of theoretical work available now, experiments were carried out to study such phenomena long before that.

From among the very first experimenters, Faraday (1831) conducted an experiment with a vibrating plate, arranged as in Chladni's experiments Chladni (1787), in 1831. He explained the formation of a boundary layer by the interaction of vibrations of the plate with the air at the surface. Dvořák (1876) also observed air currents corresponding to the formation of dust figures.

Although the air motion due to vibration phenomena had been observed by these individuals, there had been no mathematical explanation offered. The first theoretical description was given by Rayleigh in his book 'Theory of sound' (Rayleigh, 1894). This type of streaming owes its origin to shear viscosity in the thin Stokes boundary layer in the vicinity of a solid boundary and is referred to as 'Rayleigh streaming'.

‘Rayleigh streaming’ or *outer streaming* is the streaming in the main bulk of the fluid, outside the boundary layer. There is another type of streaming cell inside the boundary layer, called *inner streaming*. In his analysis, Rayleigh (1883) did not include the details of inner acoustic streaming that drives the outer streaming. Schlichting (1955) gave the first mathematical model for inner streaming which he explained as a steady boundary layer vorticity, known as ‘Schlichting streaming’. This powerful inner boundary layer streaming flow then generates counter rotating streaming vortices within the main body of the fluid, accordingly named outer streaming, as already defined. This concept of combined inner and outer streaming in an incompressible flow was given by Stuart (1966) (termed ‘Stuart streaming’ by Lighthill (1978)).

Streaming observed in the main body of the fluid, when it is penetrated by an ultrasonic sound beam with a high amplitude, is termed the ‘quartz wind’. This time-averaged flow is caused by the dissipation of acoustic energy in the fluid owing to its viscosity. Although earlier observations of the quartz wind were made by Meissner (1926) in liquid and Walker & Allen (1950) in air, Eckart was the first one who gave a mathematical analysis for the quartz wind. Eckart (1948) showed that the quartz wind is caused by the viscous attenuation. ‘Eckart streaming’ can be generated both in standing and travelling waves.

In addition to his contributions on rectifying misconceptions about acoustic streaming, included at the beginning of this section, Lighthill (1978) also studied the difference between the Lagrangian and Eulerian mean motion in the acoustic streaming.

All the discussion above concerns an incompressible fluid. However, in reality, it is the compressibility of the fluid that allows sound to pass through it. Since particle size is assumed to be very small in comparison to wavelength of the stationary acoustic wave, fluid immediately around the particles can be assumed to be incompressible.

1.2.2 Steady streaming effects

Following Rayleigh and Lighthill, Riley (1967) gave a theoretical description of time-averaged streaming flows in incompressible fluids. In order to incorporate flows in incompressible fluids, the assumption was made that particle size has to be very small in comparison to the wavelength of the sound applied. The term ‘steady streaming’ was first coined by Riley (1967, 1997, 2001), who noticed that the origin of streaming in both cases (a) and (b) described in section 1.2 was *attenuation*. Riley (2001) clarified the need for a term in place of ‘acoustic streaming’, as it is used for cases with a certain degree of compressibility of the fluid. He kept the term ‘steady streaming’ for the time-averaged, incompressible flow above and beyond the Stokes drift velocity.

In this thesis, all time-averaged non-linear flows are henceforth defined to be what Riley (2001) termed *steady streaming*.

In a theoretical study, Davidson & Riley (1971) investigated steady streaming in the vicinity of a drop, or bubble (alternatively known as ‘cavitation microstreaming’). Longuet-Higgins (1998) extended the work of Davidson & Riley (1971). His study showed that if a single bubble is going through

translational and radial oscillations simultaneously, it would enhance the steady streaming. The translational oscillations are motion along a single axis while the radial oscillations are volume pulsations of a bubble. Also, he found that in the later case the streaming pattern was dipole-like. It is more quadrupole-like if the bubble moved only translationally (as shown in Figure 2.1 in the next section). As compared to Davidson & Riley (1971), who covered several situations in respect to the relative orders of magnitude of the two dimensionless parameters ϵ , the ratio of the vibration amplitude to the diameter of the sphere, and M^2 , the ratio of diameter of the sphere to the viscous length (to be explained in section 3.2.2), Longuet-Higgins (1998) considered only the case when these parameters are both $\ll 1$.

1.2.3 Radiation force effects

Another net motion phenomenon in a fluid subject to a sound wave, is when rigid or compressible particles (such as bubbles) are made to move relative to the fluid under the effect of acoustic radiation forces. After a discovery of mutual interactive forces on gas bubbles by Bjerknes (1906), many authors investigated types of acoustic radiation forces, both experimentally and theoretically.

As mentioned earlier, Acoustic Radiation Forces (ARFs) were noticed experimentally in air long before King (1934) first described them theoretically for incompressible particles. Radiation “pressure”, as defined by King, is a second-order, non-linear force that acts on a particle immersed in an acoustic field due to the transfer of momentum from the acoustic wave to

the particle. Here, as in all acoustic particle separation problems, the small parameter is ϵ or is proportional to ϵ . It was also found that the ARF will be orders of magnitude stronger in a standing wave field compared with that in a travelling wave field. King studied rigid spheres in an ideal fluid, and measured magnitudes of forces acting on them. In a standing wave field, the spheres were found to drift towards the nodes or antinodes, depending upon the difference between the density of the sphere and the fluid it is submerged into.

Yosioka & Kawasima (1955) went further to extend this theory for the effects of particles of finite compressibility in an inviscid fluid. Gor'kov (1962) added the effects of viscosity and thermal conductivity, also taking care of particle compressibility, into King's work.

A non-zero pressure gradient can couple with bubble oscillations to produce a translational force on the bubble, called the *primary Bjerknes force*. It is named after Bjerknes, who first reported the principle of such forces for bubbles (Bjerknes, 1906). The primary Bjerknes force drifts bubbles in the same way as the King's acoustic radiation force for rigid spheres. It was Leighton (1990) who gave a formulation as well as a graphical illustration of the response of a spherical bubble to a periodic pressure field in an incompressible liquid in terms of the Rayleigh-Plesset equation (or RPNP, named after Rayleigh, Plesset, Noltingk, Neppiras and Poritsky). He also explained how, in a standing-wave field, bubbles of less than resonant size travel up a pressure gradient towards the pressure antinodes, and those larger than resonance size travel down the gradient to the nodes. Here, the resonance size refers to the size of the bubble for which the amplitude of oscillation is

maximum for a given forcing frequency.

The time-averaged interaction force between two particles is called the *secondary Bjerknes force* for bubbles and *König force* for solid spheres (König, 1891). For this interactive force, the size of the particles was considered much smaller than the distance between them, that in turn was smaller than the wavelength of the imposed acoustic field.

To summarize, in an acoustic field, the *primary* forces drive the particles to accumulate at the pressure nodes or antinodes of a standing wave, and the *secondary* forces are responsible for their mutual attraction or repulsion, and a possible formation of a particle structure.

Doinikov (2003) presented a major review of theoretical work on the topic of radiation forces. He included the cases of acoustic radiation and interactive forces on single particles, between two bubbles, bubble and a solid particle, bubble and a liquid drop, two rigid spheres, and N compressible spheres in a compressible fluid.

1.2.4 Multiple scattering effects

Previous results for single particles assumed the separation distance between the bubbles to be large in comparison with the bubble sizes (Bjerknes, 1906). When two compressible particles are placed so close to each other that the distance between them is comparable to their sizes, the reflection of the applied sound field is not negligible. This process of reflection of the sound field off the particles is known as multiple scattering. The first attempt to take multiple scattering into account was made by Zavtrak (1987). It

was found that at such small distances between two equal sized bubbles the magnitude of the mutual interaction force is substantially different from that given by Bjerknes' theory.

Doinikov & Zavtrak (1995) calculated an expression for mutual interactive forces for two pulsating gas bubbles incorporating multiple scattering effects. The surrounding liquid around the bubbles was assumed to be incompressible and inviscid. Also, very small-amplitude acoustic waves were considered so the non-linear effects were neglected. They also discussed interactions among bubbles of different and similar sizes along with comparisons of physical aspects of each phenomenon. The mechanism behind the formation of the phenomenon of stable “bubble grapes” (observed in Kobelev *et al.* (1979)) was explained, when both bubbles were larger than their resonance sizes.

1.2.5 Summary

Various types of large and small scale streaming were introduced in this section so far, with special emphasis on streaming and other interactive effects around the particles submerged in a fluid. An attempt was made to remove confusion in the terminology used in the literature for the steady streaming phenomenon. The objective of this work involves investigation of the role of steady streaming forces in particular, in bringing the particles to touch. The motivation behind this study is an application of this work and is given in the next section.

1.3 Motivation: Milk Separation Project

This research is part of an Australian Research Council (ARC) Linkage project with Geoffrey Gardiner Dairy Foundation, where the dairy industry is interested in milk separation using ultrasound. The current technology involves use of centrifuges whereas the use of ultrasound can perform the same job involving simpler devices that have no moving parts. The task is achieved through piezoelectric transducers.

This work involved a quantitative and qualitative measure and comparison of forces induced by steady streaming acting on fluid particles, to determine if these forces bring the particles to attract or repel each other. In particular, since the fluid under consideration is milk, the role of streaming forces acting on micron-sized fat particles, Milk Fat Globules (MFGs), in making them attract or repel each other, will be studied. The main focus will be on bringing MFGs to stick together.

Along with the theoretical and computational work, experiments were carried out as a part of this project. Macro- and micro- scale experiments were conducted by Dr. Thomas Leong and Dr. Linda Johansson, respectively (Leong *et al.*, 2016). Work was undertaken to design and employ micro-scale systems and microscopy to study specific aspects of the large scale operation, in addition to other methods of chemical analysis of extracted fat and particle size analysis (Johansson *et al.*, 2016). A cross validation was part of this process to ensure the micro-scale systems truly represent the engineering scale systems. Following are the values of parameters that were used in the experiments done by Leong *et al.* (2016), in order to separate

cream from milk by using ultrasound:

- Pressure amplitude of sound wave, $P = 100$ kPa
- Frequency, $\omega = 1 - 2$ MHz
- Radius, $R = D/2$, is measured between 2 – 5 micrometers

With the knowledge of pressure amplitude of the sound wave, frequency, and radius of the particles, the following entities can be derived (Skudrzyk, 1971):

- $\epsilon = 1/100 \approx \mathcal{O}(10^{-2})$
- Velocity scale, U , in steady streaming is $2\pi 10^{-8} \times 10^6 \approx \mathcal{O}(10^{-2}) - \mathcal{O}(10^{-1})$ m/s

It has been known since the 1920s that sound waves can separate particles from fluids (e.g. (King, 1934; Yosioka & Kawasima, 1955; Yasuda *et al.*, 1995)). This technology also has applications in food processing (Juliano *et al.*, 2013), petrochemical (Dionne *et al.*, 2013), pharmaceutical (Maitz *et al.*, 2000), and bio-medical industries (Petersson *et al.*, 2004).

The MFGs are less dense than rest of the composition of milk fluid and hence float at its surface when left for some time. If attraction of the MFGs under the influence of steady streaming causes them to touch, then they will rise out of milk faster, which is the desired outcome as mentioned before. One of the outcomes of the micro- scale experiments was that MFGs need to be in contact (but need not coalesce) in order to cream (Manasseh *et al.*, 2016). Also, it was found experimentally that particles of small size do not get removed from milk (Leong *et al.*, 2016). The experimental results implied that there was some size threshold below which particles would

never reach an antinode. In this work, an attempt will be made to give an explanation for why the smaller sized particles stay suspended in the milk.

1.4 Thesis Outline

Chapter 2 reviews literature for steady streaming flows around single and multiple spherical particles. In **chapter 3**, two computational methods, namely DNS (Direct Numerical Simulation) and WNF (Weakly Non-linear Formulation), are briefly introduced. They will be employed to investigate the role of steady streaming in bringing spherical particles to touch. The focus of this thesis is not the development of these computational methods, but to apply them to study the behaviour of particles under the effects of steady streaming. The flow considered is restricted to only two equal sized particles for simplification. The equations along with the non-dimensional parameters involved in the numerical model are also discussed. In **chapter 4**, steady streaming around a single sphere is modelled using DNS. The DNS is compared with literature and thoroughly verified for a single sphere first. Those DNS results are used in order to verify the other numerical method, WNF, in **chapter 5**. WNF is much faster than the DNS, especially for steady streaming flows around two spheres, and quite accurate as well. In **chapter 6**, the perturbation based method WNF is used to calculate steady streaming flows and forces exerted on two spheres, solving the weakly non-linear form of Navier Stokes equations. The problem for two-spheres is defined along with its parameters. Regimes where two equal sized spheres attract or repel each other in three different configurations for different frequencies are discussed.

The work in chapters 5 and 6 is based on the analysis of Fabre *et al.* (2017). The objective of work in **chapter 7** is to find initial conditions and the time involved for the spheres to touch. This chapter is entirely the work of the author. **Chapter 8** comprises conclusions and discussion leading to those conclusions.

In July 2015, David Fabre, Assistant Professor at Institute of Fluid Mechanics, Toulouse, visited Swinburne University of Technology. This visit led him to derive the equations mentioned in chapter 3. Chapter 6 is rewritten and is largely his work that is published in Fabre *et al.* (2017).

Chapter 2

Literature Review

2.1 Introduction

Consider the conservation of momentum expressed in terms of Euler's equation,

$$\frac{\partial}{\partial t}(\rho \mathbf{u}) + \mathbf{u} \cdot \nabla(\rho \mathbf{u}) = -\nabla p + \rho \mathbf{g}, \quad (2.1)$$

where \mathbf{u} , ρ and p denote the velocity, density, and pressure in the fluid, respectively, and \mathbf{g} is the acceleration due to gravity. Assuming density ρ constant and forces due to gravity are at balance, a simpler version of equation (2.1) is

$$\frac{\partial \mathbf{u}}{\partial t} + \mathbf{u} \cdot \nabla(\mathbf{u}) = -\frac{1}{\rho} \nabla p, \quad (2.2)$$

There is a quadratic non-linearity present on the left hand side in equation (2.2) as a product of velocity and velocity gradient $\mathbf{u} \cdot \nabla \mathbf{u}$. This non-linearity can be produced in two ways: either the velocity \mathbf{u} has to be large or the gradient of velocity $\nabla \mathbf{u}$ is large. The time-average of this product is non-

zero. It is this non-linear term that is responsible for steady streaming in the fluid. The focus of study in this chapter is the streaming flow generated when a solid boundary oscillates in an incompressible fluid, generating steady streaming. The particles are assumed to be very small in comparison to the wavelength of the stationary acoustic wave. This allows the assumption of fluid immediately around the particles as incompressible.

In the following sections, a review of literature is presented for single and multiple spherical particles, with an emphasis on behaviour of these particles due to steady streaming.

2.2 Steady Streaming around Single Oscillating Spheres

The steady streaming flow around a sphere in a sound field was analysed by Lane (1955) who followed the approach of Rayleigh (1883). Lane identified inner vortices in the oscillatory boundary layer (or Stokes layer) around a spherical particle in a sound field. These inner vortices would in turn drive outer vortices (see Figure 2.2). The speed of flow in the inner vortices would be expected to be much higher than in the outer vortices. It was observed that the thickness of the Stokes layer was much less than what was given theoretically. A comparison of streaming around a sphere with previously studied streaming around a cylinder was also given.

Longuet-Higgins (1998) also used perturbation methods for his analysis of streaming around a bubble. It was reported that the streaming flow

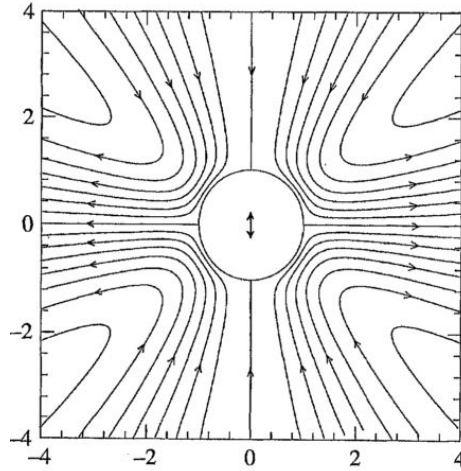


Figure 2.1: A quadrupole-like streaming around a linearly translating particle when the particle is moving vertically. The image is reproduced from Longuet-Higgins (1998), by permission of the Royal Society.

followed a quadrupole pattern when the bubble was translating (see Figure 2.1) and a dipole pattern when it was undergoing volumetric pulsations, which was also reported by Wu & Du (1997). It was determined that the streaming velocities were enhanced by at least an order in magnitude in the case where it is oscillating volumetrically. Although steady streaming was computed, the forces induced as a result were not taken into account. Furthermore, these results were only valid when the oscillations of the particle were small compared to its radius.

The case for single translating bubbles is relevant to non-pulsating or rigid spheres. In this context, a significant difference between the translating bubble and the rigid sphere, which will be considered later in this thesis, is the application of a no-slip boundary condition in the rigid sphere case. In this thesis, the sphere is a MFG, which is solid at the prevailing temperatures. Thus, a no-slip boundary condition can be used.

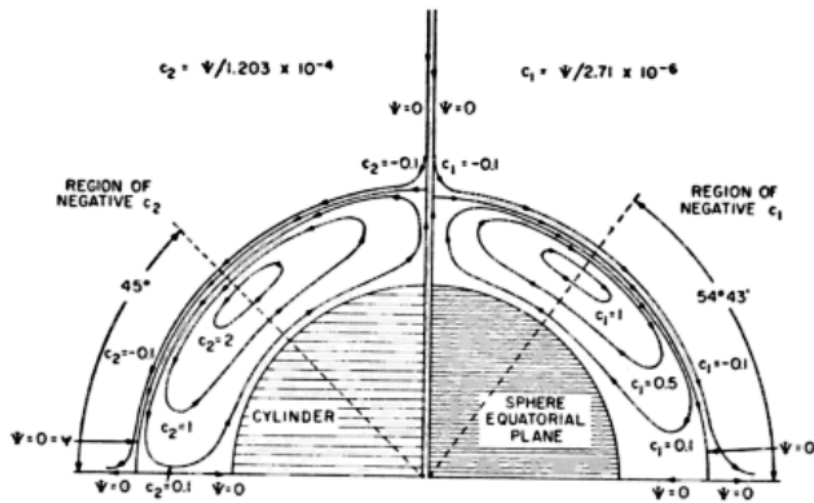


Figure 2.2: Sketch of the inner streaming vortices around a horizontally vibrating cylinder and a spherical particle. Reprinted with permission from Lane (1955). Copyright 1955, Acoustic Society of America.

Many authors, including Longuet-Higgins (1998) and Davidson & Riley (1971), assumed incompressibility of liquid around particles. For the existence and passage of sound, compressibility is required at leading order, when expanded in ϵ , but not at the next order. Since it is assumed that the fluid is incompressible at the order above the leading order, the passing acoustic wave can be modelled as an oscillatory boundary condition.

The vibration of an isolated single rigid sphere has been studied in two- and three- dimensional steady and oscillatory flows, analytically, numerically and experimentally. Some of the notable analytical and numerical works are based on perturbation theory (Lane, 1955; Riley, 1967; Tabakova & Zapryanov, 1982), spectral methods (Chang & Maxey, 1994), series truncation methods (Alassar & Badr, 1997) and spectral element methods (Blackburn, 2002).

Riley (1967) distributed and described flows induced by a solid body oscillating in a viscous fluid, with small amplitudes compared to its size, into the following four cases depending on the range of parameters Re and ϵ , defined as

$$\epsilon = \frac{U}{\omega D}, \text{ and } \text{Re} = \frac{UD}{\nu}, \quad (2.3)$$

where U is a velocity scale equal to the vibration velocity amplitude, ω is the frequency of oscillation, D is the sphere diameter, and ν is the kinematic viscosity. Thus, ϵ is the ratio of the vibration amplitude to the diameter of the sphere. In the literature, the ratio $1/\epsilon$ is also known as the Strouhal number, denoted by St . The parameter ϵ is the ratio of length scales, which gives a comparison of the displacement of the particle (or the motion of the far field relative to the sphere) to the diameter of the sphere. Re is proportional to the ratio of inertial forces to viscous forces, commonly known as Reynolds number. The ratio of Re and ϵ is commonly used in the literature as M^2 , whereas their product is defined as Re_s . To minimize the number of parameters, $M^2 = 4\Omega$ has been used in this thesis, as defined later in chapter 3, section 3.2.2):

Case I: $4\Omega = \frac{\text{Re}}{\epsilon} = O(1)$.

This case corresponds to $\epsilon \text{Re} \ll 1$, when the steady streaming persists outside the oscillatory boundary layer (a feature of the flow for large Ω), that has the same structure as Stokes boundary layer but spread over a much wider region as compared to the diameter, D , of the sphere.

Case II: $\text{Re} = \epsilon 4\Omega = O(1)$.

$$\Rightarrow \Omega = O(1/\epsilon), \text{ with amplitude of oscillation } \epsilon \ll 1 \Rightarrow \Omega \gg 1.$$

For $\Omega \gg 1$, the steady streaming that persists outside of the oscillatory boundary layer again assumes a Stokes-like character.

Case III: $\text{Re}_s = \epsilon^2 4\Omega = \epsilon \text{Re} = O(1)$.

$$\Rightarrow \text{Re} = O(1/\epsilon) \Rightarrow \epsilon \ll 1 \ll \text{Re}$$

$$\Rightarrow \Omega \gg 1 \Rightarrow \delta \ll D, \text{ as } 2\sqrt{\Omega} = \frac{D}{\delta}.$$

Thus, with $4\Omega \gg 1$ for a steady viscous flow, the Stokes layer is small compared to the size of the sphere. Also, $\text{Re}_s \ll 1$ is a necessary and sufficient condition for the outer steady flow to be Stokes-like, as in cases I and II. If $\text{Re}_s \gg 1$, the outer flow will assume a boundary-layer character, with the inner boundary layer being confined within this outer boundary layer.

Case IV: $M \ll 1$.

This case is basically equivalent to $\text{Re} \ll \epsilon \ll 1/4$. Also $2\sqrt{\Omega} = D/\delta \ll 1$ implies that $D \ll \delta$. Hence, the oscillatory boundary layer δ will extend over a much wider region compared to the size of the sphere, D .

Axisymmetric flows studied by Riley (1966) for two cases, $\text{Re} \ll 4\Omega \ll 1$ and $4\Omega \gg 1$, are illustrated in Figure 2.3. The boundary layer in Figure 2.3(b) is very thin as compared to Figure 2.3(a).

Chang & Maxey (1994) considered the same cases as Riley (1967) for $\epsilon \geq 0.05$ and $\text{Re} \leq 20$. It was found that $\text{Re}_s = 2\epsilon \text{Re} \gg 1$ is the necessary and sufficient condition for a low amplitude oscillatory flow to have a double-boundary layer structure, but this condition did not hold for high amplitudes and so it could not be generalized for flows of all amplitudes. A similar analysis for the case of bubbles was performed by Davidson & Riley (1971) in which they discovered differences in direction and velocity magnitudes for

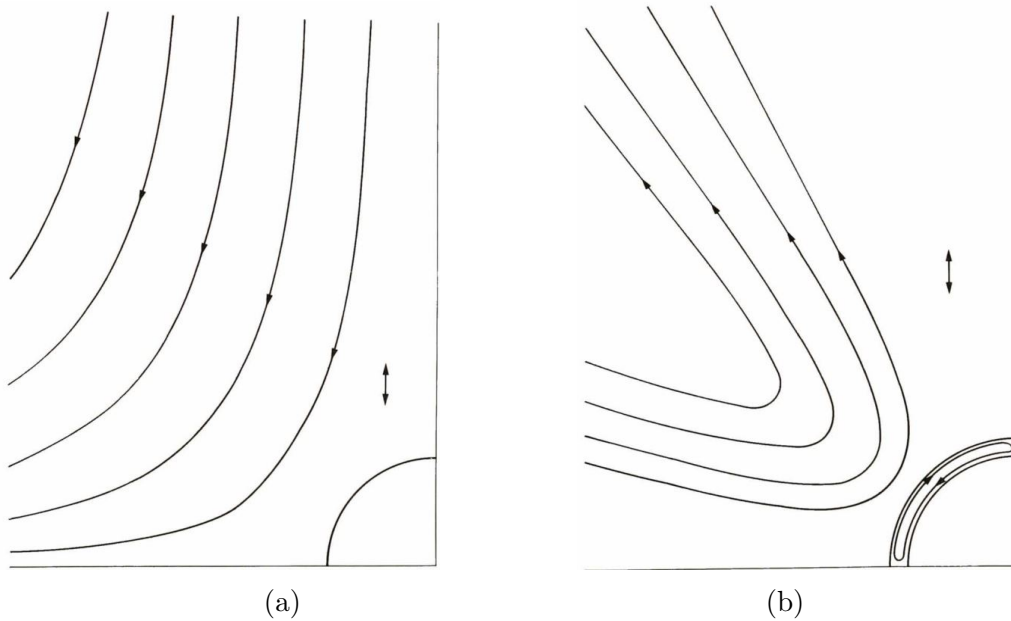


Figure 2.3: Streamlines of flow around a single sphere oscillating in a vertical direction for (a) $\text{Re} \ll 4\Omega \ll 1$, and (b) $4\Omega \gg 1$ and $\text{Re}_s \ll 1$. Reproduced from Riley (1966) by permission of Oxford University Press.

case $\Omega \gg 1$.

Blackburn (2002) presented a numerical study for scalar and momentum transport for steady and oscillatory incompressible flows. The Navier-Stokes and scalar transport equations were integrated with respect to time. A spectral element approach was applied to solve the problem, together with the Gauss-Lobatto-Legendre (GLL) quadrature for integration. The dimensionless parameters defined were similar to those defined in this thesis, i.e. Reynolds number, Re , and oscillation amplitudes, ϵ . The range of these parameters used was $1 \leq \text{Re} \leq 100$ and $0.05 \leq \epsilon \leq 5$. The mesh employed was designed in a way so that it could capture effects near the boundary of the sphere when the maximum extent of the domain was $50D$.

A comparison for peak coefficients of a drag force for a stationary

sphere in an oscillatory flow, as well as for an oscillating sphere in a quiescent fluid, was presented as a function of Re and ϵ . These results matched well with Basset's analytical solution (Basset, 1888) for amplitudes $\epsilon \leq 1$. Blackburn (2002) commented on the 'two-celled structure' of the oscillatory flow, namely inner and outer vortices. To explore the presence and structure of these vortices in the streaming flow, the size of the inner vortices was measured. It was observed that the inner recirculation region decreases as the Reynolds number, Re , increases. It was the largest for low Re , so much so that it reached the extent of the domain, and the results were deemed unreliable at those points. These results are used for verification of DNS in the present study, and are presented in chapter 5.

There have been recent experimental studies for three-dimensional flows around a single oscillating sphere at finite Reynolds numbers, Re , and oscillatory amplitudes, ϵ , producing visualizations (Kotas *et al.*, 2006; Otto *et al.*, 2008). In other recent experiments involving finite numbers of spheres, steady streaming is considered responsible for attraction between spheres in oscillating flows (Voth *et al.*, 2002).

Recently, there have been studies other than those involving acoustics, that resulted in similar patterns of steady streaming for vibrating circular cylinders Van Dyke (1982) and spheres Otto *et al.* (2008) at macro scales. Earlier, these works were preceded by studies of streaming in the vicinity of cylinders (Raney *et al.*, 1954).

The experiments of Kotas *et al.* (2006) involved extracting three-dimensional streaming flows around a vertically oscillating single sphere (and spheroid) for oscillation amplitudes, $0.04 \leq \epsilon \leq 1.2$, also measuring the size

of the inner vortices. It was concluded that the extent of the inner vortices is not dependent on the amplitude of oscillation, ϵ , but on the ratio ν/ω , which is the square of the thickness of oscillatory boundary layer (or Stokes layer), $\delta = \sqrt{\nu/\omega}$.

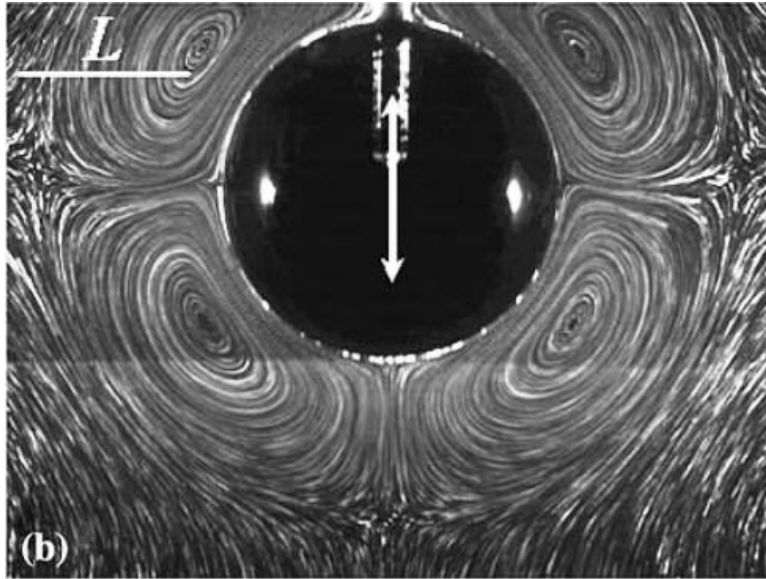


Figure 2.4: Steady streaming around a sphere oscillating vertically. $L = 1.4$ cm is the radius of the sphere. Reprinted with permission from Springer Nature, Kotas *et al.* (2006), Copyright 2006.

A useful private communication (with R. S. Alassar) was also mentioned by Kotas. This indicated that the extent of the inner region increases about 10% after 10 oscillations than when measured after 100 oscillations. In addition, it was suggested that ϵ , ratio of the oscillation amplitude to the body length scale, appeared to have little if any effect on the streaming velocity. This meant that results at relatively large ϵ could be extended to the very small ϵ values. These results, that the size of the inner region for steady streaming around cylinders was independent of ϵ for $\epsilon < 0.5$, were validated with the results of Raney *et al.* (1954), and the asymptotic analyses

of oscillating spheres for $\epsilon \ll 1$ were validated with Riley (1966).

In the experiments of Kotas *et al.* (2006), the sphere was attached to a metal rod oscillating vertically, hence obstructing measurement of distance to the stagnation point in the direction of oscillation (see Figure 2.4). The way that Kotas *et al.* (2006) measured the distance from the center of the sphere to the stagnation points was modified and improved by Alassar (2008) in a numerical study. A new definition for this distance was given to measure the length up to the stagnation points, which is equivalent to the size of the inner vortices in the direction of stagnation point under consideration. As a consequence, it was proved that the size of the inner vortices parallel and perpendicular to the direction of axis of oscillation was not the same. It was noted that the size of the inner vortices changed with varying θ , the angle between the stagnation points lying to the right and to the top of the sphere, when oscillating vertically. Thus the shape of the inner vortices was found to be non-symmetric along and perpendicular to direction of the axis of oscillation. It was also observed that as the Reynolds number, Re , gets higher, the inner vortices get thinner. Also, increasing the frequency oscillations weakened the outer vortices.

Otto *et al.* (2008) observed the flows around a sphere, far from boundaries but close to the bottom wall, oscillating vertically in a container filled with fluid. In estimating location of the stagnation point and measuring size of the inner vortices, it was pointed out that at large oscillation amplitudes, ϵ , the streaming flows can be very different than the widely studied small amplitudes of oscillation. This work was aimed at self-organization of spheres following Voth *et al.* (2002). For flows around a single sphere at low

Re, repulsive behaviour was predicted, contrary to the attraction observed by Voth *et al.* (2002). Another interesting observation was that the data for the distance to stagnation points provided by Kotas *et al.* (2006) collapsed on a single curve, suggesting that distances to stagnation points were independent of oscillatory amplitudes ϵ ; however this could only be verified for amplitudes, $\epsilon < 0.15$ in Otto's work. For larger amplitudes, the distances up to stagnation points were found to be dependent on ϵ . It was concluded that the interaction between multiple spheres in Voth *et al.* (2002) were due to non-linear interactions.

In 2009, Klotsa (2009) presented an experimental and numerical study of the interactions between rigid spheres vibrated horizontally in a small cell filled with liquid. More importantly, the interaction of two equal- and unequal-sized spheres was also studied. The range of parameters for two-sphere experiments was $3 \leq \text{Re} \leq 113$, and $0.08 \leq \epsilon \leq 3$, and for the simulations, $5 \leq \text{Re} \leq 120$. A numerical model was developed to simulate a finite box in which the spheres were sitting on the bottom, which was shaken horizontally, including effects of the boundary walls on the flow.

For a single oscillating particle of 1 mm diameter, qualitative agreement of the numerical simulation devised by Klotsa (2009) was found with the experiments of Kotas *et al.* (2006) and Otto *et al.* (2008) and the numerical studies of Chang & Maxey (1994) and Alassar & Badr (1997). A difference of 17% was found between the drag forces measured by the devised model and that of Alassar & Badr (1997). The emphasis of development of this model was on capturing physical mechanisms of the system rather than its numerical accuracy. It was able to capture the behaviour of the system and

allowed addition of a large number of rigid spheres that could interact with one another.

2.3 Steady Streaming Flow around Two Spheres

To study streaming flows around single and multiple bubbles, Tho (2005) performed experiments observing the quadrupole and dipole streaming structures described by Longuet-Higgins (1998) for single particles. Tabakova & Zapryanov (1982) analytically analysed interaction of two spheres oscillating translationally in a viscous fluid and concluded it to be attractive.

An experimental study was conducted by Voth *et al.* (2002) to determine behaviours of two and of more than two particles, or rather clusters, under the influence of horizontal vibrations of 20 and 50 Hz frequency. The particles were spheres made of stainless steel and were of radius = 0.397 mm. The particle Reynolds number, $Re = \frac{A\omega D}{\nu}$, ranged between 2 and 10. For two such spheres, it was proved that the attraction between particles is due to the streaming mechanism. An expression for the inflow velocity, and the decreasing distance between the two spheres, were also given. Systems of more than two particles were also discussed.

Otto *et al.* (2008) used three-dimensional particle tracking velocimetry to calculate steady streaming flows around two spheres oscillating in translation. This work was based on the experimental work of Voth *et al.* (2002) and provided improvements in previous calculations. Predictions were made about attraction and repulsion regimes for two spheres of rather large size of 1.91 cm in diameter. It was indicated that explanations given by Voth

et al. (2002) were over simplified in this case and needed further work for a better understanding of non-linear interaction of such flows.

For two identical spheres of 1 mm diameter, Klotsa *et al.* (2007) concluded that one will take a path that follows the outer streaming flow of the other until they align perpendicular to the direction of oscillation. It was shown experimentally that two rigid dense spheres subjected to oscillatory fluid flow will attract each other and line up perpendicular to the flow with a well-defined equilibrium gap between them. In particular, the interaction force between the two spheres was measured and a long-ranged attraction and a short-ranged repulsion was found between the spheres for different viscosities and vibratory conditions. Furthermore, once two spheres were ‘linked’ due to an equilibrium gap between the spheres, the pair behaved as a single unit and paired with another such unit to form a chain. Klotsa (2009) also studied the formation and interaction between such chains of spheres.

A useful technique was employed by Pacheco-Martinez *et al.* (2013) to study streaming flows through magnetically levitating particles in a fluid. The flow was not influenced by boundary effects this way. The conclusions of this study reinforced the foregoing findings that particle attraction was caused by streaming flows.

2.4 Transport and Organization of Multiple Particles

In the literature, extensive material is found for bubbles and forces acting on them, as compared to solid particles. However, more focus has been on radiation forces on bubbles rather than streaming forces in that work (Doinikov, 2003; Xi, 2012; Manasseh, 2015).

A vast amount of work on steady streaming flows around particles is reported in the field of microfluidics, particularly regarding particle trapping (Wang *et al.*, 2012), particle aggregation (Collins *et al.*, 2016), flow control (Townsend *et al.*, 2004), and droplet transport and coalescence (Pangu & Feke, 2007). A review on applications of acoustic streaming in microfluidic devices is given by Wiklund *et al.* (2012).

Townsend *et al.* (2004) modelled fluid flow in an ultrasonic standing wave in microfluidic devices that could also be extended to macro fluid flows. A particle model was developed using Computational Fluid Dynamics (CFD) software to determine the velocity profile of the particle mix passing through the acoustic device. This velocity profile was then integrated over time in order to determine particle paths, with which the particle concentration was measured. The model was applied to control particle concentration passing through a flow separator. The forces under consideration took into account the drag force and the acoustic radiation force, however, second order acoustic effects and other particle forces, such as van der Waals forces, interparticle forces, and lift, were not considered in the model.

A comprehensive review of work done in acoustofluidics is given

by Friend & Yeo (2011), covering generation of various types of acoustic waves, their propagation in different fluids, and manipulation of particles for applications for micro- and nano-fluids. In another review on separation of suspensions and emulsions using ultrasonic standing waves, Trujillo *et al.* (2014) predicted that if acoustic streaming is strong, it will disrupt any aggregated particles. The successful use of ultrasonic separation in the food processing industry was discussed, specifically the enhanced creaming of milk fat globules and oil recovery from palm oil. Further large-scale applications of ultrasonic separation, such as separation of microalgae for production of biodiesel (Bosma *et al.*, 2003), blood sample preparation (Pettersson *et al.*, 2004), and cell perfusion and harvesting (Pui *et al.*, 1995) were presented in a review by Leong *et al.* (2013). It was concluded in Leong *et al.* (2014) that higher energy density was key to increase the rate of separation of fat particles in milk.

In a recent numerical study, movement of micron-sized particles under the effect of radiation forces was investigated by Sepehrirahnama *et al.* (2015). The primary and secondary radiation forces (caused by scattering of the wave) were measured and compared for rigid spheres in a standing wave. Using the proposed numerical scheme based on multi-pole series expansion and the weighted residual method, the effects of position, incident angle and size of the rigid particles were studied.

In another related but separate numerical study, Sepehrirahnama *et al.* (2016) incorporated the effects of viscosity in the fluid, to calculate radiation forces and acoustic streaming effects for rigid spheres in a standing wave. The objective was to study the role of viscosity on the interaction

between rigid spheres in a sound field. However, streaming effects were neglected at first in the total force as they are negligible in a standing wave. Results were discussed only for equal sized spheres, but of three different radii. It was concluded that the viscosity and streaming had a larger effect on the smaller spheres, while the total radiation force became larger when the spheres were larger. Also, it was found that in the presence of viscosity, the acoustic streaming enhanced the interaction force by three orders of magnitude in comparison to the inviscid fluid. However, the analysis was not valid when the spheres were close to each other, although it was predicted that the acoustic streaming effects over power when distance between particles was small. This study was limited to only a single configuration when the spheres were sitting along the direction of the wave.

Experimental and numerical studies were conducted by Saadatmand & Kawaji (2010, 2013) to investigate the effects of fluid viscosity on motion of a solid particle under the influence of vibration in a cell filled with viscous fluid, with particular emphasis only on repulsive forces exerted on the particles by the nearest wall.

In another recent study, Lyubimov *et al.* (2013) discussed pattern formation of identical particles under the effects of high frequency vibration. Two identical rigid particles were subjected to a uniform pulsational flow, with a high frequency such that the thickness of Stokes layer around the particles was small in comparison to particle size and distance between particles. Thus, the fluid was assumed incompressible and the flow as inviscid except for flow near the particles. If the particles were aligned in such a way that there was a non-zero angle between the axis of vibrations and the line

connecting the particles, the particle pair turned. Chains of particles were formed perpendicular to the direction of such enforced vibration. The effects of boundaries and of gravity were ignored in this work.

In a comprehensive study for streaming around single and multiple spherical particles, Klotsa (2009) simulated flows in a cell used in experiments, compromising on the accuracy of the numerical model used in order to focus more on the physical phenomenon between the particles. For a single sphere, the flow included effects of walls and bottom boundaries. There was no mention of trajectories of individual particles and tracing their paths. The orientation of particles was analyzed when they were only short distances apart i.e. $\sqrt{2}R$.

2.5 Review Summary

Steady streaming flow around a single oscillating sphere can be visualized in Figure 2.4. The parameter space used in work reviewed in this chapter for steady streaming around a single sphere is summarized in Figure 2.5. Most of the theoretical work carried out for steady streaming around single spheres has been focused on small oscillatory amplitudes, $\epsilon \ll 1$, and $M^2 \ll 1$.

Out of these studies for a single oscillating sphere, important conclusions relevant for the current study are the following:

- The length of the inner vortices is independent of ϵ and dependent on Stokes length δ , for small oscillatory amplitudes $\epsilon \ll 1$ (Riley, 1967; Chang & Maxey, 1994).

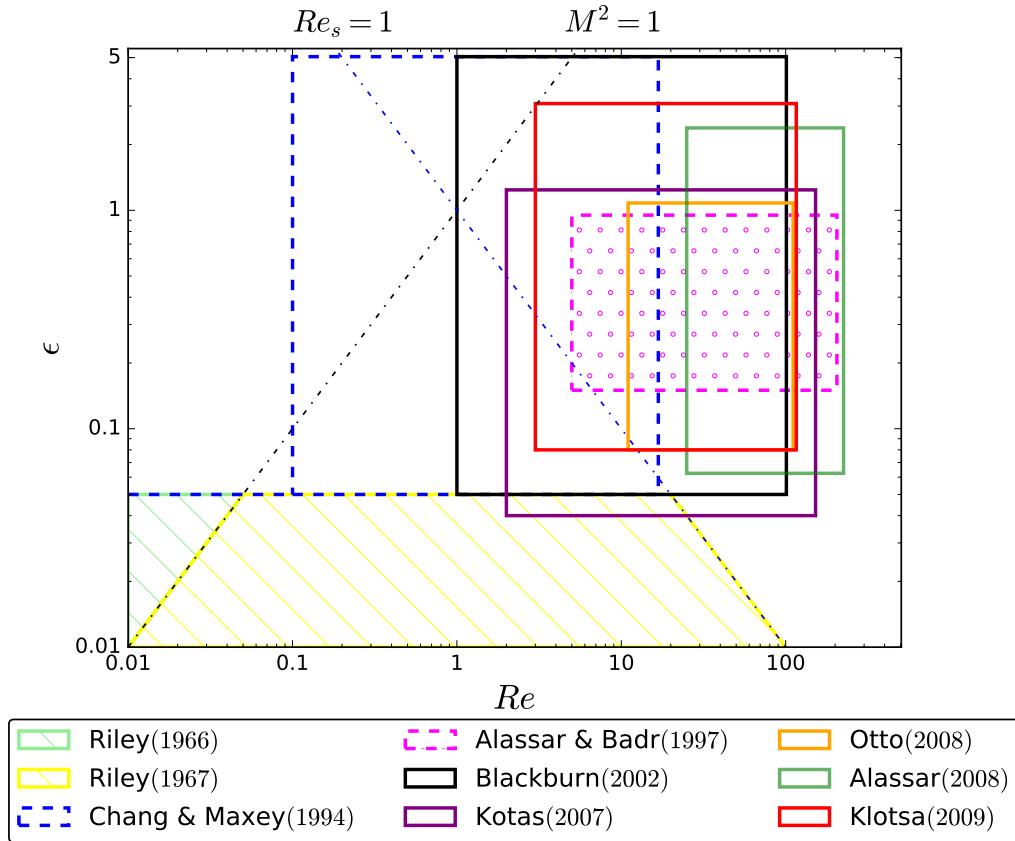


Figure 2.5: Parameter spaces for various studies conducted for steady streaming flows around a single sphere, where the entire domain shown is the parameter space used in this study. Re_s is the product, and M^2 is the ratio of dimensionless parameters Re and ϵ , respectively. The shaded regions for Riley (1966, 1967) is depicting region where $\epsilon \ll 1$.

- The shape of the inner vortices is non-symmetric over and perpendicular to the axis of oscillation (Alassar, 2008).
- Whether there is a ‘two-celled’ structure present in the flow, comprising of the inner and outer streaming, can be assessed by the size of the inner vortices (Blackburn, 2002).

For studying steady streaming around two spheres, mostly experimental and numerical approaches were used. The use of these approaches

also gave an advantage of incorporating flows at higher oscillatory amplitudes, ϵ . However, most of these studies were limited in either the parameter space, the configuration of particles under consideration, or the accuracy of the numerical model used (Otto *et al.*, 2008; Sepehrirahnama *et al.*, 2016; Klotsa, 2009).

Various studies have been carried out for particle transport in different fields of life such as biotechnology (microfluidics), chemical engineering (food processing and petrochemical industry etc), and mining (for processes such as sedimentation) to name a few. None of the studies reported was targeted particularly to investigate the role of steady streaming for transport and accumulation of solid spherical particles to bring them close to each other.

In the work carried out in this thesis, particular attention will be paid to try to fill the gaps, and questions thus posed, in the literature. In the next chapter, two numerical methods are introduced that will be used in subsequent chapters of this thesis to investigate the role of steady streaming in bringing spherical particles close to each other. For simplicity, this multiple particle system is limited to a study of only two particles at first.

Chapter 3

Methodology

3.1 Introduction

In this chapter, the computational methods used for simulation of steady streaming flows will be briefly introduced. The focus of this thesis is not the development of these computational methods, but to apply them to study the behaviour of particles under the effects of steady streaming. The equations that are involved in the numerical model are also discussed along with the non-dimensional parameters.

As noted in chapter 1, the main objective of this study is to find out the role of steady streaming once two spheres come close to each other, in making them attract or repel. In the next section, a formulation is developed for this problem, involving Partial Differential Equations (PDEs), that will later be solved using numerical methods.

In this chapter, a mathematical model is presented that is relevant to some aspects of steady streaming around Milk Fat Globules (MFGs) that

were mentioned in chapter 1. These particles, that are spherical in shape, are rigid enough to be assumed incompressible. Actual values of the parameters used for experiments are given in section 1.3. Since the size of these particles is very small in comparison to the wavelength of the imposed stationary acoustic wave (Keenan & Mather, 2006), and that they are immersed in a fluid that has similar properties to that of water, the fluid is assumed incompressible, following discussion in section 2.1. For a simpler flow, this multiple particle system is kept to a study of only two particles.

3.2 The Governing Equations

Assume a Newtonian fluid that behaves as a continuum. As noted in section 1.2.2, if the size of the sphere immersed in this fluid is very small in comparison to the wavelength of the stationary acoustic wave, then the fluid around the sphere can be assumed incompressible. An incompressible sphere is assumed to be immersed in an incompressible fluid, either liquid or gas, that is subject to a stationary acoustic wave. Since the wavelength of the applied acoustic wave is large compared to the particle size, as just noted, this can also be seen as an oscillation being applied in the far field of the fluid. On the surface of particles, a no-slip boundary condition was applied. Such a flow can be modelled mathematically by the equation of continuity and the Navier-Stokes equation for conservation of mass and momentum,

respectively, in Cartesian coordinates given as:

$$\begin{aligned} \nabla \cdot \mathbf{u} &= 0, \\ \rho \left\{ \frac{\partial \mathbf{u}}{\partial t} + (\mathbf{u} \cdot \nabla) \mathbf{u} \right\} &= -\nabla p + \mu \Delta \mathbf{u}. \end{aligned} \tag{3.1}$$

The variables used are explained in Table 3.1.

The notation for the equation for conservation of momentum varies among authors. Some authors, like Davidson & Riley (1971) and Longuet-Higgins (1998), who discuss acoustic streaming prefer to use the stream function formulation of the Navier-Stokes equations in spherical polar coordinates.

Other authors, like Eckart (1948) and Riley (2001), used the primitive variable formulation, which retains the velocity and pressure in vector notation in the Navier-Stokes equations. The advantage of having the vector notation of these equations is that it allows the assumption of fluid incompressibility at second order to be easily incorporated, as the velocity (which will be the small parameter) appears explicitly.

3.2.1 Non-dimensionalization of the Navier-Stokes equations

The component-wise form of equation of motion for an incompressible fluid, with no body force is the form of the Navier-Stokes equations given below in cylindrical polar co-ordinates. The description of variables used in these equations is given in Table 3.1, where ‘*’ denotes dimensional variables.

Table 3.1: List of variables used in section 3.2.1

Variable	Meaning
\mathbf{u}	velocity vector
u	axial component of velocity
v	radial component of velocity
w	angular component of velocity
p	pressure
ρ	density
μ	dynamic viscosity
ν	kinematic viscosity
r	radial distance
ϑ	azimuthal angle
x	axial distance
t	time

Equation for Conservation of Mass (The Continuity Equation)

$$\frac{1}{r^*} \frac{\partial (r^* u^*)}{\partial r^*} + \frac{1}{r^*} \frac{\partial (v^*)}{\partial \vartheta} + \frac{\partial w^*}{\partial x^*} = 0 \quad (3.2)$$

Equation for Conservation of Radial Momentum

$$\begin{aligned} \frac{\partial u^*}{\partial t^*} + u^* \frac{\partial u^*}{\partial r^*} + \frac{v^*}{r^*} \frac{\partial u^*}{\partial \vartheta} - \frac{v^{*2}}{r^*} + w^* \frac{\partial u^*}{\partial x^*} = -\frac{1}{\rho} \frac{\partial p^*}{\partial r^*} + \nu \left\{ \frac{1}{r^*} \frac{\partial}{\partial r^*} \left(r^* \frac{\partial u^*}{\partial r^*} \right) + \right. \\ \left. \frac{1}{r^{*2}} \frac{\partial^2 u^*}{\partial \vartheta^2} - \frac{u^*}{r^{*2}} - \frac{2}{r^{*2}} \frac{\partial v^*}{\partial \vartheta} + \frac{\partial^2 u^*}{\partial x^{*2}} \right\}, \end{aligned} \quad (3.3)$$

where $\nu = \frac{\mu}{\rho}$ is the kinematic viscosity.

Equation for Conservation of Azimuthal Momentum

$$\begin{aligned} \frac{\partial v^*}{\partial t^*} + u^* \frac{\partial v^*}{\partial r^*} + \frac{v^*}{r^*} \frac{\partial v^*}{\partial \vartheta} + \frac{u^* v^*}{r^*} + w^* \frac{\partial v^*}{\partial x^*} = -\frac{1}{\rho r^*} \frac{\partial p^*}{\partial \vartheta} + \nu \left\{ \frac{1}{r^*} \frac{\partial}{\partial r^*} (r^* \frac{\partial v^*}{\partial r^*}) + \right. \\ \left. \frac{1}{r^{*2}} \frac{\partial^2 v^*}{\partial \vartheta^2} + \frac{2}{r^{*2}} \frac{\partial u^*}{\partial \vartheta} - \frac{v^*}{r^{*2}} + \frac{\partial^2 v^*}{\partial x^{*2}} \right\} \end{aligned} \quad (3.4)$$

Equation for Conservation of Axial Momentum

$$\begin{aligned} \frac{\partial w^*}{\partial t^*} + u^* \frac{\partial w^*}{\partial r^*} + \frac{v^*}{r^*} \frac{\partial w^*}{\partial \vartheta} + w^* \frac{\partial w^*}{\partial x^*} = -\frac{1}{\rho} \frac{\partial p^*}{\partial x^*} + \nu \left\{ \frac{1}{r^*} \frac{\partial}{\partial r^*} (r^* \frac{\partial w^*}{\partial r^*}) + \right. \\ \left. \frac{1}{r^{*2}} \frac{\partial^2 w^*}{\partial \vartheta^2} + \frac{\partial^2 w^*}{\partial x^{*2}} \right\}. \end{aligned} \quad (3.5)$$

3.2.2 Dimensionless parameters

Let

$$t^* = \frac{t}{\omega}, r^* = Dr, u^* = Uu, v^* = Uv, w^* = Uw, x^* = Dx, \text{ and } p^* = Pp, \quad (3.6)$$

where ω is the frequency, U is the velocity amplitude, P is the pressure amplitude of the applied oscillation, and D is the diameter of the sphere.

Also, let

$$\epsilon = \frac{U}{\omega D}, \text{ and } \text{Re} = \frac{UD}{\nu} \quad (3.7)$$

as defined in section 2.2. In this study, $\text{Re} \approx \mathcal{O}(10 - 10^2)$.

The ratio of Re and ϵ is commonly used in the literature as $M^2 = \text{Re}/\epsilon$, as used in section 2.2. Using the definitions of Re and ϵ in equation (3.7), M can also be expressed in terms of thickness of the oscillatory boundary layer near the surface of the sphere or ‘Stokes layer’, $\delta = \sqrt{\nu/\omega}$, such

that $M = D/\delta$. Thus, M is a ratio of diameter of the sphere to the viscous length. In this thesis, M^2 is referred to as Ω , also known as ‘Stokes number’ (where $M^2 = 4\Omega$).

After non-dimensionalizing equations (3.2), (3.3), and (3.4) with the dimensional variables defined in equation (3.7), the following set of equations are obtained.

Equation for Conservation of Mass

From equation (3.2),

$$\Rightarrow \frac{1}{r} \frac{\partial(r^2 \rho u)}{\partial r} + \frac{1}{r} \frac{\partial(\rho v)}{\partial \vartheta} + \frac{\partial w}{\partial x} = 0 \quad (3.8)$$

Equation for Conservation of Radial Momentum

Equation (3.3) yields,

$$\begin{aligned} \Rightarrow \frac{\partial u}{\partial t} + \epsilon u \frac{\partial u}{\partial r} + \epsilon \frac{v}{r} \frac{\partial u}{\partial \vartheta} - \epsilon \frac{v^2}{r} + \epsilon w \frac{\partial u}{\partial x} = & -\frac{P}{U^2} \frac{\epsilon}{\rho} \frac{\partial p}{\partial r} + \frac{\epsilon}{\text{Re}} \left\{ \frac{1}{r} \frac{\partial}{\partial r} \left(r \frac{\partial u}{\partial r} \right) + \right. \\ & \left. \frac{1}{r} \frac{\partial^2 u}{\partial \vartheta^2} - \frac{u}{r^2} - \frac{2}{r^2} \frac{\partial v}{\partial \vartheta} + \frac{\partial^2 u}{\partial x^2} \right\} \end{aligned} \quad (3.9)$$

Equation for Conservation of Azimuthal Momentum

Also, from (3.4),

$$\begin{aligned} \Rightarrow \frac{\partial v}{\partial t} + \epsilon u \frac{\partial v}{\partial r} + \epsilon \frac{v}{r} \frac{\partial v}{\partial \vartheta} + \epsilon \frac{uv}{r} + \epsilon w \frac{\partial v}{\partial x} = & -\frac{P}{U^2} \frac{\epsilon}{\rho r} \frac{\partial p}{\partial \vartheta} + \frac{\epsilon}{\text{Re}} \left\{ \frac{1}{r} \frac{\partial}{\partial r} \left(r \frac{\partial v}{\partial r} \right) + \right. \\ & \left. \frac{1}{r^2} \frac{\partial^2 v}{\partial \vartheta^2} + \frac{2}{r^2} \frac{\partial u}{\partial \vartheta} - \frac{v}{r^2} + \frac{\partial^2 v}{\partial x^2} \right\} \end{aligned} \quad (3.10)$$

Equation for Conservation of Axial Momentum

Following from equation (3.5)

$$\Rightarrow \frac{\partial w}{\partial t} + u \frac{\partial w}{\partial r} + \frac{v}{r} \frac{\partial w}{\partial \vartheta} + w \frac{\partial w}{\partial x} = -\frac{P}{U} \frac{\epsilon}{\rho} \frac{\partial p}{\partial x} + \nu \left\{ \frac{1}{r} \frac{\partial}{\partial r} \left(r \frac{\partial v}{\partial r} \right) + \frac{1}{r^2} \frac{\partial^2 v}{\partial \vartheta^2} + \frac{2}{r^2} \frac{\partial u}{\partial \vartheta} - \frac{v}{r^2} + \frac{\partial^2 w}{\partial x^2} \right\} \quad (3.11)$$

Note that the numerical methods used, explained in the following section 3.3, are based on the assumption of axi-symmetry about the x -axis.

3.3 Numerical Methods Employed

This section contains a brief introduction to two numerical methods employed in this thesis, to simulate steady streaming around spheres: a Direct Numerical Simulation (DNS), based on a spectral element method, and a Weakly Non-linear Formulation (WNF), based on a finite element method.

As noted in chapter 1, the aim of this study is to find the role of steady streaming once two particles are close to each other, in making them attract or repel. The DNS is limited to axisymmetric flows around a single sphere unless it is upgraded to three-dimensions. This upgrading is likely to be very time consuming. In comparison, the task of computing steady streaming flows around single and two spheres can be achieved economically using WNF. It has the added flexibility of imposing oscillations at any given angle to the axis on which the spheres are placed. Both DNS and WNF offer advantages over the other depending on the situation being simulated, that will be discussed in the chapters following.

First, a single sphere problem is modelled and verified qualitatively and quantitatively against the literature using DNS. Then, the results using WNF and DNS are compared, qualitatively and quantitatively. For steady streaming around two spheres, a new problem is defined along with its set of parameters. WNF is used to obtain the results in three different configurations, depending on the alignment of the spheres with respect to the axis of oscillation. Flow visualizations as well as the forces exerted on the spheres by steady streaming measured using the DNS and WNF are presented in chapters 5 and 6. Based on the forces thus calculated using WNF of the two sphere problem, trajectories followed by the spheres are computed, mainly to find out initial conditions that would lead the spheres to touch, and the time it takes.

For both the DNS and WNF, the flow can be expressed by the incompressible Navier-Stokes equations. A single sphere of unit diameter, D , is modelled at the center of an unbounded, incompressible fluid. The fluid is oscillating with an amplitude A , and frequency ω . For two identical spheres set apart at a distance L between their centers and positioned at an angle θ , between the axis joining their centers and the axis of oscillation, a new setup is defined using WNF.

As noted in section 3.2.2, the dimensionless parameters defined are the inverse Strouhal number $\epsilon = A/D$ and Reynolds number $\text{Re} = UD/\nu$, where $U = A\omega$, and A is the amplitude and ω is the frequency of the oscillating flow, respectively, D is the diameter of the sphere, and ν is the kinematic viscosity. A ratio of Re and ϵ is introduced as $\Omega = \omega D^2/4\nu$, when using WNF, which as noted earlier, is often used as M^2 in the literature.

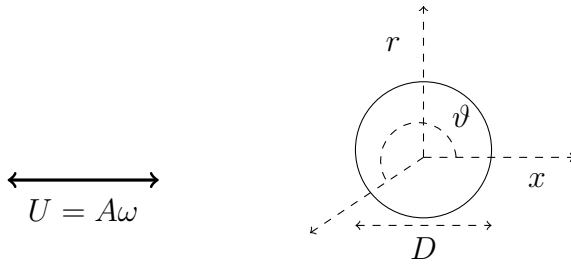


Figure 3.1: Schematic of the one sphere problem for the DNS.

3.3.1 DNS: Direct Numerical Simulation

The DNS is a specialized code developed at Monash University (Thompson *et al.*, 1996). The code is well established, and has previously been employed in axisymmetric, pulsatile flows with time-dependent boundary conditions (Griffith *et al.*, 2009) and for complex axisymmetric flows around spheres (Griffith *et al.*, 2011). It was adjusted to work for parameters that are valid for separation of milk cream using ultrasound. For the axisymmetric flow, a polar cylindrical co-ordinate system (r, ϑ, x) is used in which the velocity components are $\mathbf{u} = (u, v, w)$.

Integration of the governing equations

Axisymmetric simulations were performed using a spectral-element method, solving, as noted, the incompressible Navier-Stokes equations defined in equations (3.8) - (3.10). The domain was discretized into quadrilateral elements (with curved sides on the body boundary), and seventh-order Lagrange polynomials, associated with the Gauss-Lobatto-Legendre quadrature points were used as shape functions within these elements. These elements can be refined in the desired areas of the domain, known as h -refinement. Together with

Lagrange polynomials of order, p , it becomes an h - p method (Karniadakis & Sherwin, 2005).

The said governing equations were moved to the left hand side leaving them in the form $\mathbf{G}(r, \vartheta, x) = 0$. A test solution was substituted in this form of the equations resulting in a residual \mathbf{R} . The method of weighted residuals (MWR) was applied to weight the residual by taking integrals of the product of weighting functions and the residual \mathbf{R} and setting it equal to zero. This integral is easier to satisfy than the original equation, which is why it is called the “weak form”. Since both the test solution and the weighting functions used were tensor-product Lagrange polynomials, the method can be termed a Galerkin method. More detail on MWRs and Galerkin methods can be found in Fletcher (1984). These integrals were evaluated over every single element and then added together.

Time-stepping was performed using a three-way time-splitting scheme; a third-order Adams-Bashforth method was used to integrate the advection term, a Poisson equation for the pressure was formed by enforcing continuity at the end of this pressure sub-step, and a Crank-Nicolson scheme was used to integrate the diffusion term.

Boundary conditions

An example of the mesh employed is shown in Figure 3.2 where different boundaries are shown color-coded to distinguish between the various boundary conditions. Each color describes a unique boundary condition. The flow was assumed to be axi-symmetric about the direction of the oscillating flow $r = 0$ (colored yellow) where $\partial\mathbf{u}/\partial r = 0$. An oscillatory velocity was imposed

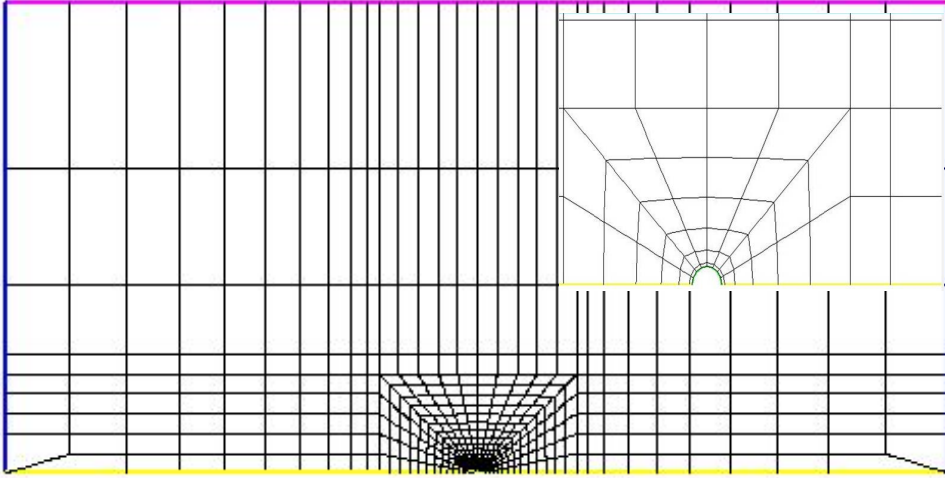


Figure 3.2: Spectral element mesh developed similar to that used by Blackburn (2002). Size of the elements is measured in terms of diameter of the sphere D . The colored edges of the mesh depict the boundary conditions explained in section 3.3.1. The sphere is positioned at the center of the bottom boundary, but is difficult to see due to the large size of the domain. (Inset) Detail of mesh around the sphere with fewer elements than that were actually used in the mesh, to depict the structure of the cells adjacent to the sphere.

at the domain boundaries on left and right sides for incoming and outgoing flow (colored blue). At the transverse boundary, the flow was parallel ($v = 0$), with zero-stress ($\partial u / \partial r = \partial w / \partial r = 0$) and the pressure gradient $\partial p / \partial r = 0$ (colored magenta). In addition to a no-slip condition for the velocity, the normal gradient of the pressure $\partial p / \partial n = 0$ was enforced at the surface of the sphere and all boundaries and is not over-constraining.

Mesh, domain size and resolution

The rectangular mesh comprised of a semi-circle embedded at the center of a rectangle, where the mesh is refined as shown in Figure 3.2. The mesh in Figure 3.2 is only a representative of its design in order to represent the different regions and cells clearly. The actual mesh used (M4 in Table 3.2)

Table 3.2: Meshes used for mesh analysis, M1 – M5, along with the total number of elements comprising them. The parameters varying in these meshes are length of the square, number of layers of elements from circle to the square, length of the domain upstream and downstream of square rear edge, number of elements from square front/rear edge to inlet/outlet, and number of total elements in the mesh, respectively.

Mesh	Total number of elements
M1	618
M2	2038
M3	3038
M4	3038
M5	3508

was much denser.

With the assumption of axi-symmetry about the direction of the axis of oscillation, this inner refined region becomes a complete square. The length of that inner square was 50 and number of elements on the surface of the sphere, azimuthally, was 20 in 100 layers, for the square around the sphere. The thickness of the first boundary layer of elements is $0.02D$. The length of the entire domain is $100D$ parallel to the axis of oscillation. The mesh was refined and large enough in the inner square to capture the micro-

Table 3.3: The distance from the surface of the sphere to the stagnation points, r_{cross} , measured using DNS with different meshes for a single sphere, M1 – M5 given in Table 3.2, for $Re = 1$, $Re = 40$, and $Re = 100$ when $\epsilon = 0.05$ and $\epsilon = 5.0$. Some meshes were under resolved and thus could not come up with a value of r_{cross} .

Mesh	$\epsilon = 0.05$			$\epsilon = 5.0$		
	Re = 1	Re = 40	Re = 100	Re = 1	Re = 40	Re = 100
M1	0.542258	0.701405	0.602502	-	4.314638	5.124527
M2	16.236372	0.704850	0.604381	-	7.553476	6.156302
M3	39.663735	0.709916	0.500001	-	7.798016	6.161393
M4	40.283592	0.709925	0.500001	4.275103	7.447914	6.159781
M5	47.736170	0.709921	0.5	5.701502	7.686545	6.160824

Table 3.4: Maximum drag force, F_d , measured using DNS with different meshes for a single sphere, M1 – M5 given in Table 3.2, for $Re = 1$, $Re = 40$, and $Re = 100$ when $\epsilon = 0.05$ and $\epsilon = 5.0$.

Mesh	$\epsilon = 0.05$			$\epsilon = 5.0$		
	Re = 1	Re = 40	Re = 100	Re = 1	Re = 40	Re = 100
M1	0.001598	0.302360	1.216117	0.001498	0.082962	0.269254
M2	0.001602	0.302210	1.215799	0.000868	0.075919	0.260984
M3	0.001602	0.302272	1.216166	0.000875	0.075585	0.260963
M4	0.001602	0.302212	1.215809	0.000901	0.075887	0.260974
M5	0.001602	0.302212	1.215811	0.000892	0.075646	0.260967

streaming effects near the boundary of the sphere, containing a total of 3038 elements. The effects were quantified in Tables 3.3 and 3.4 using meshes with different lengths of the domain and the inner square, of respective mesh densities with total number of elements given in Table 3.2.

Time step was fixed and determined by using the value of ϵ at the

Table 3.5: r_{cross} measured using DNS with mesh M4 given in Table 3.2, for $\epsilon = 0.05$ and $\epsilon = 1.00$, when n_T and n_{Av} are varied. Here, n_T is the number of periods before averaging, and n_{Av} is the number of periods over which the averaging is done.

a) $\epsilon = 0.05$

		Re = 1		Re = 40		Re = 100	
		10	20	10	20	10	20
n_T	n_{Av}						
	100	40.283592	40.305172	0.709925	0.5	0.5	0.5
	200	40.631368	40.643695	0.707909	0.707864	0.5	0.5

b) $\epsilon = 1.00$

		Re = 1		Re = 40		Re = 100	
		10	20	10	20	10	20
n_T	n_{Av}						
	100	9.805729	-	2.393395	2.404935	1.691852	1.691863
	200	8.27344	-	2.390973	2.390923	1.692016	1.692020

start of the calculation. It varied between $\mathcal{O}(10^{-6})$ and $\mathcal{O}(10^{-2})$ as ϵ increased. For mean flows in an oscillatory flow, the flow oscillated for 100 periods before an average was taken over a further 10 periods taking up to 65 hours. When the length of the mesh M4 was increased and refined in all the aspects by 10 units only (which is then named M5), it took up to 8 more hours for each simulation to converge. However, when the number of periods involved were doubled in the actual mesh used (i.e. the flow oscillated for 200 periods before an average was taken over a further 20 periods), each simulation took 165 hours. Therefore, M4 is the best compromise between mesh length, its refinement, and the time taken for the simulation to converge. The effects of varying the number of periods of oscillation involved are noted in Tables 3.5, and 3.6.

Table 3.6: F_d measured using DNS with mesh M4 given in Table 3.2, for $\epsilon = 0.05$ and $\epsilon = 1.00$, when n_T and n_{Av} are varied. Here, n_T is the number of periods before averaging, and n_{Av} is the number of periods over which the averaging is done.

a) $\epsilon = 0.05$

		Re = 1		Re = 40		Re = 100	
		n_{Av} \diagdown	10	20	10	20	10
n_T \diagdown	100	0.001602	0.001602	0.302212	0.304286	1.215809	1.228218
	200	0.001604	0.001604	0.321720	0.323516	1.325744	1.334958

b) $\epsilon = 1.00$

		Re = 1		Re = 40		Re = 100	
		n_{Av} \diagdown	10	20	10	20	10
n_T \diagdown	100	0.000922	0.000923	0.095229	0.095255	0.340142	0.340473
	200	0.000923	0.000923	0.095481	0.095506	0.343418	0.343742

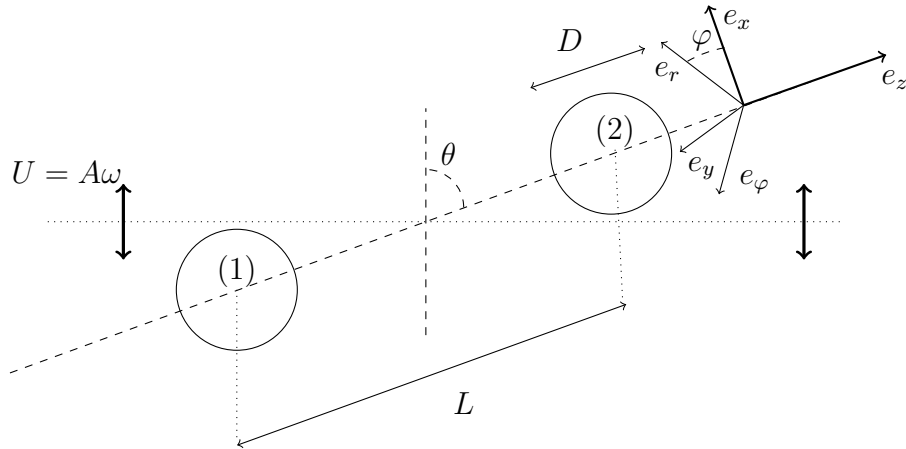


Figure 3.3: Schematic of the two sphere problem adapted from Fabre *et al.* (2017).

3.3.2 WNF: Weakly Non-linear Formulation

Two spheres of equal diameter, D , set apart at a distance L between their centers and positioned at an angle θ , are shown in Figure 3.3. The spheres are assumed to be non-rotating. θ is the angle between the direction of oscillation and the axis joining the two spheres. A no-slip boundary condition is assumed at the surface of spheres. When $\theta = 0^\circ$, the spheres are placed parallel to the axis of imposed oscillation, in an axial configuration. Similarly at $\theta = 90^\circ$, the spheres are positioned perpendicular to the axis of imposed oscillation, in a lateral configuration. The dimensionless parameters of the problem are: $\Omega = \omega D^2/4\nu$, $\text{Re} = A\omega D/\nu$, L/D , and θ .

Governing equations

As mentioned in section 1.4, the work presented in this subsection is already published. The weakly nonlinear formulation was derived and presented in Fabre *et al.* (2017). Only a brief overview of the weakly non-linear development is given here to help the reader with a better understanding of the

method and technique involved.

The incompressible Navier-Stokes equations defined in equation (3.1) are used. A schematic of the problem for two spheres of diameter, D , is given in Figure 3.3. As noted earlier in section 3.3, U is the oscillating velocity field imposed at the outer boundaries of the domain with amplitude A and frequency ω . A Cartesian frame ($\mathbf{e}_x, \mathbf{e}_y, \mathbf{e}_z$) relative to the axis joining the sphere centers together with a cylindrical frame ($\mathbf{e}_r, \mathbf{e}_\varphi, \mathbf{e}_z$) were used.

Far from the spheres, the velocity field must match the applied uniform oscillating flow defined as

$$\mathbf{u} \approx U [\cos \theta \mathbf{e}_z - \sin \theta \mathbf{e}_x] \cos \omega t \quad (3.12)$$

$$p \approx \rho U \omega [z \cos \theta - x \sin \theta] \sin \omega t. \quad (3.13)$$

In addition to the assumption that the centers of the spheres are fixed, a no-slip condition $\mathbf{u} = \mathbf{0}$ is also imposed on their surface, consistently with the no-slip condition used in the DNS.

The forces exerted on each of the spheres (1) and (2) in Figure 3.3, are given by

$$\mathbf{F}^{(1,2)} = \int_{\mathcal{S}_{1,2}} [-p\mathbf{n} + \nu(\nabla\mathbf{u} + \nabla\mathbf{u}^T) \cdot \mathbf{n}] dS \quad (3.14)$$

where $\mathcal{S}_{1,2}$ is the surface of the corresponding sphere, and \mathbf{n} is the vector normal to it pointing outwards.

In the following, the problem is solved in non-dimensional form by setting $D = 1$, $\rho = 1$, and $\nu = 1$. This assumption is required because of a

notational inconsistency between Fabre *et al.* (2017) and the present thesis. The flow can be represented by a state vector $\mathbf{q} = [\mathbf{u}; p]$. The assumption that the amplitude of the oscillating field, U , is small then implies $\text{Re} \ll 1$, so it is convenient to conduct an asymptotic analysis in terms of this parameter. Thus, \mathbf{q} can be expanded in series of Re as a combination of the first- and second-order solution as follows:

$$\mathbf{q} = \text{Re} \mathbf{q}_1 + \text{Re}^2 \mathbf{q}_2 + \mathcal{O}(\text{Re}^3) \quad (3.15)$$

The force exerted on each sphere can be similarly expanded, such that

$$\mathbf{F}^{(1,2)} = \text{Re} \mathbf{F}_1^{(1,2)} + \text{Re}^2 \mathbf{F}_2^{(1,2)}, \quad (3.16)$$

which means, in dimensional terms,

$$\mathbf{F}^{(1,2)} \equiv \rho \nu D U \mathbf{F}_1^{(1,2)} + \rho D^2 U^2 \mathbf{F}_2^{(1,2)}. \quad (3.17)$$

The second-order contribution to the force $\mathbf{F}^{(1,2)}$ in equation 3.17 consists of two terms: the first one is the steady part, and the second one, the unsteady part. The second unsteady part will not be considered here as only the time average of the force is of interest.

In equation (3.15), the solution to the equation at second-order is driven by the nonlinear term composed of the first-order terms. Further details on the weakly non-linear development itself, can be found in Fabre *et al.* (2017) and Sipp & Lebedev (2007). Gathering all the first- and second-order solutions led to the steady part of time-averaged force felt by the spheres,

$\overline{\mathbf{F}^{(1,2)}}$, as given in equation (3.17). Here, $\bar{\cdot} = 1/T \int_0^T \cdot dt$ refers to time average. The following expression is obtained from equation (3.17), taking into account the symmetry considerations, and reverting to a dimensional form:

$$\overline{\mathbf{F}^{(1)}} = -\overline{\mathbf{F}^{(2)}} = \rho D^2 U^2 \{(\cos^2 \theta F_{AA} + \sin^2 \theta F_{TT}) \mathbf{e}_z + \cos \theta \sin \theta F_{AT} \mathbf{e}_x\}. \quad (3.18)$$

Here, F_{AA} is the axial force due to axial oscillation, F_{AT} is the transverse force due to coupling between axial and transverse oscillation, and F_{TT} is the axial force due to transverse oscillation, on spheres (1) and (2) as labelled in Figure 3.3.

Mesh and domain size

A mesh was generated by triangulation over a circular domain, of extent $100D$, embedding the sphere(s) at the center. The mesh consisted of a refined inner circular region close to the sphere(s), with typical grid size $0.03D$, and a coarser outer one further away (see Figure 3.4).

For a single sphere, the size of the circular domain was $100D$, with radius of the inner refined circular mesh = $60D$, and the outer coarser one having a radius of an extra $40D$. The density of mesh in the inner circle is 1.5 times that of the outer one. For two equal sized spheres, the mesh developed was similar in properties to that with a single sphere embedded at the center. Mesh dependence was checked over various combinations of domain sizes and mesh densities, given in Table 3.7. The drag forces, F_d , vary by $< 1\%$ across all the meshes, as can be seen in Table 3.8, when calculated for $0.1 \leq \Omega \leq 100$ in chapter 6 (defined in section 3.3.2, and plotted in Figure 6.9).

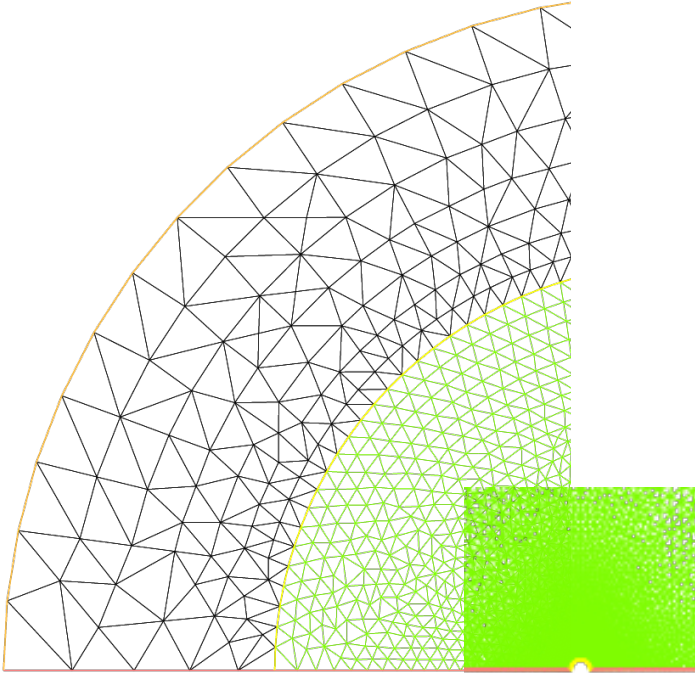


Figure 3.4: Half of the axisymmetric mesh generated for a single sphere using FreeFem++. The green inner region is more refined than the outer region. The center of the mesh is zoomed in the inset.

Table 3.7: Meshes used for mesh analysis, **M1** – **M5**, along with the parameters used, where r_{in} , r_{out} , n_{in} and n_{out} represent the radii and number of elements used for the inner and outer meshes, respectively.

Mesh	r_{in}	r_{out}	n_{in}	n_{out}
M1	10	40	15	10
M2	10	80	15	10
M3	10	40	10	5
M4	5	40	10	5
M5	10	80	30	20

In chapter 5, results are also reported for a moving sphere in a quiescent flow using WNF. It has been discussed in Fabre *et al.* (2017) that shifting to a non-inertial reference frame that travels with the body only induces a change in the second-order pressure field to account for the acceleration of the frame. There is no change kinematically, i.e. there is no change to the

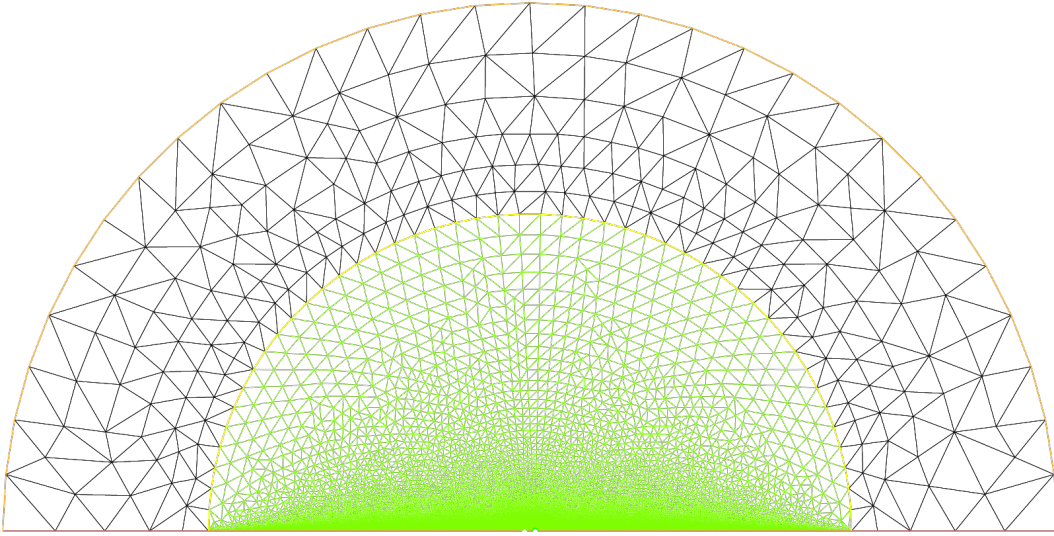


Figure 3.5: Two-dimensional mesh for two spheres placed in a lateral configuration at the center of the domain, generated using FreeFem++. The green inner region is more refined close to the spheres than the outer region.

velocity field.

3.4 Summary

In this chapter, an introduction to the equations and non-dimensional parameters involved to study steady streaming around spheres is given. Two

Table 3.8: Forces measured using WNF with different meshes, **M1** – **M5** given in Table 3.7, for $\Omega = 0.1$ and $\Omega = 100$. F_{AA} , F_{TT} , and F_{AT} are as defined in section 3.3.2.

Mesh	$\Omega = 0.1$			$\Omega = 100$		
	F_{AA}	F_{TT}	F_{AT}	F_{AA}	F_{TT}	F_{AT}
M1	1.44034	-0.103677	2.35121	-0.004678	0.345217	0.782554
M2	1.44391	-0.108278	2.35523	-0.00195161	0.343888	0.784022
M3	1.43629	-0.101821	2.34705	-0.00443296	0.342322	0.779936
M4	1.43676	-0.102702	2.348	-0.00252949	0.342554	0.778095
M5	1.44784	-0.109151	2.35664	-0.00153949	0.345294	0.786244

numerical methods, namely DNS and WNF, employed to achieve the aims of this thesis that are described at the beginning of this chapter, are briefly introduced. In the next chapter, steady streaming around a single sphere is modelled and verified against existing literature, using the DNS. A comparison of DNS and WNF will then be given in chapter 5.

Chapter 4

Verification of DNS for a Single Sphere

4.1 Introduction

The main objective of this study is to know what happens once two spherical particles under the influence of ultrasound, come close to each other i.e. whether they would attract or repel each other and what circumstances compel them to do so. In particular, the role of steady streaming affecting particle attraction (or repulsion) is explored. A numerical model is developed for a single rigid oscillating sphere and verified against literature. In order to make a comparison, a Direct Numerical Simulation (DNS) has been used as a yard stick since different parameters were used across literature.

In this chapter, steady streaming around a single sphere is modelled using DNS. The DNS is compared with literature first before moving on to the steady streaming around two spheres, addressed later in chapter 6.

4.1.1 Model for steady streaming around a single sphere

As introduced in chapter 3, section 3.3, a solid sphere of diameter D is considered, suspended in an unbounded, oscillating, incompressible stream, which oscillates sinusoidally, shown in Figure 3.1. The fluid motion is governed by the conservation principles of momentum and mass which can be expressed by the Navier-Stokes equations, as noted in section 3.2.1.

Two dimensionless parameters are defined (introduced in section 3.2.1): the inverse Strouhal number $\epsilon = A/D$ and the Reynolds number $Re = A\omega D/\nu$. Here, D is the diameter of the sphere, ω is the frequency of oscillations, A is the amplitude of the oscillation, and ν is the kinematic viscosity. For an average sized MFG of 4 μm , $\epsilon \approx O(10^{-3})$ and $Re \approx O(10^{-2})$.

Details on the development of the DNS itself, the mesh, and boundary conditions applied are given in chapter 3, section 3.3.1. Flow visualizations for $Re = 20$ and $Re = 100$ generated using the DNS are given in Figure 4.1 demonstrating small and large sizes of the inner vortices relative to the sphere. The mean streamlines in Figure 4.1 start from user selected points. For these and all subsequent flow visualizations generated in Tecplot, the color contour represents the azimuthal component of the vorticity relative to the plane where blue is inwards, and red outwards of the plane.

4.2 Comparison of DNS with Literature

As discussed in section 2.2, Lane (1955) provided theory and experiments for steady streaming around a sphere produced by an acoustic source, with

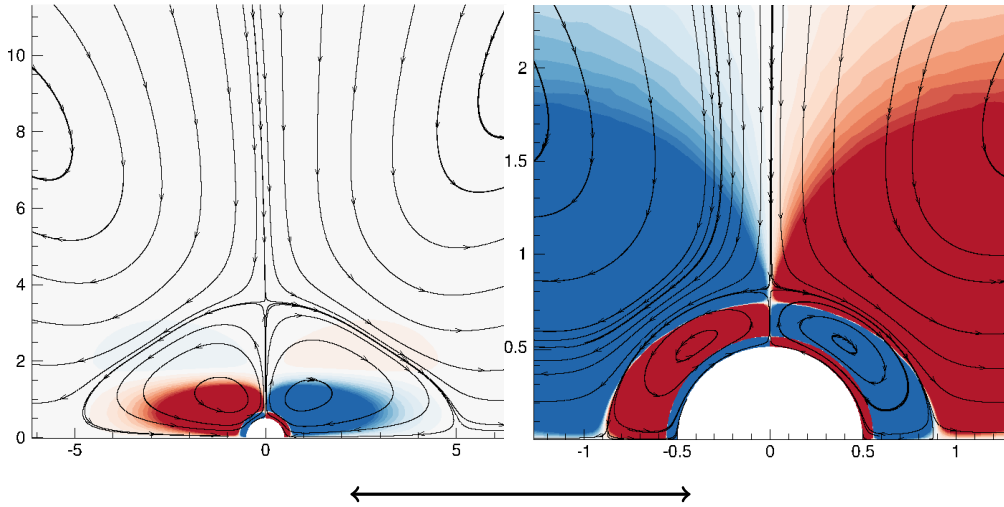


Figure 4.1: Streaming flows generated using DNS showing size of the inner vortices for a) $Re = 20$, when $\epsilon = 2.00$, and b) $Re = 100$, when $\epsilon = 0.25$. The flow is oscillating in the axial direction depicted by the bold black arrow. Rings of vortices are formed in a direction perpendicular to the axis of oscillation, along the axis of symmetry, which when sliced through a plane shows up as a pair of vortices. The colour represents azimuthal component of vorticity relative to the plane of the page, ranging from -0.01 (blue, directed inwards) to 0.01 (red, directed outwards).

a similar setup and boundary conditions applied as in the present study. A qualitative validation of DNS with the theoretical predictions of Lane is achieved, as shown in Figure 4.2. For a quantitative comparison, size of the inner vortices and peaks of drag coefficients were measured. Although the size of the inner vortices could be measured both parallel and perpendicular to axis of the imposed oscillatory flow in the numerical study carried out by Alassar (2008), the range of Re for which the results were presented was quite limited. This led to comparison of DNS results with the numerical simulation in Blackburn (2002), where $1 \leq Re \leq 100$, and the same results could further be used to make a comparison of peaks of drag coefficients.

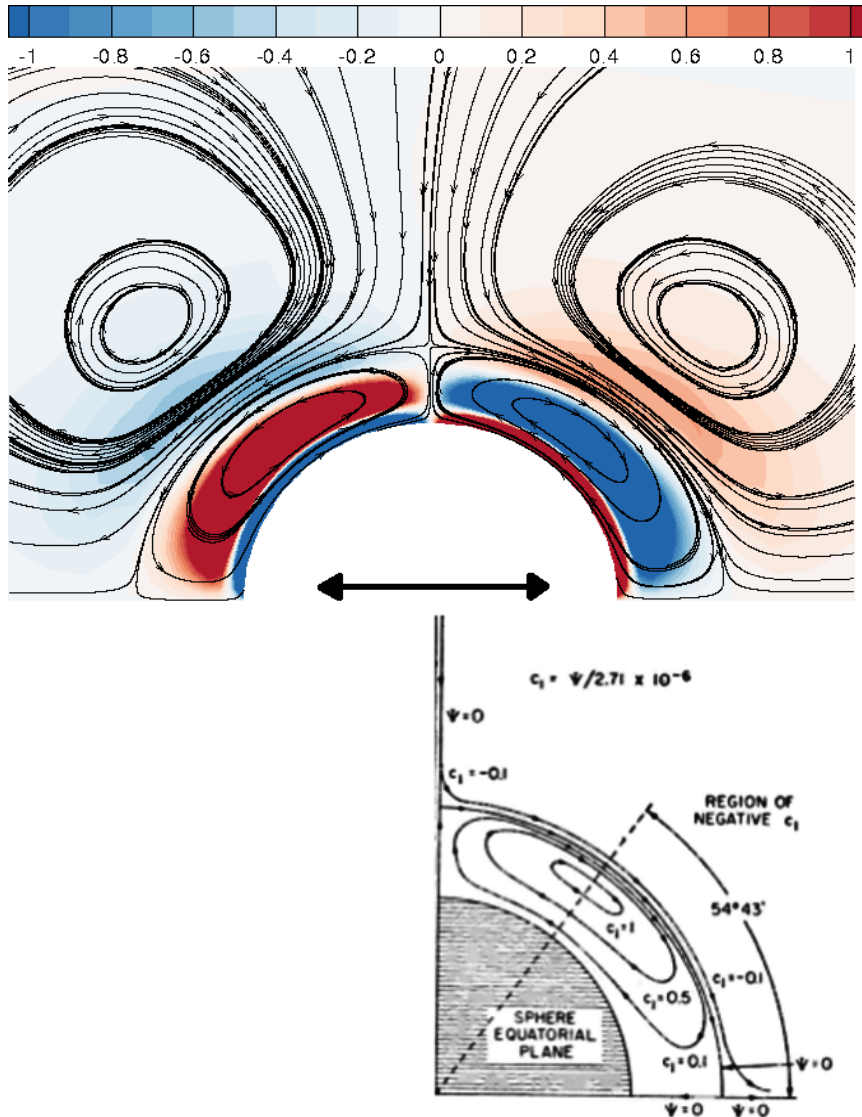


Figure 4.2: (Top) Mean velocity field showing steady streaming beyond the boundary layer region of a sphere, for dimensionless parameters $Re = 200$, $\epsilon = 0.25$. The colour contour represents azimuthal component of vorticity relative to the plane of the page, ranging from -1 to 1 . The black arrow represents axis of oscillation of the fluid in the axial (x -) direction. The streamlines start at user-selected points. (Bottom) Qualitative comparison of simulation (above) with theoretical predictions of Lane (1955) using relevant half of Figure 2.2. Reprinted with permission from Lane (1955). Copyright 1955, Acoustic Society of America.

4.2.1 Comparison of DNS with Blackburn (2002)

A mesh with a similar structure to the one used in Blackburn (2002) was constructed. The drag coefficients, C_d , were computed as

$$C_d = \frac{8F_d}{\rho U_{max}^2 \pi D^2}, \quad (4.1)$$

where $U_{max} = A\omega$ is the maximum speed of the reciprocating free stream, A is the amplitude of the oscillation, and ω is the angular frequency of oscillation. F_d is the peak drag force defined as the maximum of the integral of viscous traction and pressure over the surface of the sphere. In the DNS, $\rho = D = 1$.

The flow was axi-symmetric about the axis of the oscillating flow, $r = 0$. The rectangular mesh, with a full extent of domain = $100D$ in the axial and radial directions, was refined enough to capture the high gradients

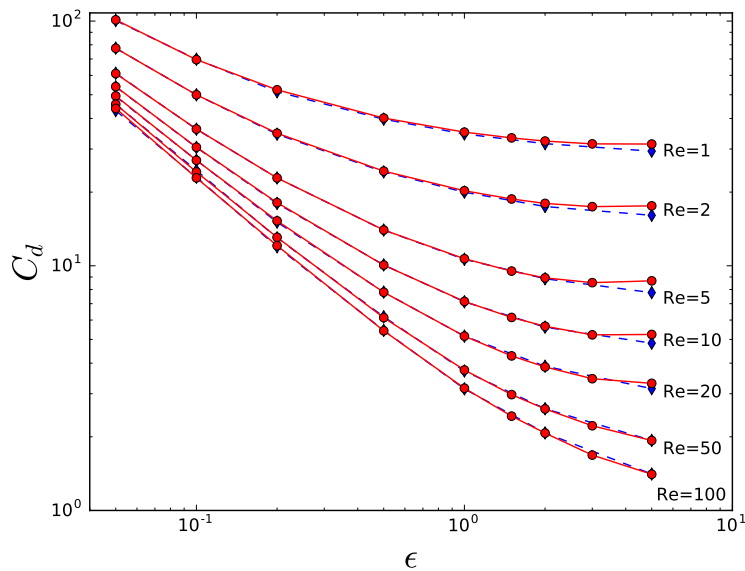


Figure 4.3: Comparison of peak coefficients of drag force, C_d , for a sphere which is placed stationary in an oscillating flow. Blackburn (2002); - -◆, DNS; —●. For $\epsilon \leq 1$, both numerical methods match Basset (1888).

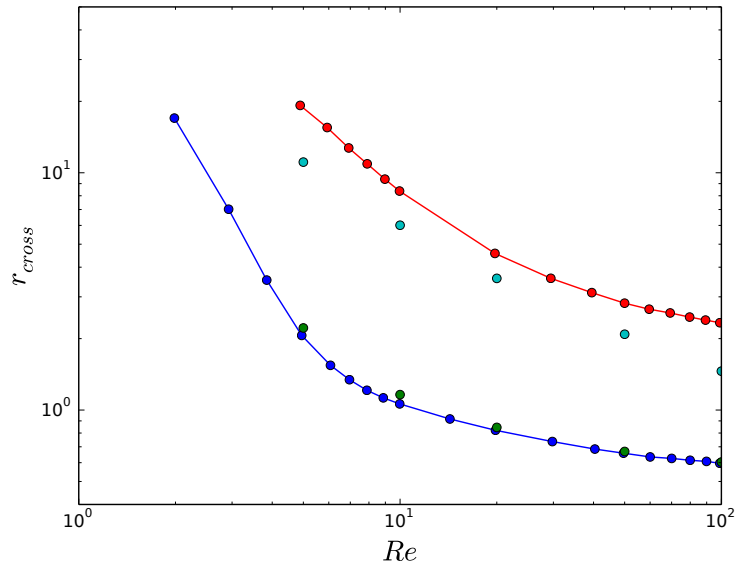


Figure 4.4: Location of the first zero-crossing of radial velocity on the line $x = 0$, r_{cross} , as a function of Reynolds number Re , for $\epsilon=0.05$, and $\epsilon=5.0$. Blackburn (2002); —●— $\epsilon = 0.05$, —●— $\epsilon = 5.0$. DNS; ● $\epsilon = 0.05$, ● $\epsilon = 5.0$.

near the boundary of the sphere, as discussed in section 3.3.1. The outer mesh further away from the sphere was coarse to save computational time. The peak coefficients of drag force, C_d , for a stationary sphere in oscillatory flow were computed as a function of Re using the DNS, shown in Figure 4.3. It matched well with Blackburn (2002) for $1 \leq Re \leq 100$ when $0.05 \leq \epsilon \leq 5$. Differences occur only for $Re \leq 10$ and $\epsilon > 3$ which is irrelevant for the range of parameters considered for the present work. It is worth noting that Blackburn (2002) in turn matched with Basset’s analytical solution (Basset, 1888) for amplitudes $\epsilon \leq 1$.

For a further verification of DNS, sizes of inner vortices were compared with Blackburn (2002) by measuring the distance to stagnation points on the axis of oscillation as shown in Figure 4.4. This length was measured by recording points where velocity in the x and r direction first crossed its

respective axis, denoted by r_{cross} . The maximum extent of radial domain was $100D$ for DNS, and $50D$ in Blackburn (2002).

Data for r_{cross} is available only for $\epsilon = 0.05$ and $\epsilon = 5.0$ in Blackburn (2002). Figure 4.4 shows that the size of the inner vortices, r_{cross} , reduces as Reynolds number, Re , increases. This is also evident since the viscous effects are large close to the sphere, thus shrinking the boundary layer in size. However, r_{cross} can grow as large as the extent of the domain for small Re . Hence, data is not considered reliable at those points.

It should be noted that though the measure of drag forces is independent of the mesh density, r_{cross} certainly increased when the mesh was further refined close to the sphere, keeping the number of periods of oscillation of the flow constant. It should be recalled that r_{cross} is the point at which the mean velocity reverses its sign. For low Re and Ω (defined in section 3.3), this mean velocity field can be extremely weak, and hence small changes in this mean velocity field due to changes in the mesh can induce very large changes in the position of this change of sign, with only a negligible variation in the forces. The effects of mesh density on F_d and r_{cross} are quantified in Tables 3.3 and 3.4 in section 3.3.1. It was noted that r_{cross} increased to 144% between meshes M2 and M3 for $Re=1$ when $\epsilon = 0.05$.

Also, when the number of periods over which the average was taken was doubled to that in M4, yet again there was a significant increase noted in r_{cross} (41% for $Re=40$, $\epsilon = 0.05$), specifically for small ϵ and high Re , as shown in Tables 3.5, and 3.6. However, it took two weeks to get all the data points required for results in section 5.2 using this setup, in comparison to only three days taken in the case of M4. Thus, the computational effort

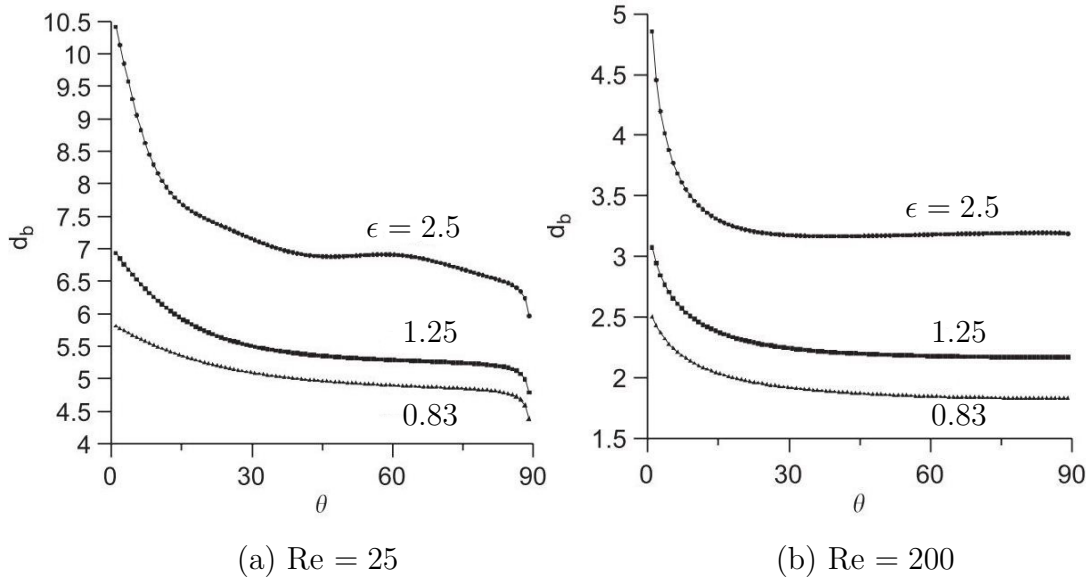


Figure 4.5: d_b denotes the size of inner vortices varying with θ , and measured from the center of the sphere. Here, $\epsilon = 0.5/S$, where S is the inverse Strouhal number. This Figure will be used to make a comparison with the results in Figure 4.6. Reprinted from Alassar (2008), Copyright (2008), with permission from Elsevier.

required to converge these values of r_{cross} is considerable without any real change in the forces and the flow near the sphere. Hence, it can be concluded that the mesh setup used is a compromise between accuracy and time taken to achieve the results, in spite of the sensitivity of the value of r_{cross} to the mesh density, and the number of periods of oscillation of the flow.

4.2.2 Comparison of DNS with Alassar (2008)

In Blackburn (2002), r_{cross} was measured only in one direction, i.e. when flow was parallel to the axis of oscillation. The DNS allows it to be measured perpendicular to the axis of oscillation as well. Alassar (2008) measured size of the inner vortices, naming it d_b , for $0^\circ \leq \theta \leq 90^\circ$.

Alassar (2008) defined two dimensionless parameters: the inverse Strouhal number, $S = 2A/D = 0.5/\epsilon$, and the Reynolds number, $Re = A\omega D/\nu$, where ϵ and Re are defined earlier in section 4.1.1. In order to verify DNS for $Re = 25$ and $Re = 200$, results were produced matching Alassar's parameters, for lengths of stagnation points on either side of the sphere i.e. for $\theta = 0^\circ$ (x -axis) and $\theta = 90^\circ$ (r -axis). A good agreement between the two was achieved, as shown in Figure 4.6. The results were averaged over the last 10 periods after running for 100 periods of oscillation. It is observed that in Figures 4.5 and 4.6, as ϵ decreases, the distance from the surface of the sphere to the stagnation point becomes smaller. Also, it is evident that the shape of the inner vortical regions is not constant over θ . The plots in these figures are drawn considering $S = 0.5/\epsilon$ for the purpose of comparison with Alassar (2008).

So far the DNS was verified against literature for the model explained in 4.1.1, i.e. streaming flows for a stationary sphere placed in an imposed oscillatory flow. However, steady streaming can also be generated when a sphere is oscillating in a quiescent fluid (e.g. Riley (1967)). A comparison of results produced using DNS for these two flows is discussed in the next section.

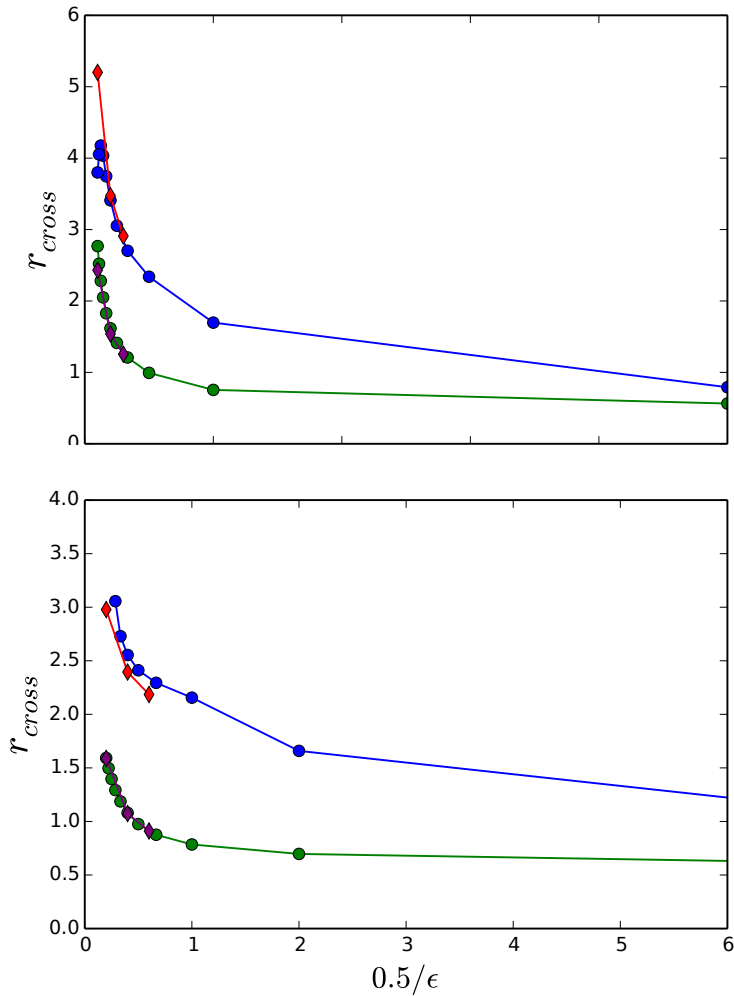


Figure 4.6: Size of the inner vortex, r_{cross} , measured (above) over the x -axis corresponding to $\theta = 0^\circ$, and (below) over the r -axis corresponding to $\theta = 90^\circ$. Alassar (2008); —●— $Re = 25$, —●— $Re = 200$. DNS; —◆— $Re = 25$, —◆— $Re = 200$.

4.3 Steady Streaming Flows in Relative and Absolute Frames

When ultrasound is switched on in a stationary tank filled with milk, the spherical Milk Fat Globules (MFGs) start oscillating with an amplitude much smaller than their radius in an initially quiescent fluid at that instant. Seeing

it from a different perspective, the problem can also be modelled as stationary spheres placed in an imposed oscillatory flow since there is an outer flow applied in the form of ultrasound. In the simulations produced using DNS, the sphere is assumed stationary and oscillatory boundary conditions are imposed, referred to as an absolute frame. Since the separation of milk using ultrasound is a combination of these, results for the two problems stated above were verified.

Simulating oscillating spheres in a quiescent fluid needs a new mesh constructed each time the sphere moves to a new position and that makes it computationally expensive to use DNS. This problem was overcome by shifting the frame of reference involved, referred to as relative frame here. In this case, the equations of momentum in the governing equations defined in section 3.2 will have an additional term for the acceleration of the reference frame. This extra term will be subtracted from the right side of the equation for conservation of axial momentum, equation (3.5), i.e.

$$\begin{aligned} \frac{\partial w^*}{\partial t^*} + u^* \frac{\partial w^*}{\partial r^*} + \frac{v^*}{r^*} \frac{\partial w^*}{\partial \vartheta} + w^* \frac{\partial w^*}{\partial x^*} = -x^* \omega^2 \sin(\omega t^*) - \frac{1}{\rho} \frac{\partial p^*}{\partial x^*} + \\ \nu \left\{ \frac{1}{r^*} \frac{\partial}{\partial r^*} \left(r^* \frac{\partial w^*}{\partial r^*} \right) + \frac{1}{r^{*2}} \frac{\partial^2 w^*}{\partial \vartheta^2} + \frac{\partial^2 w^*}{\partial x^{*2}} \right\}. \end{aligned} \quad (4.2)$$

After non-dimensionalizing this equation using the dimensionless parameters introduced in equation (3.6), it yields,

$$\begin{aligned} \Rightarrow \frac{\partial w}{\partial t} + u \frac{\partial w}{\partial r} + \frac{v}{r} \frac{\partial w}{\partial \vartheta} + w \frac{\partial w}{\partial x} = -\frac{x}{\epsilon} \sin(t) - \frac{P}{U} \frac{\epsilon}{\rho} \frac{\partial p}{\partial x} + \\ \nu \left\{ \frac{1}{r} \frac{\partial}{\partial r} \left(r \frac{\partial w}{\partial r} \right) + \frac{1}{r^2} \frac{\partial^2 w}{\partial \vartheta^2} + \frac{2}{r^2} \frac{\partial u}{\partial \vartheta} - \frac{v}{r^2} + \frac{\partial^2 w}{\partial x^2} \right\} \end{aligned} \quad (4.3)$$

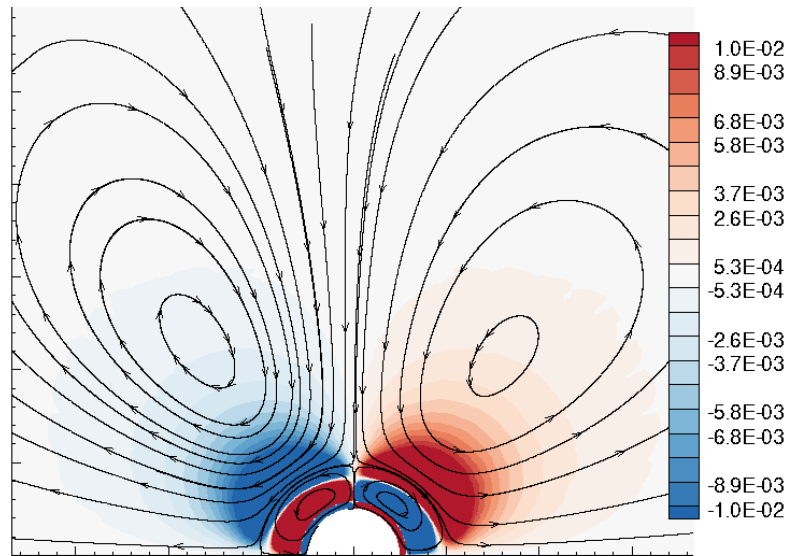


Figure 4.7: Streaming around a sphere in an oscillating flow, for $Re = 50$, $\epsilon = 0.20$. The contours represent azimuthal component of vorticity.

4.3.1 Streaming flow around a stationary sphere in an oscillatory flow

The mean of the streaming flow around a stationary sphere placed in a oscillatory flow was computed using DNS, without taking into account coupling between the sphere and the fluid i.e. velocity of the fluid is zero at the surface of the sphere. After 100 periods of oscillations, 50 snapshots were taken over one period, equispaced in time, which were then averaged. The outcome is shown in Figure 4.7 with mean streamlines. The respective comparison for peak coefficients of drag were given in Figure 4.3, already discussed in section 4.2.1.

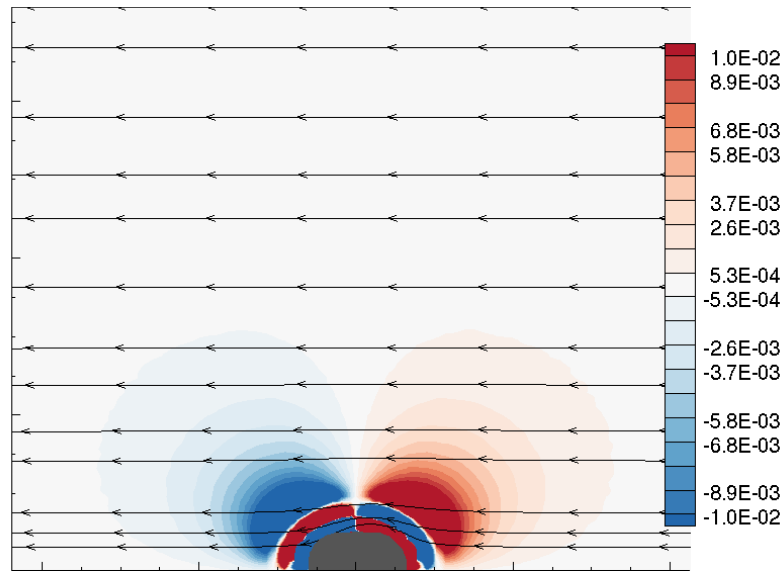


Figure 4.8: Mean streaming for a sphere oscillating in a quiescent flow initially, for $Re = 50$, $\epsilon = 0.20$. The contours represent azimuthal component of mean vorticity.

4.3.2 Streaming flow around an oscillatory sphere in a quiescent flow

The streaming flow around an oscillating sphere placed in quiescent fluid was computed using DNS, by taking the mean of the flows after 100 periods of oscillations is shown in Figure 4.8. Again snapshots at 50 different and equispaced time steps were taken. A mean of these 50 flow snapshots was computed using Tecplot. Due to changing positions of the sphere, it creates an offset from its initial position. The inside of the sphere is irrelevant to the flow around the sphere, thus that part of the flow is coloured grey.

After a qualitative comparison of streaming flows generated by an oscillatory sphere, drag forces of the flow were compared with available literature. It matches quite well for streaming flow around an oscillating sphere

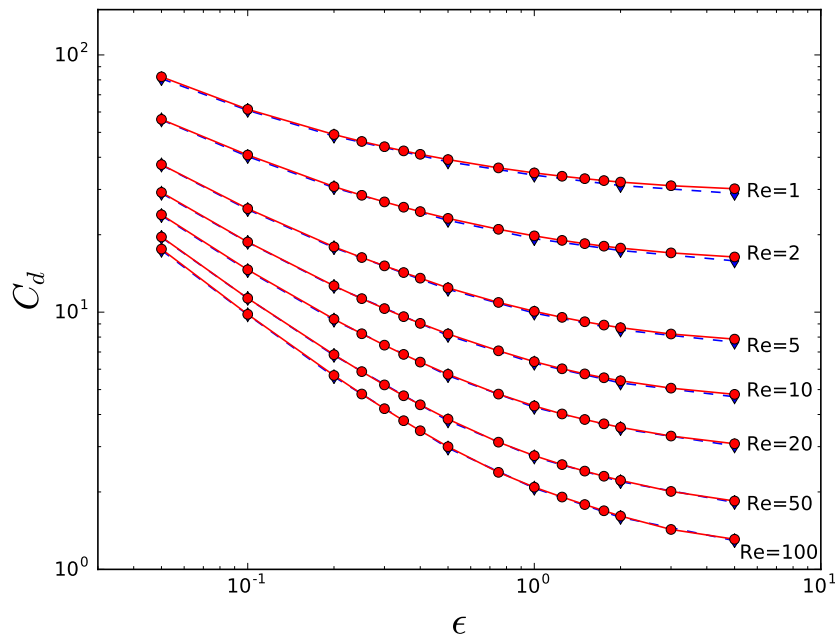


Figure 4.9: Comparison of peak coefficients of drag force, C_d , for a sphere oscillating in a quiescent flow. Blackburn (2002); - \blacklozenge , DNS; — \bullet . For $\epsilon < 1$, both numerical methods match Basset (1888).

in a quiescent fluid for $1 \leq \text{Re} \leq 100$, and $0.05 \leq \epsilon \leq 5$ when compared with Blackburn (2002), as shown in Figure 4.9. A similar comparison of peak coefficients of drag forces, C_d , for another type of flow i.e. an oscillatory flow around a stationary sphere, is already presented in Figure 4.3 and is known to be different.

4.4 Summary

The DNS has been successfully verified quantitatively and qualitatively, against the literature. The comparison was made by measuring drag forces and sizes of the inner vortices.

A comparison of drag forces, computed using DNS, was carried out

for streaming flows between the oscillatory spheres in quiescent fluid and stationary spheres placed in oscillatory fluid. The separation of Milk Fat Globules (MFGs) under the influence of ultrasound can be considered as a combination of these two flows, as discussed at the beginning of section 4.3. The flows are intrinsically different but share some common features. These two flows are compared and discussed again at the end of the next chapter.

In the next chapter, results from DNS will be presented alongside the ones from the Weakly Non-linear Formulation (WNF), to compare behaviour of the steady streaming flow involved.

Chapter 5

Steady Streaming around a Single Sphere using DNS and WNF

5.1 Introduction

In chapter 4, a full DNS was applied verified for a single sphere. Those DNS results are used in order to verify another numerical method, namely WNF in this chapter. The shift from DNS to WNF was required because the development of DNS for two spheres in three-dimensions would be very time consuming. This new method is much faster than the DNS, especially for steady streaming flows around two spheres, and quite accurate as well.

In the next section, a perturbation method is introduced to calculate forces exerted on a single sphere solving the weakly non-linear equations, referred to as Weakly Non-Linear Formulation (WNF) henceforth and

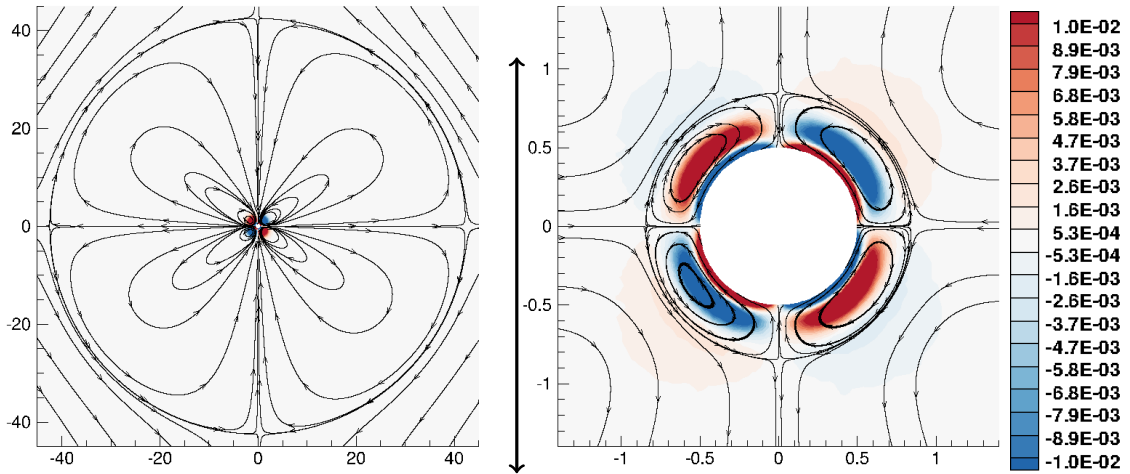


Figure 5.1: Steady streaming around a single sphere oscillating in the direction of the bold black arrow, for $\Omega = 1$ (left), and $\Omega = 100$ (right), using WNF. Recall that the basis of WNF is that $\epsilon \rightarrow 0$. Rings of vortices form perpendicular to the axis of oscillation and show up as a pair of vortices when sliced through in two-dimensions. The contours represent the azimuthal component of vorticity, as explained in section 4.1.1.

as detailed in chapter 3. More details on the theory involved are given in Fabre *et al.* (2017). The flow was computed and visualized using FreeFem++ (Hecht, 2012). In addition to computing streaming flows parallel and perpendicular to the imposed oscillatory flow, WNF allows for any angle between the axis of oscillation of the sphere and the imposed oscillatory flow, unlike the axisymmetric DNS. This feature has benefit in computing trajectories of particles, discussed in chapter 7.

5.1.1 Model for steady streaming around a single sphere using WNF

For a single sphere of unit diameter D , an unbounded, incompressible fluid was assumed to be oscillating axially with an amplitude A , and frequency ω .

More details for the model were given in section 3.3.2.

The non-dimensional parameters are defined, as before, as $\epsilon = A/D$, described in the literature as inverse Strouhal number, and Reynolds number $\text{Re} = A\omega D/\nu$, where D is the diameter, ω is the frequency of the oscillating flow, and ν is the kinematic viscosity. When WNF is applied, a ratio of Re and ϵ is introduced as $\Omega = \omega D^2/4\nu$, also known as Stokes number, as described earlier in section 3.2.2. In the case of WNF it is assumed that $\epsilon \rightarrow 0$ as is necessary for the perturbation expansion leading to WNF to be valid. The range of parameters used is given in Table 5.1.

Table 5.1: Parameter space used for both the DNS and WNF. As defined in section 2.2, $4\Omega = \text{Re}/\epsilon$, $\text{Re}_s = \epsilon\text{Re}$, and $\delta = \sqrt{\nu/\omega}$.

Parameter	Minimum	Maximum
ϵ	0.01	5.0
Re	1	500
δ	0.05	0.5
Ω	0.05	12500
Re_s	0.01	2500

In Figure 5.1, steady streaming flows for $\Omega = 1$ and $\Omega = 100$ around a single sphere oscillating in the axial direction are presented. The inner recirculation regions are much larger for low Ω as compared to high Ω . This large inner recirculation region can be a result of high viscosity which controls the flow when frequency is low. For very low values of Ω , the inner recirculation can be very large and gets dependent on the size of the domain. This flow behaviour can be related to what Riley (1966, 1967) described for $4\Omega \ll 1$ and $4\Omega \gg 1$ discussed in section 2.2, and illustrated in Figure 2.3.

Rings of vortices form perpendicular to the axis of oscillation in Figure 5.1, and show up as a pair of vortices when sliced through in two-dimensions, represented by opposite colours. The vortex axis is defined as the normal to the plane in which the circle at the center of the vortex-ring is contained. The colours in Figure 5.1, and in subsequent visualizations, represent the azimuthal component of vorticity, as explained in section 4.1.1. Flows for both low and high Ω , shown in Figure 5.1, can be compared qualitatively with predictions of Lane (1955). The orientation of the streamlines around the sphere in Figure 2.2 is the same to that in Figure 5.1 according to the direction of the axis of oscillation.

The DNS allows integration of the full Navier-Stokes equations, without any assumptions for simplifications. This helped capturing many effects in the flow that were not possible with WNF. On the other hand, it made DNS more time consuming than WNF. In the next section, a comparison of DNS and WNF is presented, highlighting the accuracy of the WNF approach and outlining where it is, and is not, valid.

5.2 Comparison of Results from WNF with DNS

Steady streaming flows around the spheres in Figure 5.2, computed using DNS and WNF, are compared qualitatively. They also agree qualitatively with the theoretical predictions of Lane (1955) (Figure 4.2) such that the size and the orientation of the vortices is the same inside and outside of the

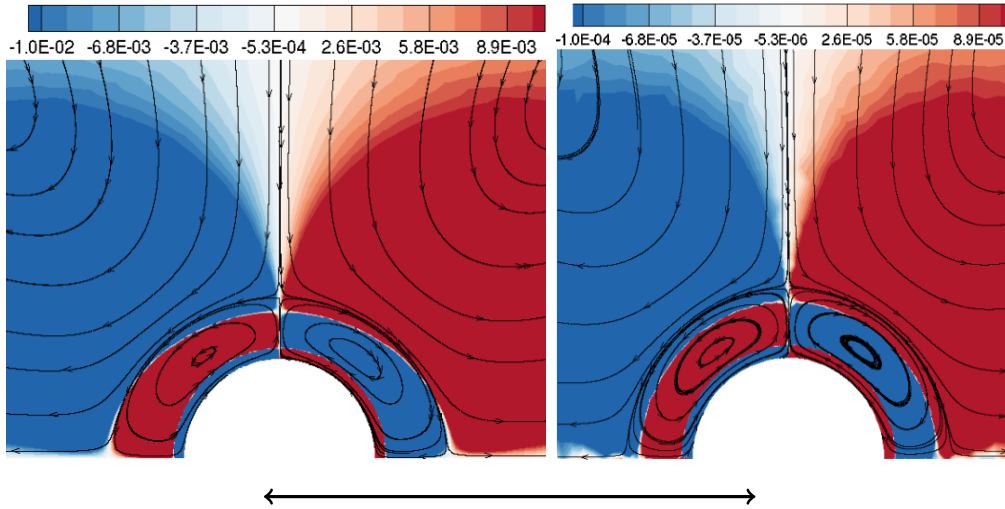


Figure 5.2: Flows generated using: (left) DNS for $Re = 100$, when $\epsilon = 0.25$, and (right) WNF for $\Omega = 100$, when $D = 1$ in both cases. Contours represent azimuthal component of vorticity as described in section 4.1.1. Streamlines are generated from user-selected points, hence can not be exactly replicated in another attempt. The bold black arrow depicts the imposed oscillating flow in the axial direction. Recall that WNF is based on infinitesimal amplitude, however, vorticity in the flow can be scaled. The aspect ratio of the images was made slightly different so that the spheres would appear of the same size, owing to the use of axisymmetric and Cartesian domains for the DNS and WNF respectively.

boundary layer.

For a quantitative comparison, the size of the inner vortices, r_{cross} , computed using DNS and WNF were compared first. A comparison of peaks of drag coefficients will follow.

5.2.1 Comparison of size of the inner vortices

The size of the inner vortices, r_{cross} , was measured as the distance from the center of the sphere to the stagnation points on either side of the sphere, as was done in chapter 4, section 4.2.1. For DNS and WNF, r_{cross} was quantitatively compared in the directions parallel and perpendicular to the imposed

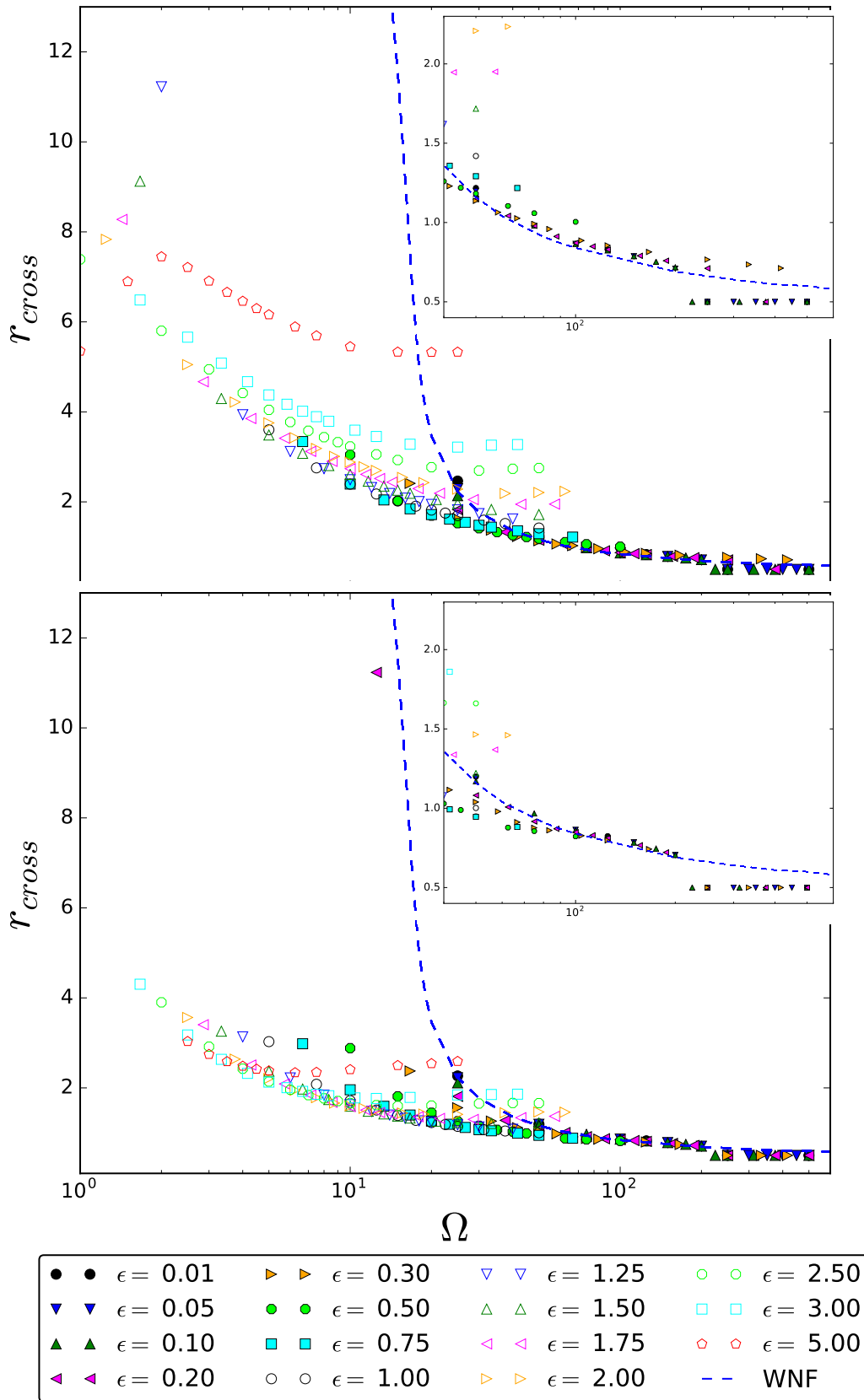


Figure 5.3: Symbols denoting DNS data for length of inner vortices, r_{cross} , plotted against Ω , and its comparison with WNF data. (above) Parallel to the direction of the imposed oscillation (x -axis); (below) perpendicular to the direction of the imposed oscillation (over the r -axis). (Insets) Same plots for $40 \leq \Omega \leq 600$.

oscillation, as shown in Figure 5.3. It was observed that r_{cross} decreases when Ω increases, for $1 \leq \Omega \leq 500$, in both these cases. Also, r_{cross} was not the same size over the axial and radial axes, when the imposed oscillation is axial. This suggests that the size of the inner recirculation region is not symmetric over $0^\circ \leq \theta \leq 90^\circ$, something that is also reported in Alassar (2008).

In Figure 5.3, the DNS data gradually collapses onto the WNF curve for $\Omega > 40$ when $\epsilon \leq 1$. It shows that r_{cross} is independent of ϵ in this range. The low ϵ DNS results fall on a single curve similar to the curve from WNF. This indicates the WNF results are valid for finite ϵ , with an upper limit at $\epsilon = 1.00$. Therefore, the results from WNF, where it is assumed that $\epsilon \rightarrow 0$, are also valid for values of $\epsilon \leq 1$.

For a Milk Fat Globule (MFG) of an average diameter of $4 \mu\text{m}$ exposed to mega hertz frequencies, $\Omega \approx 25$. For the largest MFGs of diameter up to $10 \mu\text{m}$, $\Omega \approx 160$. Recall that during the application of ultrasound, the amplitudes of oscillation are very small, with $\epsilon = 10^{-3}$. Therefore, it seems that the WNF approach is able to capture the same dynamics as the fully non-linear DNS for parameters in the range of interest, $25 < \Omega < 160$, for the milk separation application.

The data tends to gradually leave the curve of collapse for $1 \leq \Omega \leq 25$ when $\epsilon \geq 0.75$. This range of ϵ is not of interest for the milk separation as just discussed above. Since $\Omega \leq 25$ also refers to small size of the spheres, it suggests that MFGs $< 4 \mu\text{m}$ will not get removed from the milk in this cream separation process. There is evidence of MFGs smaller than this size remaining suspended in the milk even after ultrasonication, in experiments conducted by Leong *et al.* (2016).

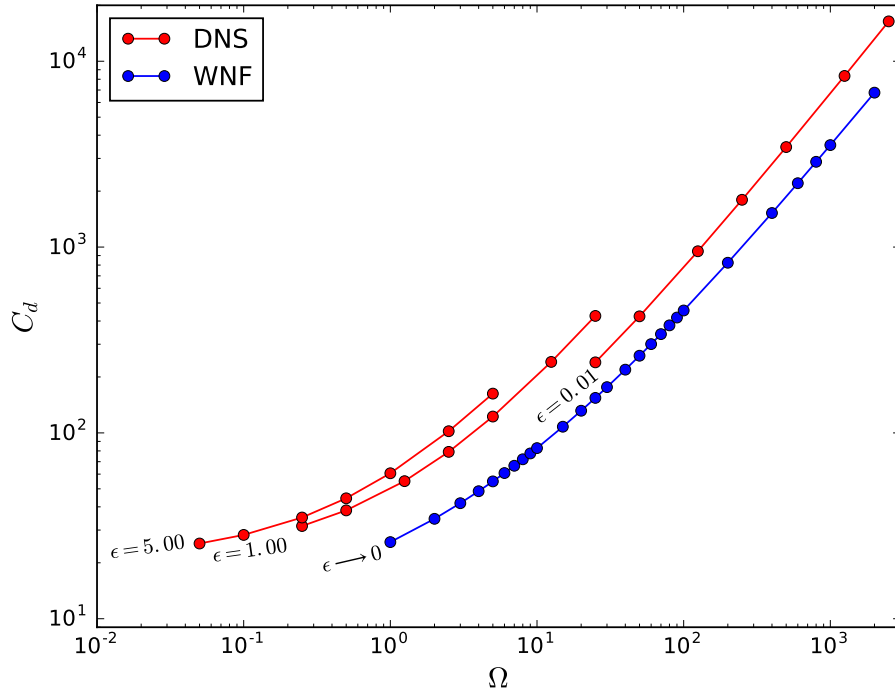


Figure 5.4: Comparison of peaks of drag coefficients C_d for DNS and WNF, when a stationary sphere is placed in an oscillatory flow. As ϵ is reduced, the DNS results tend to the WNF result where $\epsilon \rightarrow 0$.

5.2.2 Comparison of peak coefficients of drag

The drag forces, F_d , calculated by WNF were non-dimensional. The DNS coefficients of drag force given in equation (4.1), C_d , were re-defined in order to make a comparison with amplitudes $\epsilon \rightarrow 0$, as

$$C_d = \frac{2F_d}{\rho U_a \nu D}, \quad (5.1)$$

where as before, $U_a = A\omega$ is the speed of free stream, A is the amplitude of the oscillation, ω is the angular frequency of oscillation, and F_d is the drag force. This redefinition was necessary to quantify U_a , since amplitude A is

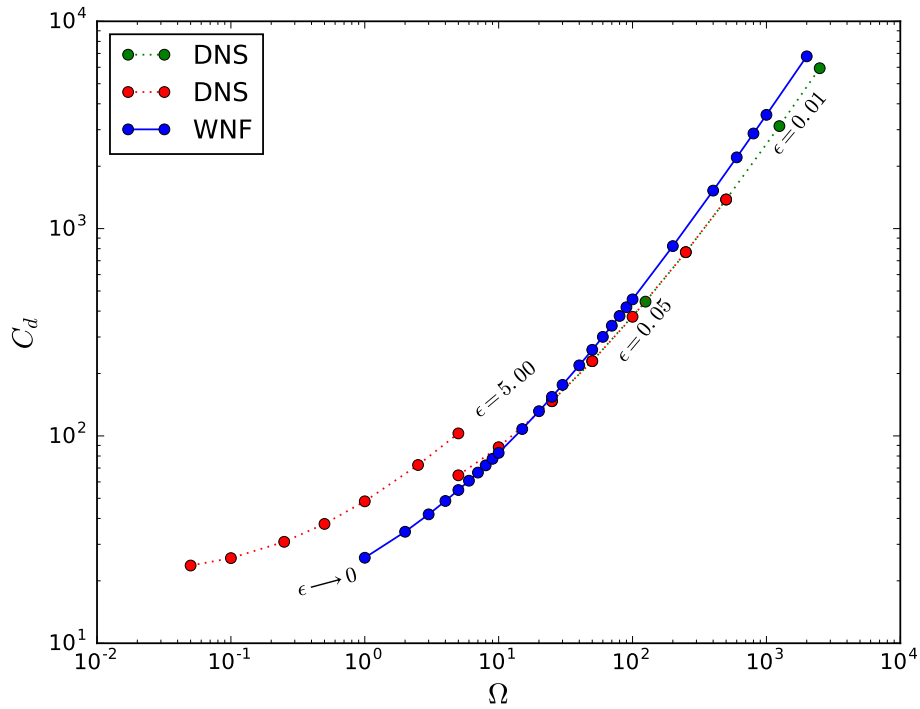


Figure 5.5: Comparison of peaks of drag coefficients, C_d , for DNS and WNF, for an oscillating sphere placed in a quiescent flow. Parts of DNS curves for $\epsilon = 0.01$ and $\epsilon = 0.05$ are overlapping each other.

infinitesimal in WNF as $\epsilon \rightarrow 0$.

In Figure 5.4, a comparison of peaks of C_d computed using DNS and WNF data, on a single sphere placed in an imposed oscillatory flow is made. The DNS data for this flow was computed via the process explained previously in section 4.3.1. It involved amplitudes $0.05 \leq \epsilon \leq 5.00$, and $1 \leq \text{Re} \leq 100$. These parameters were converted to Ω , in order to make a comparison with data from WNF, where $\epsilon \rightarrow 0$.

A comparison of peaks of C_d from DNS with WNF data when an oscillating sphere is placed in a quiescent flow is shown in Figure 5.5. The details of how data was obtained is explained in section 4.3.2.

Both plots of comparison of peaks of C_d show that as ϵ is reduced, the DNS results converge to the WNF result where $\epsilon \rightarrow 0$. It can be observed in Figure 5.4 that the WNF curve for $\epsilon \rightarrow 0$ is sitting below DNS curves for $0.05 \leq \epsilon \leq 5.00$. The results do not converge perfectly to the WNF results in Figure 5.5 for the oscillating sphere case and are left for resolution in future

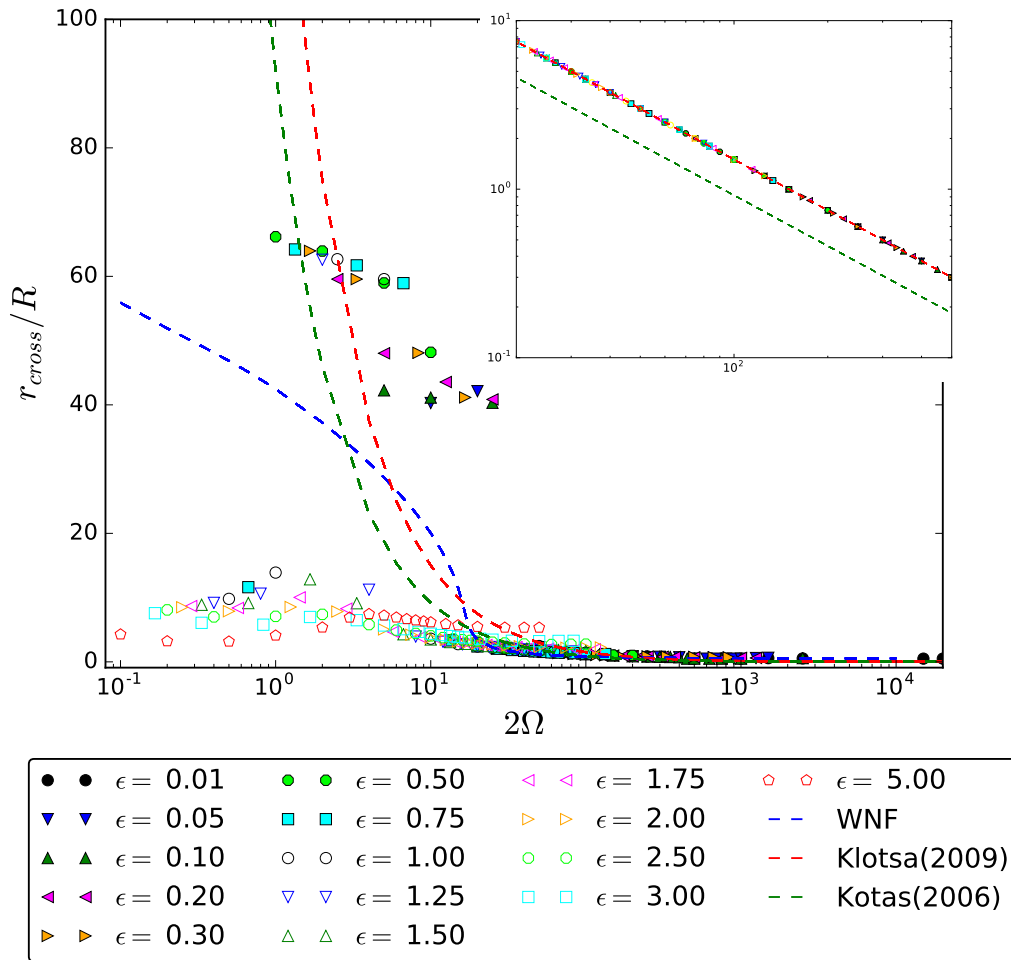


Figure 5.6: The comparison of DNS data on a log-log plot and a semi-log plot of r_{cross} as a function of Ω replicating variables defined by Klotza (2009). (Inset) The same plot on a log-log scale for the range of data presented in Klotza (2009). Klotza (2009), $75/\Omega$; - -, Kotas *et al.* (2006), $46/\Omega$; - -.

work. Both DNS and WNF will need to be investigated for flows at low ϵ to check convergence for a more refined mesh. In addition, for such a refined mesh, the effects of increasing the number of periods of oscillation before taking average of the flow should be checked.

5.3 Classification of Flow Regimes

Klotsa (2009) compared results from simulations for a single sphere with that of Kotas *et al.* (2006) in order to compare length of the inner vortical regions. The relation was given as $r_{cross}/R = C/2\Omega$, where r_{cross} is the length from the surface of the sphere to the stagnation point as defined before in 4.2.1, R is the radius of the sphere, and $C = 150 \pm 1$. The range of parameters for simulations done by Klotsa (2009) is restricted i.e. $2 \leq \text{Re} \leq 200$, providing only 9 points in the data set, which over-estimate stagnation point distances given in Kotas *et al.* (2006). In comparison, results from DNS and WNF, are computed on a much wider range i.e. $1 \leq \text{Re} \leq 500$, and $0.01 \leq \epsilon \leq 5.00$.

In Figure 5.6, data is scaled and plotted as in Klotsa (2009). A good match can be seen in the inset of Figure 5.6, where data was plotted on a log-log plot. However, when plotted on a semi-log plot and for a wider range of parameters, it shows more detail that was lost on a log-log plot. There are different trends followed by the DNS data especially, that can be classified into regimes according to the nature of the flow.

According to data from DNS, shown in Figure 5.7, steady streaming flow around a single oscillating sphere can be grouped into four possible regimes:

- Zone I: Moderate Ω and Low ϵ , ($1 \leq \Omega \leq 10$, $0.01 \leq \epsilon < 1.00$): As Ω increases, r_{cross} decreases, staying above the WNF curve without any particular dependence on ϵ . In Figure 5.8 (a), it can be seen that for low values of Ω and ϵ , r_{cross} is much wider as compared to the diameter, D , of the sphere.
- Zone II: Moderate Ω and High ϵ , ($1 \leq \Omega \leq 10$, $1.00 \leq \epsilon \leq 5.00$): As ϵ increases, data tends to gradually move away from the curve it seems to collapse to in Zone III. With the increase in ϵ , r_{cross} decreased due to the outer vortices surrounding the inner vortices, as demonstrated in Figure 5.8 (b) for $\Omega = 5$ and $\epsilon = 5.00$.
- Zone III: High Ω , ($\Omega > 10$): Data collapses down on WNF curve and is independent of ϵ . In Figure 5.8 (c), the inner vortices becomes confined by the outer vortices such that r_{cross} is small compared to the diameter, D , of the sphere.
- Zone IV: Low Ω and High ϵ , ($0.1 \leq \Omega \leq 1$, $1.00 \leq \epsilon \leq 5.00$): As Ω increases, r_{cross} increases, depending on ϵ in addition. The inner vortices are seen extending over a much wider region in Figure 5.8 (d).

It should be noted that Ω can also be expressed in terms of thickness of the boundary layer $\delta = \sqrt{\frac{\nu}{\omega}}$, as $\Omega = D^2/4\delta^2$. This dependence of r_{cross} on δ is clearly observed in Zones IV and III. However, for Zones I and II, ϵ turned out to be a significant parameter.

Also, the WNF curve shows a different behaviour than the DNS data for $\Omega < 10$. For such values and for lower values of Ω , r_{cross} is very

large, sometimes as large as the extent of the domain. These points require higher mesh resolution for precise calculation of small changes in the flow. However, the data match is good for the range of interest for milk separation i.e. $25 \leq \Omega \leq 160$.

Table 5.2: Distribution of oscillatory flow regimes around a single sphere into zones.

Ω/ϵ	Low ($0.01 \leq \epsilon < 1$)	High ($1 \leq \epsilon \leq 5$)
Low ($0.1 \leq \Omega \leq 1$)		Zone IV
Moderate ($1 \leq \Omega < 10$)	Zone I	Zone II
High ($\Omega \geq 10$)	Zone III	Zone III

As described in chapter 2, section 2.2, Riley (1967) has classified steady streaming flows induced by a sphere oscillating in a viscous fluid, into different cases for amplitudes $\epsilon \ll 1$. A comparison of flow regimes explained in Table 5.2 proved that flow in Zones I, III, and IV was the same as in Case I, III, and IV explained by Riley (1967) (given in section 2.2), and thus named in a similar fashion. However, Zone II was not discussed as all the study was limited to cases only when $\epsilon \ll 1$.

5.4 Summary

Steady streaming flows around a single sphere were generated using DNS and the perturbation-based method WNF, which have been verified qualitatively and quantitatively. These results were produced for a range of parameters much wider than studied in literature previously. For high amplitudes $1 \leq$

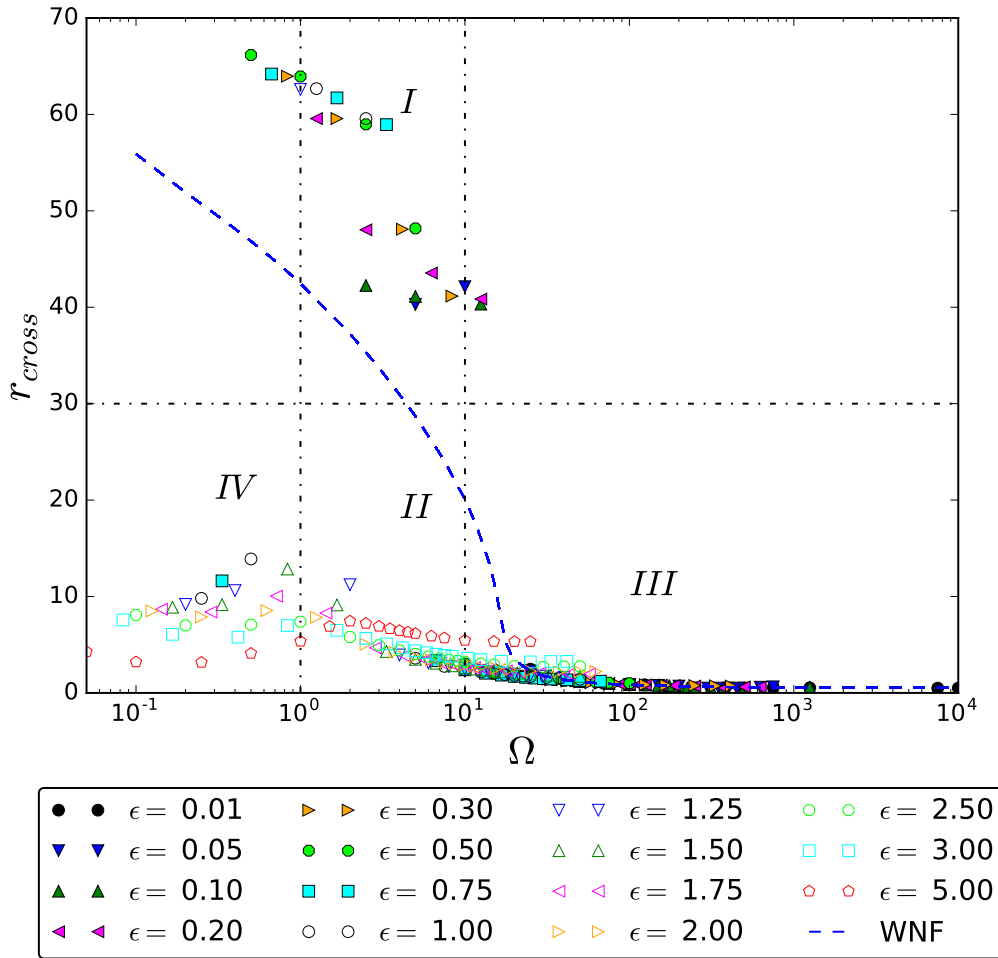


Figure 5.7: Distributing flow regimes into zones, explained in Table 5.2, according to different trends followed by the steady streaming flow simulated around a sphere in an oscillating flow using DNS, and its comparison with WNF. Recall from section 5.2.1 that WNF is only comparable for $25 < \Omega < 60$.

$\epsilon \leq 5$, DNS data showed the presence of a different flow regime, namely Zone II as shown in Figure 5.7, that has not been discussed in the literature. DNS was also capable of capturing the non-symmetric nature of the sizes of the inner vortices, seen in Figure 5.8.

However, DNS is limited to steady flows around a single sphere unless fully three-dimensional simulations are conducted, which is very expen-

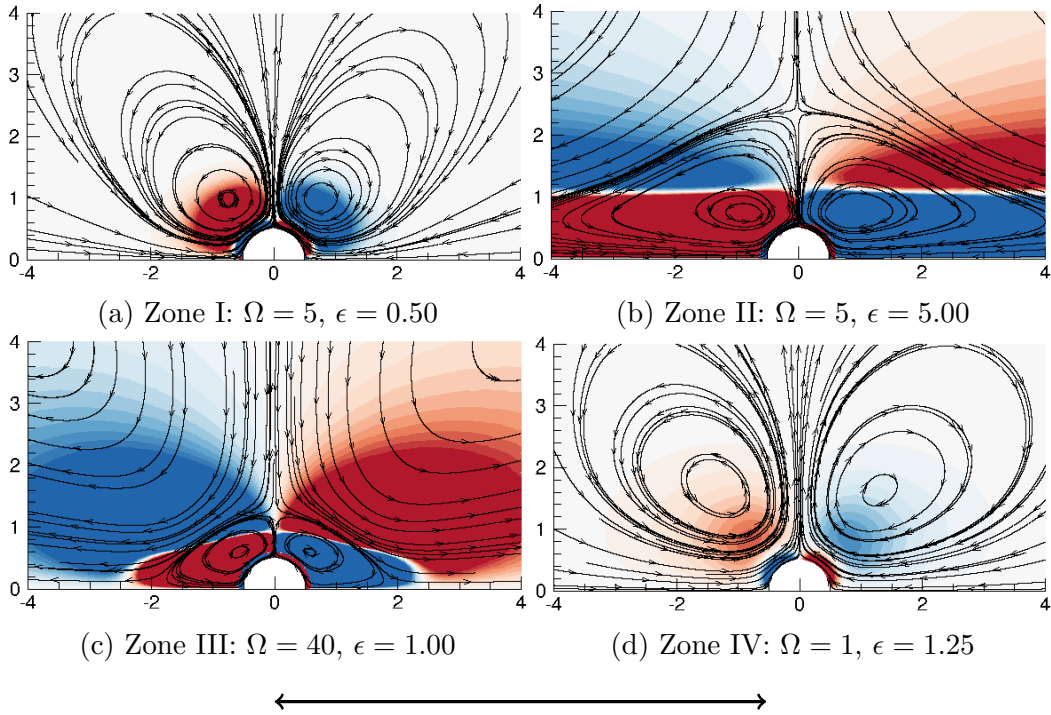


Figure 5.8: Steady streaming around a single sphere in four different zones when the imposed flow is oscillating in the direction of the bold black arrow. Colour represents azimuthal component of vorticity, between -0.01 (blue) to 0.01 (red), as described in section 4.1.1.

sive computationally. In comparison, the task of computing steady streaming flows around single sphere and around two spheres can be achieved quickly using WNF. It has the added flexibility of imposing oscillation at any given angle to the axis on which the spheres are placed.

It can be deduced from these steady streaming flows shown in Figure 5.1 that if another sphere is placed in the axial direction where the flow is away from the sphere, it will experience a repulsive force. Also, if another sphere is placed at a point in the lateral direction where the flow is coming towards the sphere, it will experience an attractive force. This raises the question whether steady streaming flows around two spheres could be pre-

dicted without actually performing a simulation of the two sphere problem. This point will be discussed again in section 6.3.2, to check if these predictions turned out to be true for steady streaming flows around two spheres. In this chapter, results were also reported for a moving sphere in a quiescent flow using WNF. As discussed in section 3.3.2, there is no change kinematically, i.e. there is no change to the velocity field.

After verification of WNF with DNS for a single sphere, steady streaming flows around two spheres using WNF, along with a new set of parameters defined, are given in the next chapter.

Chapter 6

Steady Streaming around Two Spheres

6.1 Introduction

A perturbation based method, WNF, was introduced in the previous chapter for steady streaming flows around a single sphere. In this chapter, WNF is used to calculate steady streaming flows and forces exerted on two spheres, solving the weakly non-linear form of the Navier-Stokes equations. A new problem is defined along with its parameters, described in the next section.

As mentioned in section 1.4, the work presented in this chapter is published in Fabre *et al.* (2017), based on the analysis done by David Fabre already given in section 3.3.2. In this chapter, the size of the spheres is half of those in Fabre *et al.* (2017), thus having an impact on the magnitude of the forces and visualizations involved. It does not change the overall conclusions however.

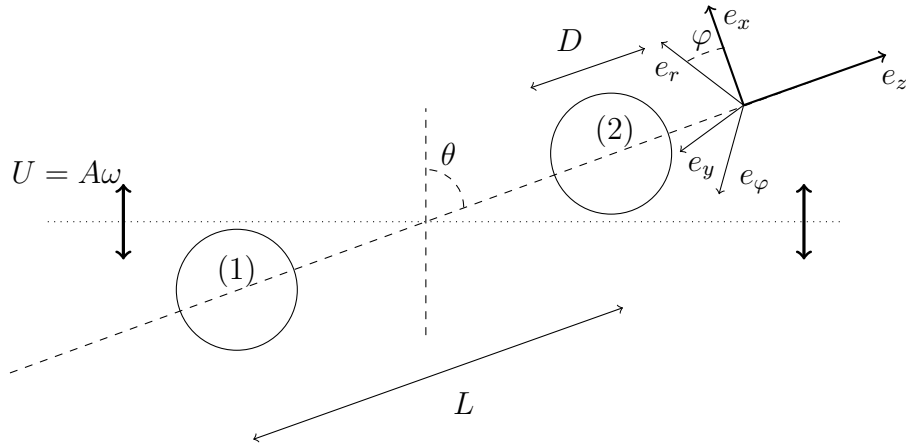


Figure 6.1: Schematic of the two sphere problem as shown in Figure 3.3.

6.2 Numerical Setup

As defined in section 3.3.2, two stationary, identical, non-rotating spheres of diameter D are set apart, at a distance L and positioned at an angle θ between the axis of oscillation and the axis which passes through their centers. As before, the flow can be expressed by the incompressible Navier-Stokes equations. Also as before, a no-slip boundary condition is assumed at the surface of spheres. When $\theta = 0^\circ$, the spheres are placed parallel to the axis of imposed oscillation, in an axial configuration (Figure 6.2(b)). Similarly at $\theta = 90^\circ$, the spheres are positioned perpendicular to the axis of imposed oscillation, in a lateral configuration (Figure 6.2(a)). The oblique configuration refers to when θ is some angle between these two limits; an example case at $\theta = 45^\circ$ is presented in Figure 6.2(c). In the frame that the figures are presented in, the oscillations are imposed in a vertical direction.

The dimensionless parameters involved are previously defined in section 3.2.2 as $\epsilon = A/D$, and Reynolds number, $\text{Re} = A\omega D/\nu$. In addition, a

ratio of Re and ϵ is introduced in section 3.2.2 as $\Omega = \omega D^2/4\nu$, also known as Stokes number.

The mesh comprises of triangles in a circular domain of size $100D$. A fine inner mesh with typical grid size of $0.015D$ was used, that gets coarser away from the embedded circles up to the full extent of the domain (see Figure 3.5). More details about the method itself and the mesh analysis are given in section 3.3.2.

6.3 Verification of Results for Two Equisized Spheres

For comparison of WNF results against those of a similar system in Klotsa *et al.* (2007), the interaction force, F_L , was measured as a function of the distance between the centers of two spheres, L/D , after non-dimensionalizing the parameters. Klotsa *et al.* (2007) performed experiments, and three-

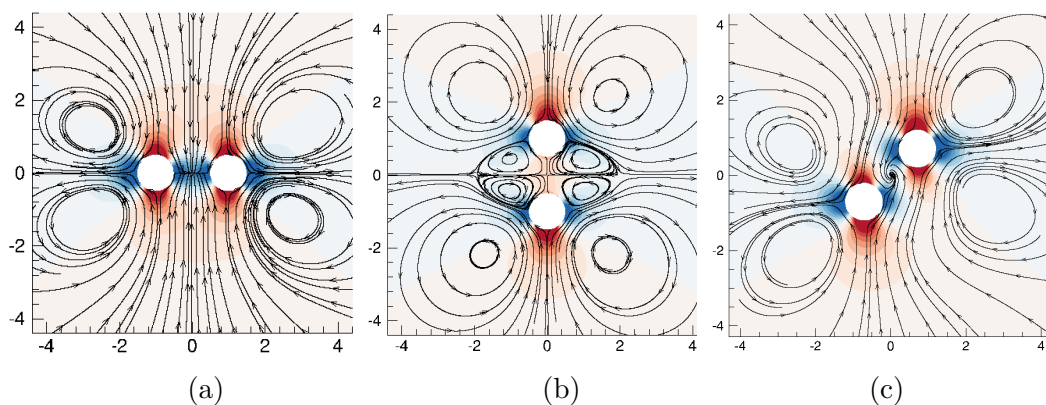


Figure 6.2: Pressure isolevels, between -0.01 (blue) to 0.01 (red), for $\Omega = 1$ in the (a) lateral, (b) axial, and (c) oblique configurations, when $L/D = 2$.

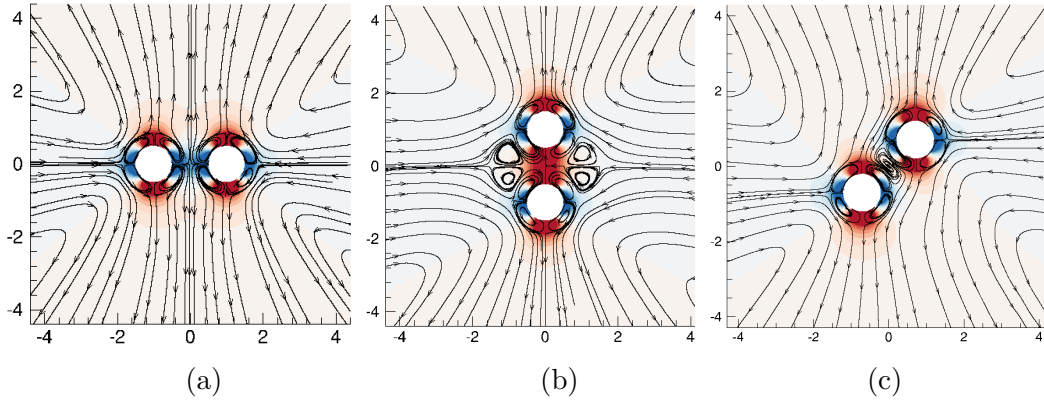


Figure 6.3: Pressure isovels, between -0.01 (blue) to 0.01 (red), for $\Omega = 100$ in the (a) lateral, (b) axial, and (c) oblique configurations, when $L/D = 2$.

dimensional simulations, of spheres immersed in a shallow fluid cell, where the depth of the fluid was not much more than the diameter of the spheres. These spheres were 1 mm in diameter and free to roll or slide along the bottom of the cell. The cell was then vibrated in the plane that the cells were free to move in and their motion analysed. Simulations performed by Klotsa *et al.* (2007) computed the force curve F_L for a pair of spheres, vibrated at 50 Hz with relative amplitude of the spheres' motion with respect to the cell, $A_r = 0.28$ mm, in a fluid of viscosity $4.5 \times 10^{-6} \text{m}^2 \text{s}^{-1}$. These values were used to achieve force curve in Figure 6.4, when the corresponding $\text{Re} \approx 20$, which is the equivalent of $\Omega = 17.85$. Figure 6.4 also shows the forces, F_L , measured for these parameters from the current WNF simulations, after normalizing L with radius R and F_L with C_F with an offset of $1.5D$. Here $C_F = \rho U^2 A_R$, $A_R = \pi R^2$, and (as previously defined) $U = A\omega$.

An interesting outcome of these force measurements is that there is a distance L/D at which the forces between the spheres is zero. This implies that there is an equilibrium position at which the spheres will not move.

This equilibrium distance, s , for F_L for the data used by Klotsa *et al.* (2007), is 0.6, as shown in Figure 6.4. However, s is a function of the frequency of oscillation. Klotsa estimated this functional dependence by fitting both experimental and numerical data to a function of the form $s = C\nu/(\omega D)$. The value of a numerical constant C was also measured. It was estimated that $C \simeq 6.5$ for experimental data and $\simeq 9$ for simulation data in Klotsa *et al.* (2007). After rescaling the parameters, and curve fitting using the relation $L/D \approx C/\Omega$, shown in Figure 6.5, a value of $C = 8.25$ was obtained.

The close match between the measured forces F_L and the value of C is remarkable given that the setup used by Klotsa *et al.* (2007) was only a

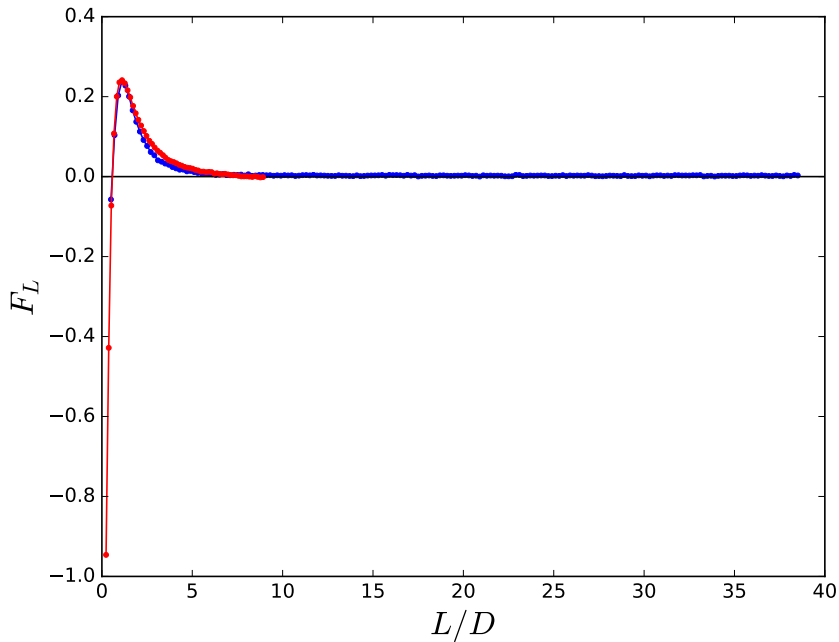


Figure 6.4: Time-averaged force, F_L , as a function of space between the spheres, L/D , after normalizing the parameters defined by Klotsa *et al.* (2007). Klotsa; —•, (WNF) $\Omega = 17.85$; —•. Positive and negative F_L represent attraction and repulsion between the spheres, respectively. The WNF curve is rescaled for a comparison.

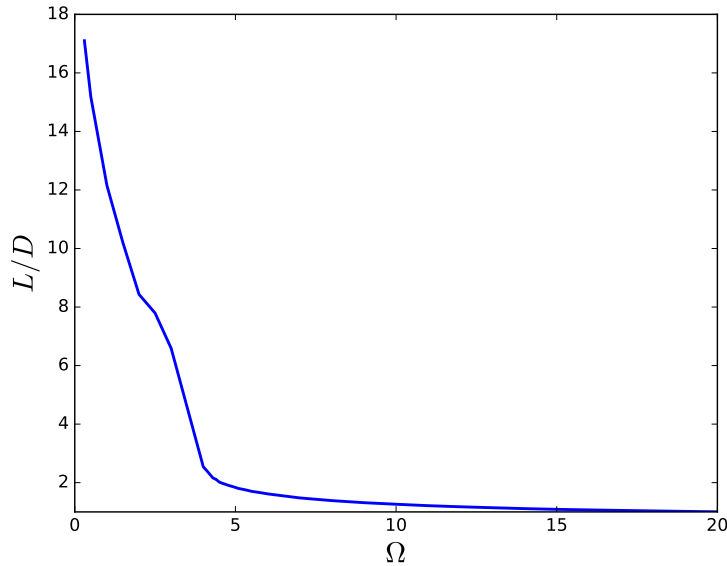


Figure 6.5: Equilibrium distance between the center of the spheres, L/D , as a function of frequency, Ω , in a lateral configuration, when spheres are positioned perpendicular to the axis of imposed oscillation. The total number of data points is 43.

small cell of domain extent = $3D$, including boundary effects on the spheres, whereas in the WNF simulations the spheres were assumed to be immersed in the fluid with extent of the domain = $100D$.

6.3.1 Streaming flows around two spheres

In this section, the effect of mean forces due to steady streaming is presented for different distances between the two spheres and for low to high Stokes number (or equivalently low to high sphere radii/frequency) Ω . Mesh dependence has been checked over various combinations of domain sizes and mesh densities, comprising, as noted earlier in section 3.3.2, a refined inner circular region close to the sphere(s), and a coarser outer one further away. The results vary only by $< 1\%$ across all the meshes (see Tables 3.7 and 3.8),

when measuring forces F_{TT} , F_{AA} , and F_{AT} for all values of Ω , as shown in Figure 6.9.

Steady streaming flows around two spheres in three different configurations are discussed and shown in the sections below, for $0.1 \leq \Omega \leq 100$. The colour in flow visualizations (Figures 6.6, 6.7, 6.8) represents the azimuthal component of vorticity (described previously in section 4) between -0.01 to 0.01 . Rings of vortices are formed with a plane of orientation perpendicular to the axis of oscillation. When sliced through in the plane of the simulation, these rings appear as a pair of equisized vortices, with opposite colors distinguishing between vorticity oriented in and out of the plane. The streamlines start from user selected points and consequently, might not be symmetrically placed.

It is worth recalling that high Ω corresponds either to high frequency, or to large particle size or both. For simplicity, in the descriptions that follow, the term ‘frequency’ will be used, but it should be understood that it refers interchangeably to particle size.

Lateral configuration

When the spheres are in a lateral configuration, the mean force in the axial direction, F_{TT} , is attractive for high frequencies and repulsive for low frequencies (see Figures 6.5, and 6.9 (a)). For intermediate values of Ω , there is a distance at which the mean force exerted on the spheres reduces to zero so the spheres stay at an equilibrium position. At distances less than this equilibrium position, the force is repulsive. At distances greater than the equilibrium position, the force is attractive. This setup also shows that the

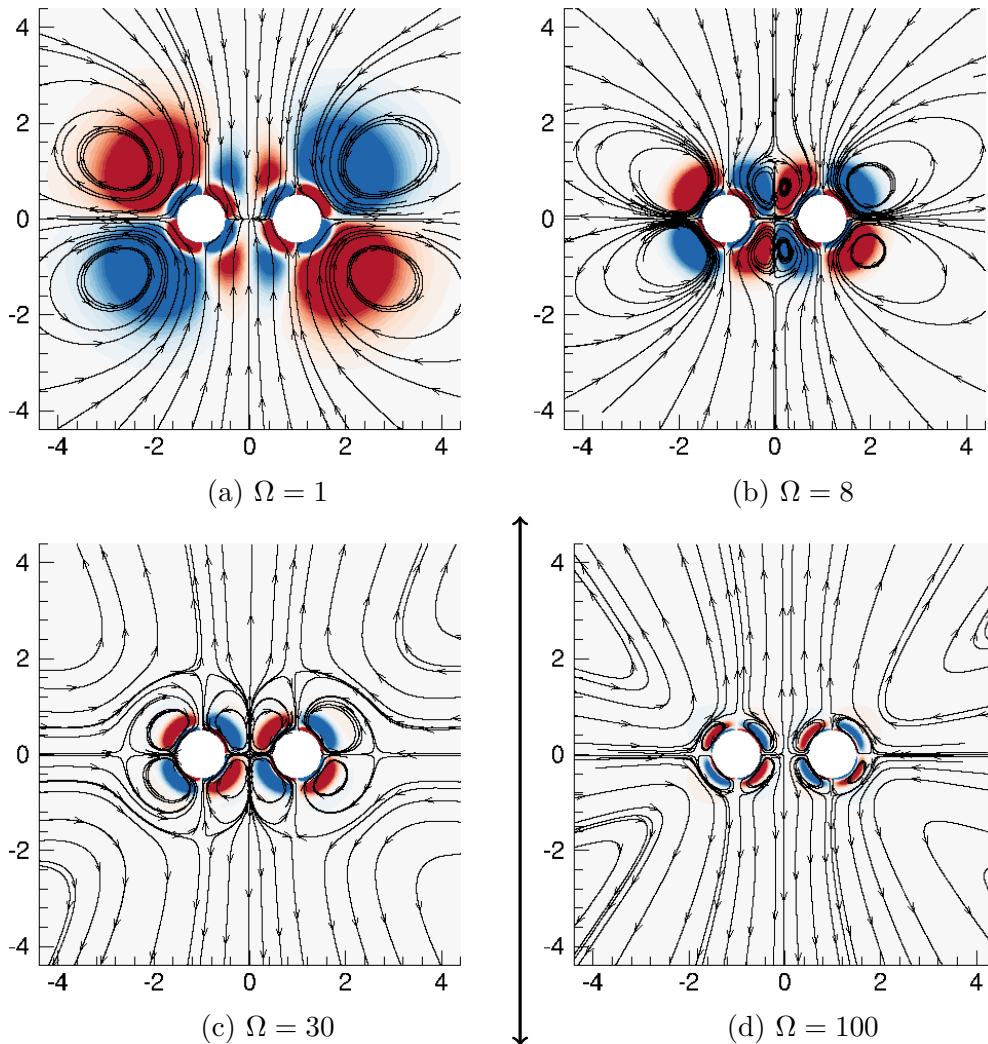


Figure 6.6: Steady streaming around two spheres in a lateral configuration, when $L/D=2$. The imposed flow is oscillating in the direction of the bold black arrow. Colour represents azimuthal component of vorticity -0.01 (blue) to 0.01 (red).

equilibrium is stable - excursions from the equilibrium position induce forces that push the spheres back towards the equilibrium.

The direction of the induced forces is clearly a function of the mean flow structures. In Figure 6.6, examples of these flow structures are shown for $L/D = 2$, for a series of increasing Ω . Note that there are only four

large inner vortices at $\Omega = 1$. These vortices reduce in size as the frequency increases. At around $\Omega = 8$, another pair of vortex rings appears for each sphere in between the spheres. The streamlines suggest that at such low frequencies the fluid is being pushed inwards in the direction of oscillation, (which is transverse to the axis joining the spheres), and therefore fluid is ejected outwards along the axis joining the spheres; thus the spheres repel each other. As the frequency further increases, the previous larger inner vortices adjust their size, together with the newly-formed small vortices, until they are of the same size. Meanwhile, the outer vortices are overpowering the inner vortices at $\Omega = 100$ meaning the direction of the flow in between the spheres is reversed with respect to the low Ω cases. The fluid is seen to be pushed inwards from the sides and rushing out in the direction of oscillation, and therefore fluid is pulled in along the axis joining the spheres, making the spheres come close together for higher Ω .

Axial configuration

In the axial configuration, the mean force in the axial direction shows an opposite trend to that of the transverse configuration (see Figure 6.9 (b)). It is attractive for low frequencies and repulsive for high frequencies. For intermediate values of Ω , the mean force between the spheres, F_{AA} , is attractive when the spheres are at a small distance apart, but is repulsive for large distances. This points out again the existence of an equilibrium distance. However, this equilibrium (in contrast to that for the transverse configuration) is unstable, as excursions from the equilibrium position induce forces that push the spheres further from this position. The direction of these forces

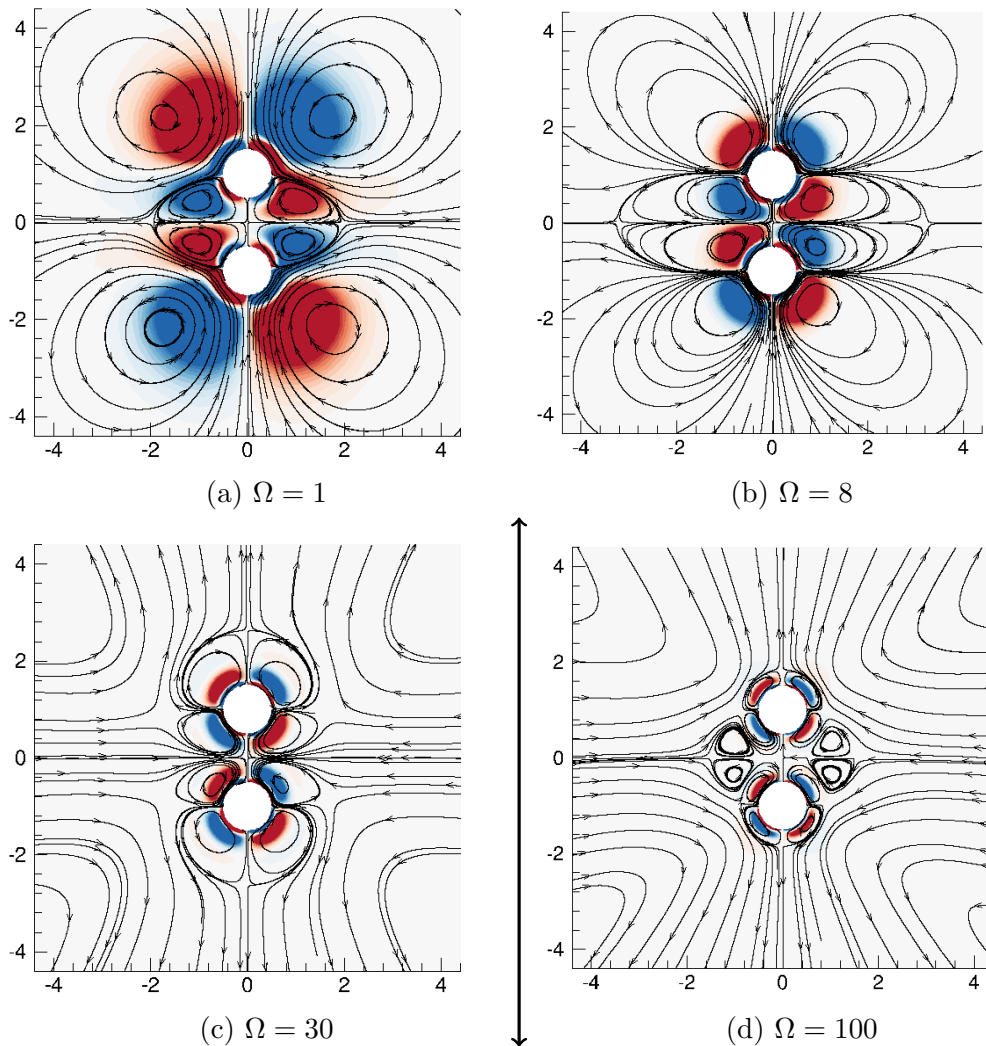


Figure 6.7: Steady streaming around two spheres in an axial configuration, when $L/D=2$. The imposed flow is oscillating in the direction of the bold black arrow. Colour represents azimuthal component of vorticity between -0.01 (blue) to 0.01 (red).

can be inferred from the pressure contours presented in Figures 6.2(b) and 6.3(b).

Figure 6.7 presents examples of the axial configuration for $L/D = 2$ for a series of increasing values of Ω . At $\Omega = 1$, the eight inner vortices (or four vortex rings) are very strong, comprising of four small ones that are in

between the spheres and four large ones around them. As the frequency increases, the size of these inner vortices starts to decrease. The outer vortices start to increase in size correspondingly. This continues until the inner vortices are confined close to the boundary of each sphere. The fluid is pushed inwards in the direction of oscillation suggesting an attraction between the spheres. The outer vortices keep growing, until at around $\Omega = 30$, there is a change in topology. Another set of vortices is quite noticeable around the two spheres. There are now twelve vortices (or six vortex rings) close to spheres in addition to four outer ones (two vortex rings) at $\Omega = 100$. The streamlines flowing in from the sides, inducing a flow outwards along the axis joining the spheres, suggest that the spheres will repel.

Oblique configuration

The oblique configuration refers to spheres positioned at an angle between $0^\circ < \theta < 90^\circ$. As an example, $\theta = 45^\circ$ is considered and shown in Figure 6.8. There is a similar trend for the case of spheres in an oblique configuration to that of the lateral configuration. Four large inner vortices are accompanied by another one in between the spheres at lower frequencies.

As the frequency is increased, another pair of vortices starts to appear perpendicular to the axis of oscillation at around $\Omega = 8$. The shared central vortex splits into two at $\Omega = 30$. These two new vortices get noticeable as Ω increases and become the inner vortices present in between the spheres. All these vortices keep shrinking until they are all confined close to the boundary of the spheres by the larger outer vortices at $\Omega = 100$, in addition to another shared vortex between the spheres. The mean forces,

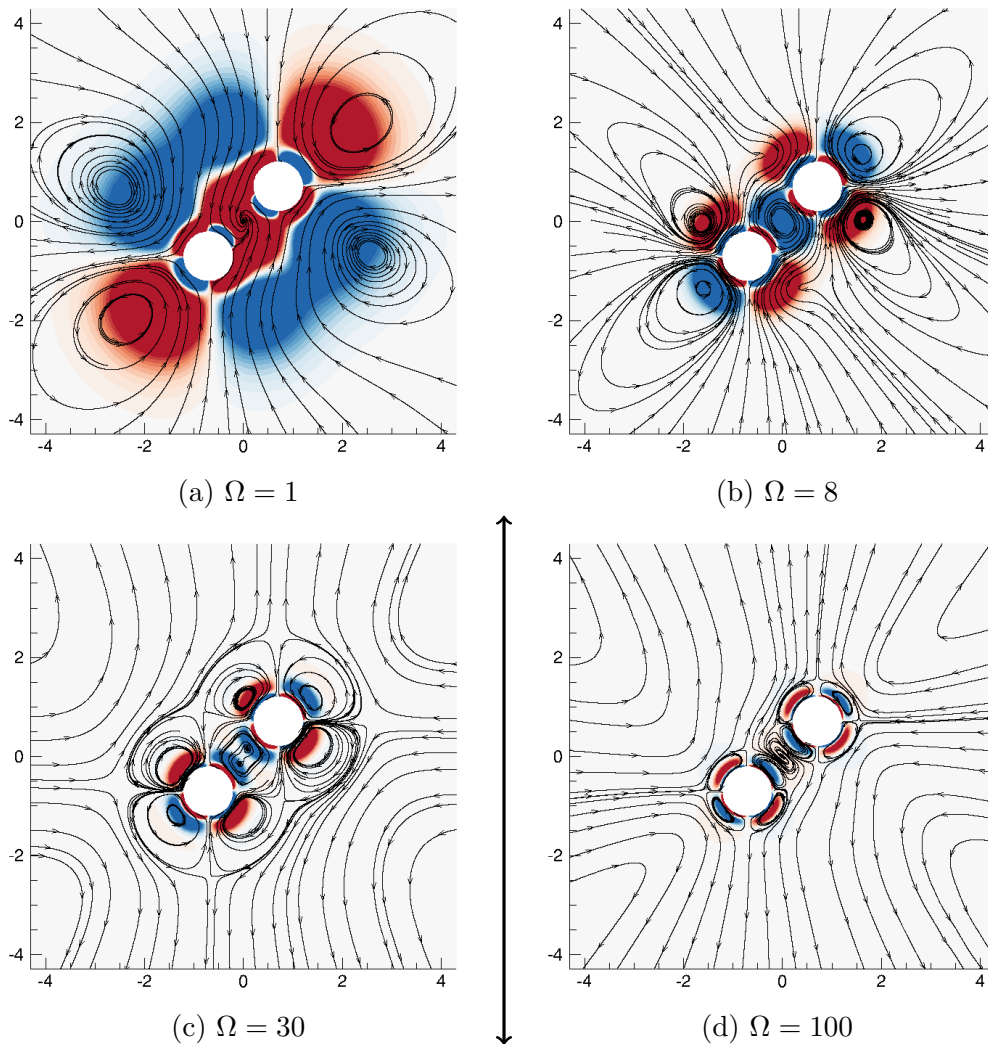


Figure 6.8: Steady streaming around two spheres in an oblique configuration, when $L/D=2$. The imposed flow is oscillating in the direction of the bold black arrow. Colour represents azimuthal component of vorticity between -0.01 (blue) to 0.01 (red).

F_{AT} , are non-symmetric, also this is evident from the streamlines. This lack of symmetry induces a transverse force, which in turn induces a moment on the spheres about their central point, that will push the spheres to re-align themselves in a lateral configuration. This point is discussed in the next

section.

Stable equilibrium between the spheres

In the lateral configuration, the forces exerted on the spheres are zero at a point of stable equilibrium for intermediate frequencies. The force between the spheres is repulsive at small distances and attractive at large distances, hence the stability. In an axial configuration, the force is repulsive at large distances but attractive at small distances for intermediate frequencies. Therefore, there is also an equilibrium position, though an unstable one. In the oblique configuration, a transverse force is generated via the coupling between the axial and lateral motion. Since the force is transverse, equal, and opposite on each of the spheres, the spheres rotate about their shared center and tend to realign themselves into the lateral configuration. Out of the three configurations discussed, the lateral configuration is the only one where the spheres find a stable equilibrium position. For the lateral configuration, the equilibrium distance is presented in Figure 6.5 for all Ω . For $\Omega \geq 20$, the forces are attractive for all distances, and if the spheres were free to move, they would eventually touch each other at $L/D = 1$.

The Stokes number Ω is described as frequency here. However, as noted earlier, if frequency ω and viscosity of the fluid ν are kept constant, Ω can also be seen as a parameter representing the size of the spheres. This means lower Ω represents small spheres, and larger Ω , large sized spheres. The only stable configuration is the lateral one, so this discussion is kept only to particles in a lateral configuration. The larger spheres ($\Omega \geq 10$) are attractive towards each other and smaller ones ($\Omega < 5$) will be repulsive. This

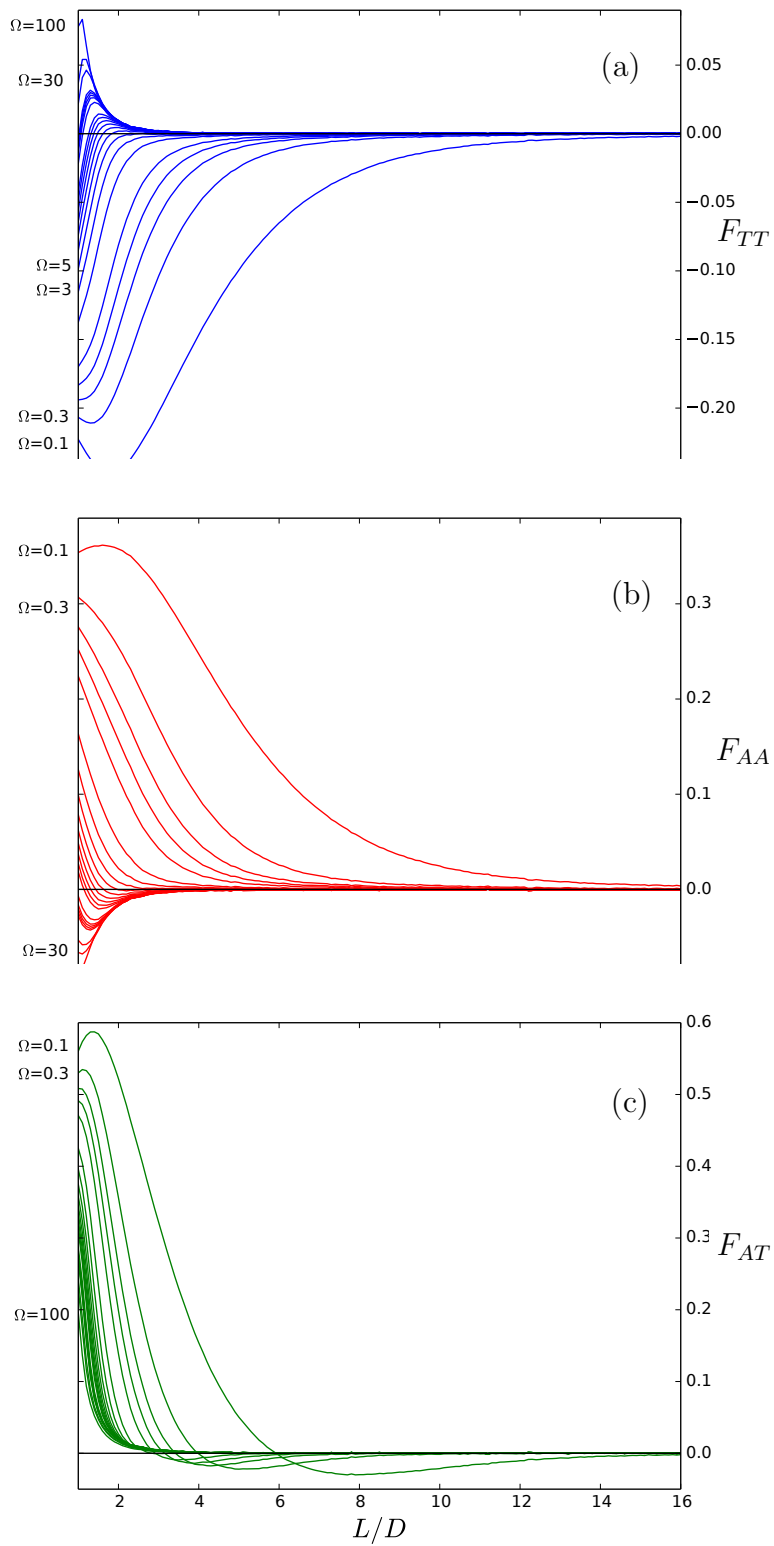


Figure 6.9: Forces, F_{TT} , F_{AA} , and F_{AT} , exerted on spheres by steady streaming in the (a) lateral configuration, (b) axial configuration, and (c) oblique configuration, respectively, as a function of distance L/D in between them for different values of Ω . The equilibrium distance occurs whenever a force curve crosses 0.0.

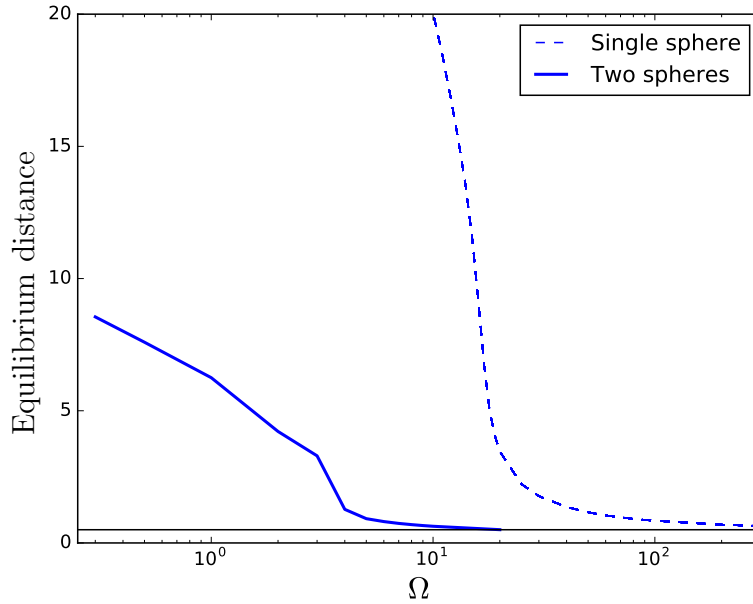


Figure 6.10: Distance where net force experienced by the sphere(s) is zero i.e. the equilibrium distance as a function of Ω , in a lateral configuration. The black horizontal line shows where the two spheres touch, at $L/D = 1$. The solid line, —, shows the location of the stable equilibrium for the intermediate values of Ω . If the two-sphere flow could be found by simply superimposing the flows around two individual spheres, this curve would coincide with the dashed line, --, the distance to the stagnation point in the single sphere case.

implies that in any situation with a non-uniform distribution of particles, larger particles will be attracted to each other and eventually touch, whereas small particles will repel. Such a non-uniform size distribution is the case for milk fat globules, hence they will still be present in the fluid (milk). This brings us to the same possibility discussed in section 5.2.1, for trends of DNS data when $\Omega \leq 25$ and $\epsilon \leq 0.75$ in Figure 5.3, that Milk Fat Globules (MFGs) of sizes around $4 - 5 \mu\text{m}$ and less, will not get removed in the cream separation process from milk.

6.3.2 Discussion

Although streaming flow around two spheres could be predicted from flow visualizations of a single sphere, as also pointed out in section 5.4, the flow around two spheres is not a simple superposition of two single spheres placed at a distance where net force experienced is zero. This statement is verified by a comparison of r_{cross}/D computed for flow around a single sphere, and equilibrium distance L/D , for flows around two spheres, shown in Figure 6.10.

For steady streaming flow around a single sphere, the flow is zero at a stagnation point. The distance from the center of the sphere to this point is measured as r_{cross} . If the flow for two spheres were a simple superposition, placing a second sphere centered at this distance should result in there being zero force between the spheres. To show that just a simple addition of another sphere's flow is not enough to predict flows around two spheres, the equilibrium distance for two spheres (where the net force on the spheres is zero), L/D , was plotted. For a single sphere, r_{cross} was picked from WNF data for y -axis from Figure 5.3. It was scaled for a comparison with the curve for equilibrium distance L/D in Figure 6.5 for two spheres in a lateral configuration, shown together in Figure 6.10. At $\Omega = 10$, there is an order of magnitude difference between distance to the stagnation points (or the equilibrium distance) for a single sphere and two spheres.

Also, the predictions from flows around a single sphere suggest that another sphere placed at the stagnation point will continue to experience either an attractive or a repulsive force irrespective of how they move in

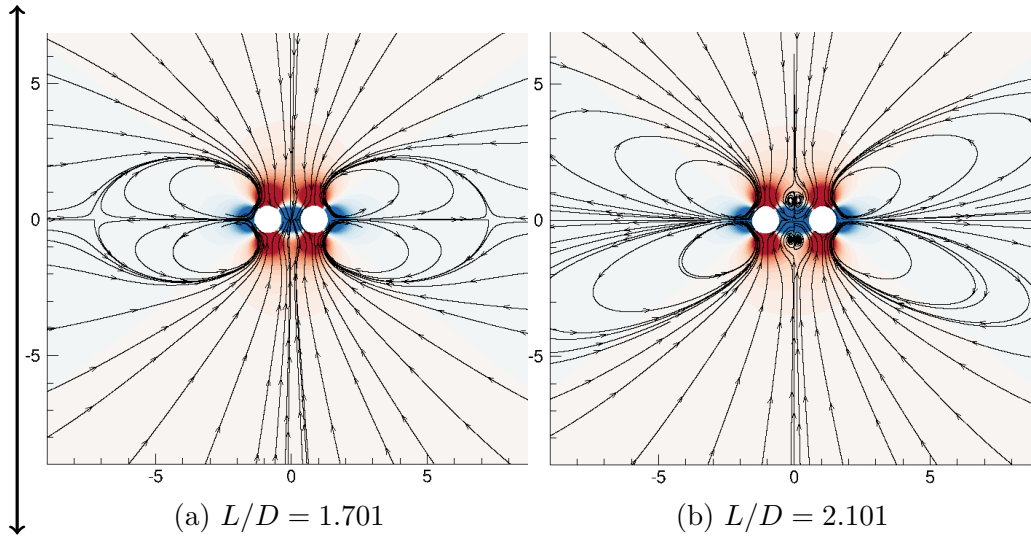


Figure 6.11: Attraction between two spheres changing to a repulsion for $\Omega = 5$ in a lateral configuration. Colour represents pressure -0.05 to 0.05 . The imposed flow is oscillating in the direction of the bold black arrow.

response to the force. Looking at forces F_{TT} for $\Omega = 5$, a point of equilibrium occurred at about $L/D = 1.9$ in Figure 6.9(a), where the repulsive force switched to being an attractive force. The flow changed its behaviour from being pushed inwards to outwards. This is also evident from flow visualizations at around that point, in Figure 6.11. Hence, it was necessary to carry out simulations around two spheres to take all these variations of fluid behaviour into account.

6.4 Summary

A new computational method based on a perturbation method, WNF, has been applied, after being verified, for the study of interactive forces and streaming flows around two spheres. It is much quicker and less expensive than the DNS, especially for the case when flows around two spheres are

considered. The need to perform simulations for two spheres in the first place has also been considered and confined. In addition, forces can be calculated and flows visualized for $0.1 \leq \Omega \leq 100$ and $0^\circ \leq \theta \leq 90^\circ$ which is a much larger range of parameters than studied previously in the literature. Regimes where two equal sized spheres attract or repel each other in three different configurations for different frequencies have been discussed.

It was concluded that for high frequencies the spheres tend to re-align themselves in to the lateral configuration before attracting each other. This also means that particles of larger sizes ($\Omega \geq 20$) will attract each other and, in the milk-separation application, MFGs rise to form cream, whereas the smaller ones ($\Omega < 5$) will still remain suspended in milk. These results verify the conclusions of experiments conducted by Leong *et al.* (2016).

Chapter 7

Trajectories of Oscillating Spheres

7.1 Introduction

In the previous chapter, it was concluded that there are streaming forces present between two identical spheres that make them attract or repel. In particular, it is the spheres in an oscillatory flow with high frequencies ($\Omega \geq 10$) in the lateral configuration that are attractive. For the separation of cream from milk, the Milk Fat Globules (MFGs) need to be close enough so that interactive streaming forces can come into play (Manasseh *et al.*, 2016). It would be useful to understand the process of how these streaming forces cause the spheres to move. Moreover, similar issues are expected to occur in other ultrasonic separation applications e.g. Leong *et al.* (2015).

The objectives of work in this chapter are to find:

- initial conditions that lead a pair of spheres to eventually touch.

- the time it takes for spheres to touch each other.
- a parameter space of the motion characteristics for the cases where a stable equilibrium is achieved.

7.2 Method Employed for Calculating Trajectories of Oscillating Spherical Particles

In this section, a numerical model is set up to trace paths traversed by two identical spheres, using forces exerted on spheres by the steady streaming flows measured with WNF in section 6.3.1. It is assumed that the timescale of any motion induced by the streaming forces is much longer than the timescale of the oscillatory flow. (This assumption is reviewed in section 7.3.) The forces on two particles at any particular time are governed purely by the instantaneous spacing; the forces on particles in a particular position are the same as forces for a simulation when particles are assumed fixed in that position.

Also, the streaming speeds, i.e. the speeds in the mean flow field u , were assumed to be faster than the speed of the particles, $U_{Particle}$. This assumption was necessary so that the spheres could be treated as quasi-steady. This means the forces are dictated only by the relative position of the two spheres, and not their relative velocity.

7.2.1 Algorithm for integration of forces

The equation of motion of a sphere considering a long-time scale, is given by Newton's second law of motion

$$\mathbf{F} = m\mathbf{a} \Rightarrow \mathbf{a} = \mathbf{F}/m, \quad (7.1)$$

where \mathbf{F} is given by equation (3.18). The drag and bouyancy forces are negligible and thus not considered. Equation (7.1) was numerically integrated twice to get position using the Adams-Bashforth explicit method of second order i.e.

$$\mathbf{v}_{\mathbf{n}+1} = \mathbf{v}_{\mathbf{n}} + \Delta t \left\{ \frac{3}{2} \mathbf{a} \Big|_n - \frac{1}{2} \mathbf{a} \Big|_{n-1} \right\}, \quad (7.2)$$

where \mathbf{v} is the velocity of the sphere. Since $\mathbf{v} = \frac{\partial \mathbf{y}}{\partial t}$,

$$\Rightarrow \mathbf{y}_{\mathbf{n}+1} = \mathbf{y}_{\mathbf{n}} + \Delta t \left\{ \frac{3}{2} \mathbf{v} \Big|_n - \frac{1}{2} \mathbf{v} \Big|_{n-1} \right\}, \quad (7.3)$$

where \mathbf{y} is the position of the sphere. The integral for \mathbf{y} needs force, \mathbf{F} , so at each time step:

1. Distance between centers of the spheres, L , and the angle between the oscillatory flow and the center of their axis, θ , is measured.
2. This distance, L , and angle, θ , is used to look up the force, \mathbf{F} , from a table of numerical data computed using WNF, and this force was divided by the particle mass, m , to obtain an acceleration. This mass, m , is explained in the following section 7.2.2.
3. Integration of these accelerations was carried out for new velocity, \mathbf{v} ,

and position, \mathbf{y} , of the sphere.

4. Repeat 1 to 3 until one of the stopping criteria was hit.

The algorithm stops, if:

- Distance $L/D = 1$ i.e. the spheres touch.
- The calculated distance between the spheres exceeds the maximum value for which data are available for i.e. $L/D = 20$.
- The above two criteria were not met and the number of time steps exceeds a predetermined set limit of 15000 timesteps.

The algorithm stated above was used as a subroutine to calculate trajectories of the spherical particles, explained in the following section.

7.2.2 Tracing trajectories of spherical particles using streaming forces

Using WNF, the streaming forces experienced by each sphere that will either bring two such spheres together, or force them apart, are computed. Since the spheres are identical, the forces computed on either sphere are equal but opposite in direction. The interactive forces are computed on sphere (2) and translated to sphere (1), as labelled in Figure 3.3. Note that under a non-dimensional scheme given in Appendix, equation (4), a dimensionless mass $m = 0.5$ was considered in equation (7.1), for the numerical model, corresponding to a density ratio relative to the surrounding fluid, $\rho^* \approx 0.9$ which is appropriate for MFGs. Note that $m = \frac{m^*}{\rho^*}$.

Considering oscillation in the x -direction, the positions of spheres are calculated in the xz -plane. The angle between the spheres and the axis of oscillation, measured clockwise, is θ . The initial position is computed as $L_0/2 \sin \theta_0$ in the x -direction and $L_0/2 \cos \theta_0$ in the z -direction, where θ_0 and L_0 (center to center distance between two spheres) are the inputs, and θ is measured and interpolated around 360° . For a given value of Ω , the result is sensitive to the initial conditions when L_0 is close to the equilibrium distance for that Ω .

For integration of velocity, \mathbf{v} , and position, \mathbf{y} , using forces, \mathbf{F} , the two-step Adams-Bashforth scheme was employed with the Euler method used for starter values, as explained in section 7.2.1. As noted in section 3.3.2), the formula to compute forces using WNF, at any given angle, is given by

$$\overline{\mathbf{F}^{(1)}} = -\overline{\mathbf{F}^{(2)}} = \rho D^2 U^2 \{(\cos^2 \theta F_{AA} + \sin^2 \theta F_{TT}) \mathbf{e}_z + \cos \theta \sin \theta F_{AT} \mathbf{e}_x\}. \quad (7.4)$$

The forces integrated to obtain trajectories of particles, following the algorithm in section 7.2.1, were computed using equation (3.18). The resulting trajectories of spheres are discussed in the section 7.4.

7.3 Validity of the Numerical Model Employed for Calculating Trajectories

When calculating the trajectories of the particles, as noted in section 7.2, the assumption that the flow is quasi-steady is valid as long as the speed of the particles, $U_{Particle}$, is significantly slower than typical values of streaming

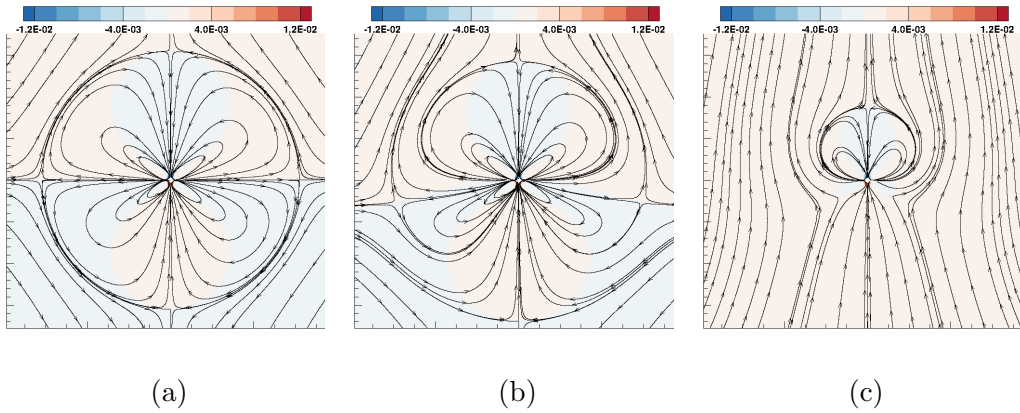


Figure 7.1: Trajectories when a small velocity in the axial direction is added, for $\Omega = 4$. (a) Undisturbed case, where $U_{Stream} \simeq \mathcal{O}(10^{-3})$, (b) velocity of 10^{-6} added, and (c) velocity of 10^{-5} added.

velocity, u . For convenience, the maximum of the streaming velocity is defined as U_{Stream} . In order to estimate how slow $U_{Particle}$ should be compared to U_{Stream} , a small constant was added to U_{Stream} for a test case of $\Omega = 4$, for which $L/D = 2.5$. As demonstrated in Figure 7.1, the recirculating flow pattern is obliterated when a constant of $\mathcal{O}(10^{-5})$ is added to U_{Stream} i.e. $\mathcal{O}(U_{Particle})$ is two orders of magnitude smaller than $\mathcal{O}(U_{Stream})$.

The magnitude of U_{Stream} and $U_{Particle}$ is compared in Figure 7.2 where the assumption that the flow is quasi-steady is valid for time $t = 0.015$ i.e. $\mathcal{O}(U_{Particle}) < \mathcal{O}(U_{Stream})$. Here, dimensionless time $t = \text{number of time steps} \times dt$ with $dt = 10^{-4}$. Recall from equation (3.6) that the time scale for time t is $1/\omega$. The results obtained using the numerical model presented in section 7.2, thus, are valid only when run for very short times t and/or for L_0 that matches equilibrium distances L/D for particular Ω . These results are given in the next section, i.e. section 7.4, for a much longer range of t with number of time steps 10^4 times that used for Figure 7.2.

For the results obtained in section 7.4 to be valid, it is assumed that the flow fields calculated for motionless particles and the resulting forces are unaffected by $U_{Particle}$. The calculation of trajectories that is valid over a wider range of parameters, Ω and t , would require a completely different ‘fully coupled’ problem to be solved, in which the particles move with a speed, $U_{Particle}$, that is significant with respect to the streaming velocity magnitudes, U_{Stream} . This would significantly distort the streaming flow fields, and presumably, change the forces causing attraction or repulsion of the particles significantly, in turn altering $U_{Particle}$. This fully coupled calcu-

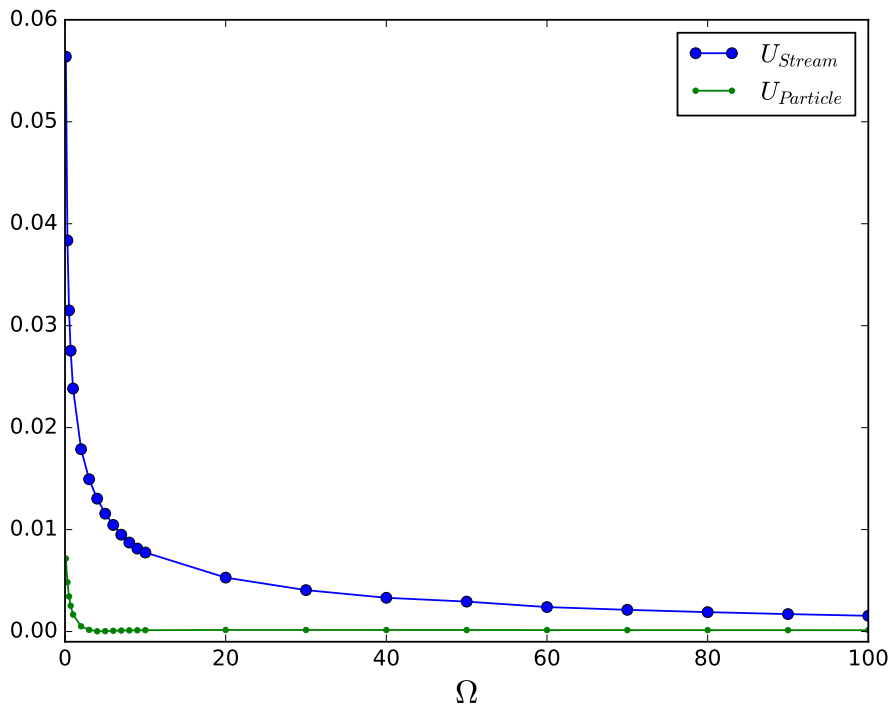


Figure 7.2: Comparison of the streaming and particle velocities, U_{Stream} and $U_{Particle}$, respectively, when $L_0 = 2.3D$, and $\theta_0 = \pi/2$ rad. $U_{Particle}$ is measured for a time $t = 0.015$.

lation where the particles are coupled with the fluid and are allowed to move as the fluid oscillates under the influence of the body force is beyond the scope of this thesis, but an illustration of the richness of the behaviour that might be expected can be found in results presented in section 7.4. In these results, although the constraint of validity, that $U_{Particle}$ is significantly less than U_{Stream} , is relaxed, it still demonstrates the behaviour of particles. The timescale involved here is longer than that of the imposed oscillatory flow which is happening at a much faster rate. The work in section 7.4 provides a guide for future work where fully-coupled calculations are undertaken.

7.4 Trajectories of Two Equisized Oscillating Spheres

As found in section 6.3.1, the lateral configuration is the only configuration where the spheres find a stable equilibrium position, out of the three configurations discussed. Trajectories of spheres positioned in a lateral configuration are traced and shown in Figure 7.3(a) using the model explained in section 7.2, and the assumption that was discussed in section 7.3. The initial spacing used was $L_0 = 1.836$. It can be observed that for small frequencies, $\Omega < 5$, the spheres repelled, and touched each other for high frequencies $\Omega \geq 20$. For intermediate frequencies, $5 \leq \Omega \leq 10$, the spheres tend to oscillate around an equilibrium distance close to each other. This behaviour of spheres positioned in a lateral configuration has also been predicted in section 6.3.1. For most parameters, small variations in the initial conditions did not cause large

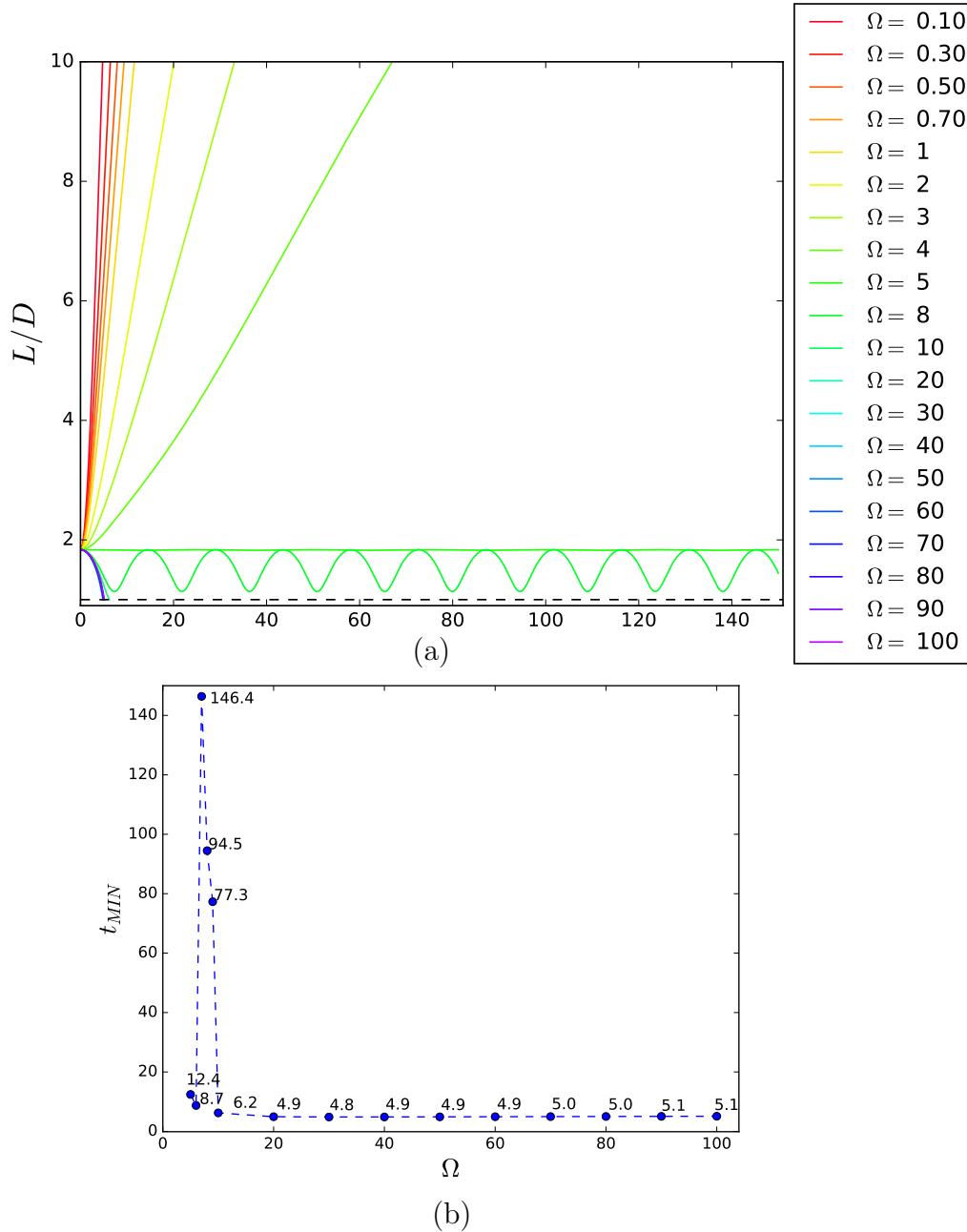


Figure 7.3: (a) Trajectories of spheres over dimensionless time, t , for frequencies $0.10 \leq \Omega \leq 100$, when $L_0 = 1.836$ and $\theta_0 = \pi/2$ rad i.e. lateral configuration. The black horizontal dashed line shows $L/D = 1$. (b) Time, t_{MIN} , taken to reach the absolute minimum L_{MIN} for $L_0 = 1.836$ and $\theta_0 = \pi/2$ rad.

variations, except for cases when L_0 is close to the equilibrium distance for particular Ω . In Figure 7.3(a), $L_0 = 1.836$ corresponded to the equilibrium distance for $\Omega \approx 5$, predicted according to Figure 6.5, hence the oscillatory behaviour for $5 \leq \Omega \leq 9$.

Since the trajectories of these spheres could be traced, the time it took for spheres to travel along those trajectories could also be quantified. In Figure 7.3(b), the time it took for spheres to get to its absolute minimum, or touch at $L/D = 1$, is given as t_{MIN} . Overall t_{MIN} decreases as Ω increases. The spheres simply repelled for $\Omega < 5$ and never touched. For intermediate frequencies $5 \leq \Omega \leq 9$, the spheres took a longer time to get to their respective minimum value of L_{MIN} close to 1. The spheres touched each other for $\Omega \geq 10$ in around $4 - 7t_{MIN}$, where t_{MIN} is the time taken to reach the absolute minimum L_{MIN} for the given initial conditions. The validity of these results was already discussed in section 7.3.

7.4.1 Estimating particle behaviour around conditions leading to equilibrium

The role of initial conditions, L_0 and θ_0 , is investigated for the intermediate frequencies $5 \leq \Omega \leq 9$, where a small change can shift particle behaviour significantly. Also, this is the range of Ω relevant to the size of MFGs (1 – 12 microns), being exposed to ultrasound of 1 – 2 MHz frequencies.

The case $\Omega = 5$ is chosen, owing to information drawn from the plot for forces for lateral configuration in Figure 6.9. A contour plot is drawn for a range of initial conditions for $\Omega = 5$ in Figure 7.4, for $1.2 \leq \theta_0 \leq \pi/2$ rad

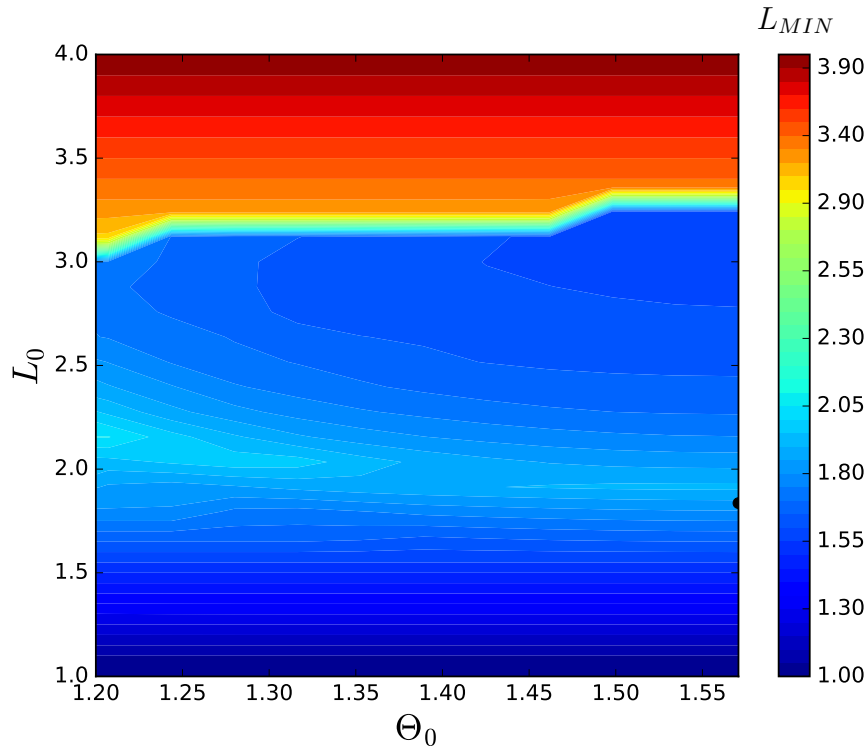


Figure 7.4: Contour plot for L_{MIN} showing convergence and divergence trends for $\Omega = 5$, for a range of L_0 and θ_0 close to the point of equilibrium $L_0 = 1.836$ and $\theta_0 = \pi/2$ rad, represented by black circle.

and $1 \leq L_0 \leq 4$ showing the minimum distance between the spheres achieved at any point in time, L_{MIN} . For this range of initial conditions close to the point of equilibrium $L_0 = 1.836$ and $\theta_0 = \pi/2$ rad, Figure 7.4 shows that the spheres tend to oscillate around an equilibrium. The spheres never actually touch, according to the contour plot, with the minimum distance L_{MIN} never passing below 1. The amplitude of oscillation increases around L_0 when the spheres start off far from each other. However, this oscillation is about a point L_0 much further than $L/D = 1$, so the large amplitude of oscillations do not cause the spheres to touch.

To investigate this behaviour further, data was picked along the

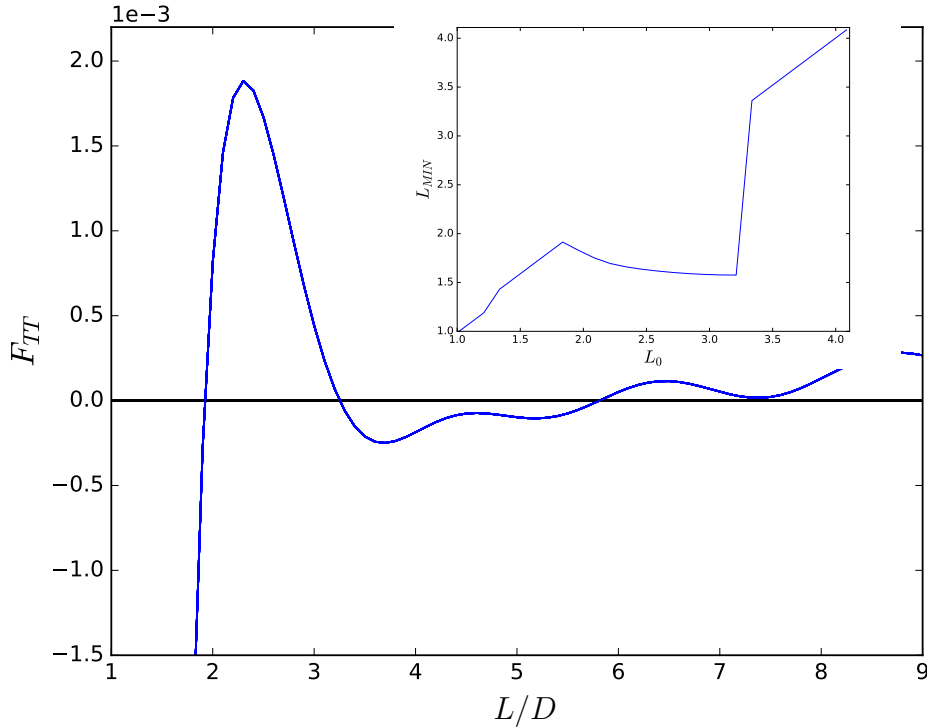


Figure 7.5: Force, F_{TT} , for $\Omega = 5$. The first equilibrium is at $L/D = 1.926$ and, the second, at $L/D = 3.2$ for the smoothed force (reducing noise). (Inset) Data extracted out of Figure 7.4, along $\theta_0 = \pi/2$ rad.

vertical line $\theta_0 = \pi/2$ rad, and plotted for L_{MIN} in the inset of Figure 7.5. The curve L_{MIN} was expected to converge to $L/D = 1$, but instead it heads up higher, apparently, to another equilibrium, as L_0 is away from the point of equilibrium. There appear to be multiple points of equilibria, as seen in Figure 7.5, that could also be noticed in the contour plot Figure 7.4 as well. The spheres seem to overshoot when starting farther off from equilibrium distance L_0 , towards the second equilibrium, which is further away.

In Figure 7.6, a contour plot is shown for $\Omega = 10$ starting off at equilibrium distance $L_0 = 0.630$. For $\Omega = 10$, the equilibrium distance is

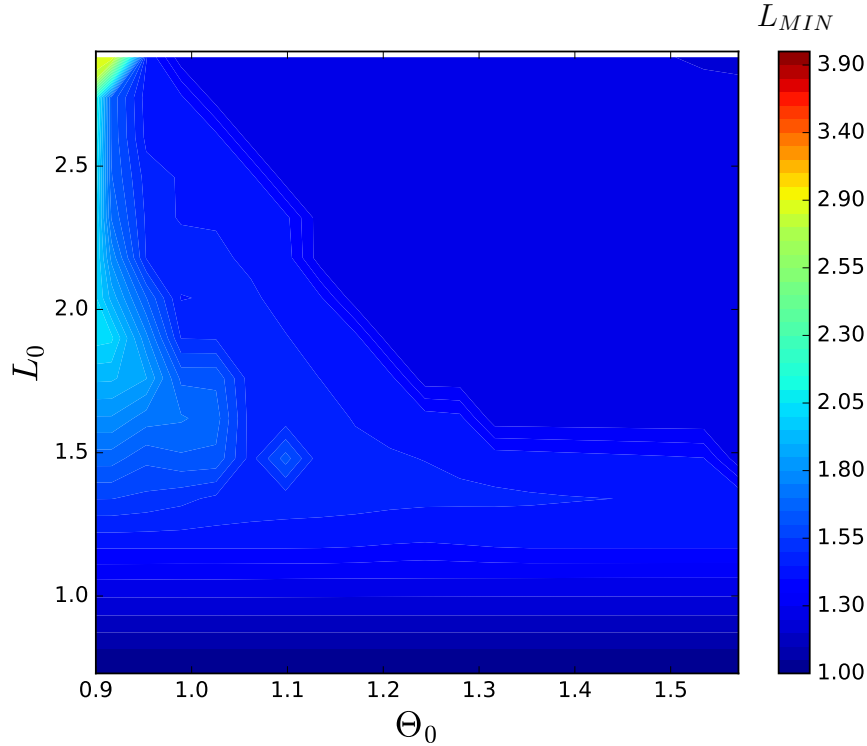


Figure 7.6: Contour plot for L_{MIN} trends for $\Omega = 10$, for a range of L_0 and θ_0 showing mostly convergent trend close to the corresponding point of equilibrium $L_0 = 0.630$ and $\theta_0 = \pi/2$ rad.

quite small so spheres are very close to touching each other. For a variation in the initial conditions L_0 and θ_0 close to the equilibrium distance, the spheres still touch each other in most part of the domain checked i.e. $1 \leq L_0 \leq 2.8$ and $0.9 \leq \theta_0 \leq \pi/2$ rad.

It should be recalled that most of these results are in the regime where $U_{Particle}$ is not very small compared to U_{Stream} , and thus the present results cannot be considered valid. Nonetheless, when a fully coupled calculation is able to be made, complex behaviour such as multiple equilibria may well be found.

7.4.2 Trajectories of particles in milk separation

In whole milk, there is 4% milk fat present approximately. If α , the concentration of milk fat in the milk, is the ratio of volume of the spherical MFG of radius R to the volume of the cube containing it with length l , then

$$\frac{4}{3}\pi\left(\frac{R}{l}\right)^3 = \alpha = 0.04 \Rightarrow \frac{R}{l} \approx 0.21. \quad (7.5)$$

Thus, the initial distance between centers of the milk fat particles is $l/R = 1/0.21 = 4.7$, or $2.3D$, where D is the particle diameter. Therefore, the MFGs are certainly close enough to be susceptible to mutual forces from mean streaming. Upon application of ultrasound, the streaming effects will be strong enough for particle interaction.

The preceding analysis predicts that the streaming forces on the MFGs that are large enough to have an $\Omega \geq 10$ will eventually cause them to touch, as they are rotated into a lateral configuration and then mutually attract. However, for smaller particles with lower Ω , it is predicted that the particles will repel, or possibly oscillate around an equilibrium position. These interim findings would need to be revised once a fully coupled calculation is undertaken.

It should be noted however, that there may be other processes which cause the particles to touch when then are brought close together by the streaming. As the particles are drifting closer to each other, they are also vibrating to and fro and very small particles will be susceptible to Brownian motion. Thus, real particles could over shoot from the point of equilibrium predicted by the model, and could actually touch.

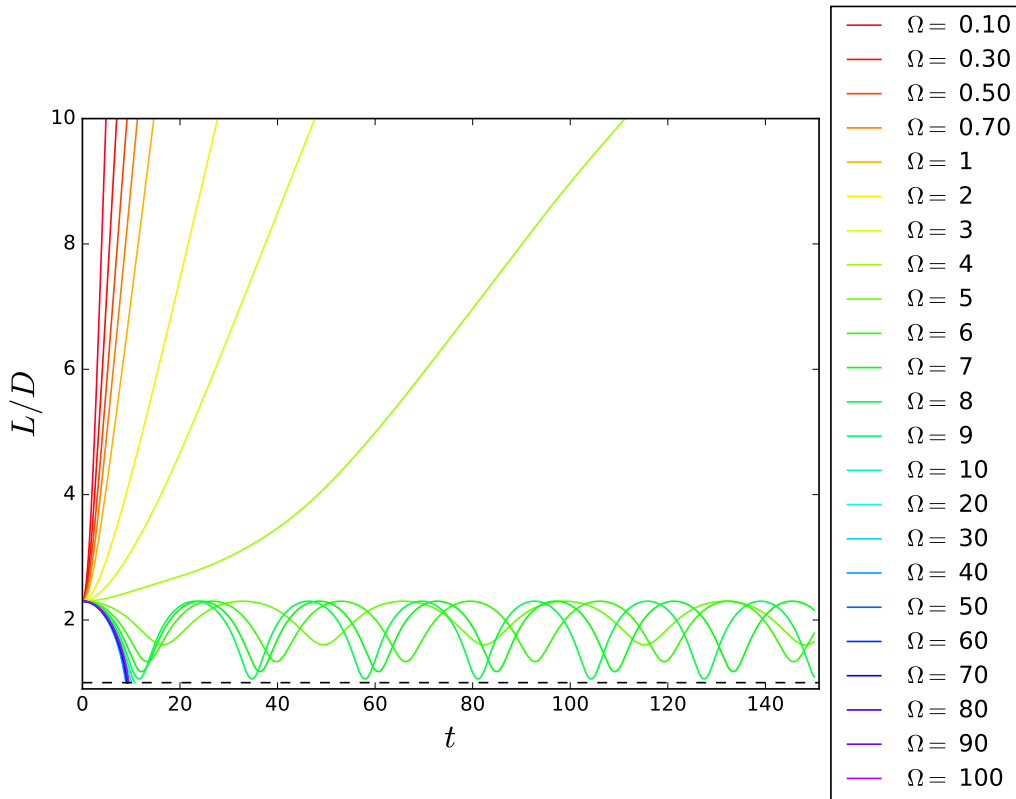


Figure 7.7: Trajectories of spheres over dimensionless time, t , for frequencies $0.10 \leq \Omega \leq 100$, when $L_0 = 2.3$ and $\theta_0 = \pi/2$ rad i.e. lateral configuration. The black horizontal dashed line shows $L/D = 1$. $L_0 = 2.3$ is equilibrium distance for $\Omega \approx 4$.

7.5 Summary

In this chapter, trajectories followed by two equal sized spheres were traced over a long time scale, when they were up to $20D$ apart, allowing them to move and sit at any angle relative to the applied oscillation. For the stable lateral configuration, attractive, repulsive and oscillatory behaviour of particles was found depending on the parameter Ω . Assuming that the flow fields calculated for motionless particles and the resulting forces are unaffected by the speed of the particle, $U_{Particle}$, spheres of size $\Omega \geq 10$

touch each other in as little as $5t_{MIN}$, where t_{MIN} is the time taken to reach the absolute minimum L_{MIN} for the given initial conditions. The effects of initial conditions for intermediate frequencies $5 \leq \Omega \leq 10$, that exhibit an oscillatory behaviour, have been investigated.

In the case of milk, MFGs are already as close as $2.3D$ apart, as calculated in section 7.4.2, it is deduced that the larger sized MFGs will align themselves in a lateral configuration and attract each other while the smaller sized spheres stay suspended in milk.

Since the condition of validity is relaxed, as discussed in section 7.3, the time it took for spheres to actually touch each other can not be considered directly applicable. According to this analysis, the particles take only $0.1\mu\text{s}$ to touch when a frequency of 1 MHz is applied. This time is order of a second shorter than the experiments performed by Leong *et al.* (2016). The calculation of trajectories that is valid over a wider range of parameters would require a completely different ‘fully coupled’ problem to be solved, where the particles are coupled with the fluid and are allowed to move when the fluid oscillates under the influence of the body force. This fully coupled problem is beyond the scope of this thesis, however, the results presented in section 7.4 demonstrate the interesting behaviour of particles owing to steady streaming.

Chapter 8

Conclusion

The research presented in this thesis is aimed at finding the role of steady streaming around spherical particles. It is found that steady streaming plays a positive part in making them come close to each other and eventually touch. This objective was achieved by applying numerical methods. Two numerical methods were employed to simulate steady streaming around spheres: a Direct Numerical Simulation (DNS), based on a spectral element method, and a Weakly Non-linear Formulation (WNF), based on a finite element method. Both DNS and WNF offer advantages over the other depending on the situation being simulated.

First, a single sphere problem is modelled and verified qualitatively and quantitatively against the literature using DNS, in **chapter 4**. Then, in **chapter 5**, the results using WNF and DNS are compared, qualitatively and quantitatively. For steady streaming around two spheres, a new problem is defined in **chapter 6** along with its set of parameters. WNF, based on a perturbation method, is used to obtain the results in three different configu-

rations, depending on the alignment of the spheres with respect to the axis of oscillation. Flow visualizations as well as the forces exerted on the spheres by steady streaming measured using the DNS and WNF are presented in **chapters 5 and 6**. Based on the forces thus calculated using WNF of the two sphere problem, trajectories followed by the spheres are computed in **chapter 7**, mainly to find out initial conditions that would lead the spheres to touch, and the time it takes.

For steady streaming around a single sphere in an oscillatory flow, results are produced for a range of parameters much wider than those studied previously. For high amplitudes $1 \leq \epsilon \leq 5$, DNS data shows presence of a different flow regime, as shown in Figure 5.7, that has not been discussed in the literature, to the best of our knowledge. DNS is also capable of capturing the non-symmetric nature of the sizes of the inner vortices, seen in Figure 5.8. However, DNS is limited to steady flows around a single sphere unless fully three-dimensional simulations are conducted, which is very expensive computationally.

The computational method WNF was verified with DNS for a single sphere to study forces and streaming flows around one and two spheres in an oscillating flow. In contrast to the DNS, the task of computing steady streaming flows around single and two spheres can be achieved quickly and economically using WNF. It has the added flexibility of imposing oscillations at any given angle to the axis on which the spheres are placed.

Using WNF, steady streaming has been studied around two spheres of equal size, placed at a distance L apart, for $0^\circ \leq \theta \leq 90^\circ$. Regimes, where two spheres can attract or repel each other, were discussed for three

particular configurations for $0.1 \leq \Omega \leq 100$, where the parameter Ω is defined as the Stokes number. This work is already published in the Journal of Fluid Mechanics (Fabre *et al.*, 2017). The Stokes number Ω is described as frequency here. However, Ω can also be seen as a parameter representing the size of the spheres. This means lower Ω represents small spheres, and larger Ω , large sized spheres. It was concluded that for high frequencies the spheres tend to re-align themselves in to the only stable configuration, i.e. lateral configuration, before attracting each other. This implies that in any situation with a non-uniform distribution of particles, that particles of larger sizes ($\Omega \geq 20$) will attract each other and, in the milk-separation application discussed in section 1.3, MFGs rise to form cream, whereas the smaller ones ($\Omega < 5$) will still remain suspended in milk. These results verify the conclusions of experiments conducted by Leong *et al.* (2016). Further applications of this work are mentioned in sections 1.3 and 2.4.

Following the steady streaming flows for a single sphere using WNF, it could be deduced where another sphere should be placed to experience repulsive or attractive force. This raised a question whether if performing a simulation for flows around two spheres is necessary. It was found that the flow around two spheres is not a simple superposition of two single spheres placed at a distance where net force experienced is zero i.e. a stagnation point.

The relative motion of two particles owing to the mutual induction of steady streaming has been calculated in a parameter range that has not been studied before. For the results presented, it was assumed that the flow fields are calculated for motionless particles and the resulting forces are unaffected

by the speed of the particle. Under this assumption, it was found that spheres of size (or frequency) $\Omega \geq 10$ touch each other, in a lateral configuration. All these results are ultimately applicable to the ultrasonic separation of Milk Fat Globules (MFGs), and other ultrasonic separation applications, and will be able to predict under what conditions these applications will work. Moreover, this work can be easily extended for spheres of different radii, and for ellipsoids and cylinders. With the assumption of validity for the numerical model developed to calculate the trajectories of particles being relaxed, the time it took for spheres to actually touch each other can not be strictly quantified. However, these results capture and demonstrate interesting inter-particle behaviour owing to steady streaming.

The numerical model involved for all the results presented so far involved many assumptions needed to make calculations tractable. It is found that a more detailed system needs to be simulated in the future, incorporating the fluid-particle coupling in order to take into account the complex phenomena happening between particles. In addition, there are phenomena that are known to further contribute to the role of steady streaming between particles. One such simplification is neglecting the multiple-scattering effects that are known to be significant when particles are placed at a distance comparable to their size (Crum, 1971). The rotation or spinning of spheres is also known to generate and contribute to steady streaming that has not been taken into account (Bestman, 1983). These inclusions would further strengthen the application of this work, which has demonstrated the influence of steady streaming in bringing particles to attract each other.

Bibliography

- ALASSAR, R. S. 2008 Acoustic streaming on spheres. *International Journal of Non-Linear Mechanics* **43** (9), 892–897.
- ALASSAR, R. S. & BADR, H. M. 1997 Oscillating viscous flow over a sphere. *Computers & Fluids* **26** (7), 661–682.
- BASSET, A. B. 1888 *A Treatise on Hydrodynamics*, vol. 2. Cambridge, England: Deighton, Bell and Co.
- BESTMAN, A. R. 1983 Low Reynolds number oscillatory flow past a slowly rotating sphere. *Zeitschrift für angewandte Mathematik und Physik ZAMP* **34** (6), 867–885.
- BJERKNES, V. F. K. 1906 *Fields of Force*. New York: Columbia University Press.
- BLACKBURN, H. M. 2002 Mass and momentum transport from a sphere in steady and oscillatory flows. *Physics of Fluids* **14** (11), 3997.
- BOSMA, R., VAN SPRONSEN, W. A., TRAMPER, J. & WIJFFELS, R. H. 2003 Ultrasound, a new separation technique to harvest microalgae. *Journal of Applied Phycology* **15** (2-3), 143–153.

- CHANG, E. J. & MAXEY, M. R. 1994 Unsteady flow about a sphere at low to moderate Reynolds number. Part 1. Oscillatory motion. *Journal of Fluid Mechanics* **277**, 347–379.
- CHLADNI, E. 1787 *Entdeckungen über die Theorie des Klanges (Discoveries on the theory of sound)*. Leipzig: Bey Weidmanns erben und Reich.
- COLLINS, D. J., MA, Z. & AI, Y. 2016 Highly localized acoustic streaming and size-selective submicrometer particle concentration using high frequency microscale focused acoustic fields. *Analytical Chemistry* **88** (10), 5513–5522.
- CRUM, L. A. 1971 Acoustic force on a liquid droplet in an acoustic stationary wave. *The Journal of the Acoustical Society of America* **50** (1B), 157–163.
- DAVIDSON, B. J. & RILEY, N. 1971 Cavitation microstreaming. *Journal of Sound and Vibration* **15** (2), 217–233.
- DIONNE, J. P., MCCARTHY, B., ROSS-JOHNSRUD, B., MASI, L. & LIPKENS, B. 2013 Large volume flow rate acoustophoretic phase separator for oil water emulsion splitting. *The Journal of the Acoustical Society of America* **133** (5), 3237–3237.
- DOINIKOV, A. A. 2003 Acoustic radiation forces: Classical theory and recent advances. In *Recent Research Developments in Acoustics*, pp. 39–67. Kerala, India: Transworld Research Network, Trivandrum.
- DOINIKOV, A. A. & ZAVTRAK, S. T. 1995 On the mutual interaction of two gas bubbles in a sound field. *Physics of Fluids* **7** (8), 1923–1930.

- DVOŘÁK, V. 1876 Ueber die akustische anziehung und abstossung (on the acoustic attraction and repulsion). *Annalen der Physik* **233** (1), 42–73.
- ECKART, C. 1948 Vortices and streams caused by sound waves. *Physical Review* **73** (1), 68–76.
- FABRE, D., JALAL, J., LEONTINI, J. S. & MANASSEH, R. 2017 Acoustic streaming and the induced forces between two spheres. *Journal of Fluid Mechanics* **810**, 378–391.
- FARADAY, M. 1831 On a peculiar class of acoustical figures; and on certain forms assumed by groups of particles upon vibrating elastic surfaces. *Philosophical Transactions of the Royal Society of London* **121**, 299–340.
- FLETCHER, C. A. J. 1984 *Computational Galerkin methods*. Springer.
- FRIEND, J. & YEO, L. Y. 2011 Microscale acoustofluidics: Microfluidics driven via acoustics and ultrasonics. *Reviews of Modern Physics* **83** (2), 647–704.
- GOR'KOV, L. P. 1962 On the forces on a small particle in an acoustical field in an ideal fluid. *Soviet Physics Doklady* **6** (9), 773–775.
- GRIFFITH, M. D., LEWEKE, T., THOMPSON, M. C. & HOURIGAN, K. 2009 Pulsatile flow in stenotic geometries: flow behaviour and stability. *Journal of Fluid Mechanics* **622** (August 2016), 291.
- GRIFFITH, M. D., SCHOUVEILER, L., THOMPSON, M. C. & HOURIGAN, K. 2011 Dynamics of the flow around colliding spheres. *Journal of Fluids and Structures* **27** (8), 1349 – 1356.

- HECHT, F. 2012 New development in freefem++. *Journal of Numerical Mathematics* **20** (3-4), 251–265.
- JOHANSSON, L., SINGH, T., LEONG, T., MAWSON, R., MCARTHUR, S., MANASSEH, R. & JULIANO, P. 2016 Cavitation and non-cavitation regime for large-scale ultrasonic standing wave particle separation systems – in situ gentle cavitation threshold determination and free radical related oxidation. *Ultrasonics Sonochemistry* **28**, 346 – 356.
- JULIANO, P., TEMMEL, S., ROUT, M., SWIERGON, P., MAWSON, R. & KNOERZER, K. 2013 Creaming enhancement in a liter scale ultrasonic reactor at selected transducer configurations and frequencies. *Ultrasonics Sonochemistry* **20** (1), 52 – 62.
- KARNIADAKIS, G. & SHERWIN, S. 2005 *Spectral/hp element methods for computational fluid dynamics*. Oxford University Press.
- KEENAN, T. W. & MATHER, I. H. 2006 Intracellular origin of milk fat globules and the nature of the milk fat globule membrane. In *Advanced Dairy Chemistry Volume 2 Lipids* (ed. P. F. Fox & P. L. H. McSweeney), pp. 137–171. Boston, MA: Springer US.
- KING, L. V. 1934 On the acoustic radiation pressure on spheres. *Proceedings of the Royal Society A: Mathematical, Physical and Engineering Sciences* **147** (861), 212–240.
- KLOTSA, D., SWIFT, M., BOWLEY, R. & KING, P. 2007 Interaction of spheres in oscillatory fluid flows. *Physical Review E* **76** (5), 056314.

- KLOTSA, K. D. 2009 The dynamics of spheres in oscillatory fluid flows. PhD thesis, University of Nottingham.
- KÖNIG, W. 1891 Hydrodynamisch-akustische untersuchungen. *Annalen der Physik* **278** (3), 353–370.
- KOBELEV, Y. A., OSTROVSKII, L. A. & SUTIN, A. M. 1979 Effect of self-clearing for acoustic waves in a liquid with gas bubbles. *Pis'ma v Zhurnal Éksperimental'noi i Teoreticheskoi Fiziki* **30**, 423–425.
- KOTAS, C. W., YODA, M. & ROGERS, P. H. 2006 Visualization of steady streaming near oscillating spheroids. *Experiments in Fluids* **42** (1), 111–121.
- LANE, C. A. 1955 Acoustical streaming in the vicinity of a sphere. *The Journal of the Acoustical Society of America* **27** (6), 1082.
- LEIGHTON, T. G. 1990 Primary Bjerknes forces. *European Journal of Physics* **11**, 47–50.
- LEONG, T., JOHANSSON, L., JULIANO, P., MAWSON, R., MCARTHUR, S. & MANASSEH, R. 2014 Design parameters for the separation of fat from natural whole milk in an ultrasonic litre-scale vessel. *Ultrasonics sonochemistry* **21** (4), 1289–98.
- LEONG, T., JOHANSSON, L., JULIANO, P., MCARTHUR, S. L. & MANASSEH, R. 2013 Ultrasonic separation of particulate fluids in small and large scale systems: A review. *Industrial and Engineering Chemistry Research* **52** (47), 16555–16576.

- LEONG, T., JOHANSSON, L., MAWSON, R., MCARTHUR, S. L., MANASSEH, R. & JULIANO, P. 2016 Ultrasonically enhanced fractionation of milk fat in a litre-scale prototype vessel. *Ultrasonics Sonochemistry* **28**, 118–29.
- LEONG, T., KNOERZER, K., TRUJILLO, F. J., JOHANSSON, L., MANASSEH, R., BARBOSA-CÁNOVAS, G. V. & JULIANO, P. 2015 Megasonic separation of food droplets and particles: Design considerations. *Food Engineering Reviews* **7** (3), 298–320.
- LIGHTHILL, S. J. 1978 Acoustic streaming. *Journal of Sound and Vibration* **61** (3), 391–418.
- LIGHTHILL, S. J. 1991 Biomechanics of hearing sensitivity. *Journal of Vibration and Acoustics* **113** (1), 1–13.
- LONGUET-HIGGINS, M. S. 1998 Viscous streaming from an oscillating spherical bubble. *Proceedings of the Royal Society A: Mathematical, Physical and Engineering Sciences* **454** (1970), 725–742.
- LYUBIMOV, D. V., BAYDIN, A. Y. & LYUBIMOVA, T. P. 2013 Particle dynamics in a fluid under high frequency vibrations of linear polarization. *Microgravity Science and Technology* **25** (2), 121–126.
- MAITZ, M., TRAMPLER, F., GRÖSCHL, M., D CÂMARA MACHADO, A. & L. D CÂMARA MACHADO, M. 2000 Use of an ultrasound cell retention system for the size fractionation of somatic embryos of woody species. *Plant Cell Reports* **19** (11), 1057–1063.

- MANASSEH, R. 2015 Acoustic Bubbles, Acoustic Streaming, and Cavitation Microstreaming. In *Handbook of Ultrasonics and Sonochemistry* (ed. Muthupandian Ashokkumar), pp. 1–36. Singapore: Springer.
- MANASSEH, R., MCARTHUR, S., MAWSON, R., JULIANO, P., JOHANSSON, L., LEONG, T. & JALAL, J. 2016 Ultrasonic separation of milk fat. Final steering committee report. Swinburne University of Technology and CSIRO Animal, Food and Health Sciences, Melbourne, Australia.
- MEI, C. C. 1985 Resonant reflection of surface water waves by periodic sandbars. *Journal of Fluid Mechanics* **152**, 315–335.
- MEISSNER, A. 1926 *Zeitschrift für technische Physik* **7**, 585.
- NYBORG, W. L. 1953 Acoustic streaming due to attenuated plane waves. *The Journal of the Acoustical Society of America* **25**, 68–75.
- OTTO, F., RIEGLER, E. K. & VOTH, G. A. 2008 Measurements of the steady streaming flow around oscillating spheres using three dimensional particle tracking velocimetry. *Physics of Fluids* **20** (9), 093304.
- PACHECO-MARTINEZ, H. A., LIAO, L., HILL, R. J. A., SWIFT, M. R. & BOWLEY, R. M. 2013 Spontaneous orbiting of two spheres levitated in a vibrated liquid. *Physical Review Letters* **110** (15), 154501.
- PANGU, G. D. & FEKE, D. L. 2007 Droplet transport and coalescence kinetics in emulsions subjected to acoustic fields. *Ultrasonics* **46** (4), 289–302.

- PETERSSON, F., NILSSON, A., HOLM, C., JONSSON, H. & LAURELL, T. 2004 Separation of lipids from blood utilizing ultrasonic standing waves in microfluidic channels. *The Analyst* **129** (10), 938–943.
- PUI, P. W. S., TRAMPLER, F., SONDERHOFF, S. A., GROESCHL, M., KILBURN, D. G. & PIRET, J. M. 1995 Batch and semicontinuous aggregation and sedimentation of hybridoma cells by acoustic resonance fields. *Biotechnology Progress* **11** (2), 146–152.
- RANEY, W. P., CORELLI, J. C. & WESTERVELT, P. J. 1954 Acoustical streaming in the vicinity of a cylinder. *The Journal of the Acoustical Society of America* **26** (6), 1006.
- RAYLEIGH, J. 1894 *The Theory of Sound*, vol. 1. London: Macmillan.
- RAYLEIGH, L. 1883 On the circulation of air observed in Kundt's tubes, and on some allied acoustical problems. *Philosophical Transactions of the Royal Society of London* **175**, 1–21.
- RILEY, N. 1966 On a sphere oscillating in a viscous fluid. *Quarterly Journal of Mechanics and Applied Mathematics* **19** (4), 461–472.
- RILEY, N. 1967 Oscillatory viscous flows. review and extension. *IMA Journal of Applied Mathematics* **3** (4), 419.
- RILEY, N. 1997 Acoustic Streaming. *Encyclopedia of Acoustics* **1**, 321–327.
- RILEY, N. 2001 Steady Streaming. *Annual Review of Fluid Mechanics* **33**, 43–65.

- SAADATMAND, M. & KAWAJI, M. 2010 Effect of viscosity on vibration-induced motion of a spherical particle suspended in a fluid cell. *Microgravity Science and Technology* **22** (3), 433–440.
- SAADATMAND, M. & KAWAJI, M. 2013 Mechanism of vibration-induced repulsion force on a particle in a viscous fluid cell. *Physical Review E, Statistical, Nonlinear, and Soft Matter Physics* **88** (2), 023019.
- SCHLICHTING, H. 1955 *Boundary-Layer Theory*. New York: McGraw-Hill.
- SEPEHRIRAHNAMA, S., CHAU, F. S. & LIM, K. 2016 Effects of viscosity and acoustic streaming on the interparticle radiation force between rigid spheres in a standing wave. *Physical Review E* **93** (2-1), 023307.
- SEPEHRIRAHNAMA, S., LIM, K. & CHAU, F. S. 2015 Numerical study of interparticle radiation force acting on rigid spheres in a standing wave. *Journal of the Acoustical Society of America* **137** (April 2014), 2614–2622.
- SIPP, D. & LEBEDEV, A. 2007 Global stability of base and mean flows: a general approach and its applications to cylinder and open cavity flows. *Journal of Fluid Mechanics* **593**, 333–358.
- SKUDRZYK, E. 1971 *The Foundation of Acoustics*. Springer-Verlag.
- STUART, J. T. 1966 Double boundary layers in oscillatory viscous flow. *Journal of Fluid Mechanics* **24** (4), 673–687.
- TABAKOVA, S. S. & ZAPRYANOV, Z. D. 1982 On the hydrodynamic interaction of two spheres oscillating in a viscous fluid. - I. Axisymmetrical

- case. *ZAMP Zeitschrift für angewandte Mathematik und Physik* **33** (3), 344–357.
- THO, P. 2005 Cavitation microstreaming in single and two bubble systems. PhD thesis, The University of Melbourne.
- THOMPSON, M., HOURIGAN, K. & SHERIDAN, J. 1996 Three-dimensional instabilities in the wake of a circular cylinder. *Experimental Thermal and Fluid Science* **12** (2), 190–196.
- TOWNSEND, R. J., HILL, M., HARRIS, N. R. & WHITE, N. M. 2004 Modelling of particle paths passing through an ultrasonic standing wave. *Ultrasonics* **42** (1-9), 319–24.
- TRUJILLO, F. J., JULIANO, P., BARBOSA-CÁNOVAS, G. & KNOERZER, K. 2014 Separation of suspensions and emulsions via ultrasonic standing waves - A review. *Ultrasonics Sonochemistry* **21** (6), 2151–64.
- VAN DYKE, M. 1982 *An Album of Fluid Motion*. Stanford, USA: Parabolic Press.
- VOTH, G., BIGGER, B., BUCKLEY, M., LOSERT, W., BRENNER, M., STONE, H. & GOLLUB, J. 2002 Ordered clusters and dynamical states of particles in a vibrated fluid. *Physical Review Letters* **88** (23), 234301.
- WALKER, J. P. & ALLEN, C. H. 1950 Sonic wind and static pressure in intense sound fields. *The Journal of the Acoustical Society of America* **22** (5), 680–681.

-
- WANG, C., JALIKOP, S. V. & HILGENFELDT, S. 2012 Efficient manipulation of microparticles in bubble streaming flows. *Biomicrofluidics* **6** (1), 12801–1280111.
- WIKLUND, M., GREEN, R. & OHLIN, M. 2012 Acoustofluidics 14: Applications of acoustic streaming in microfluidic devices. *Lab on a chip* **12** (14), 2438–51.
- WU, J. & DU, G. 1997 Streaming generated by a bubble in an ultrasound field. *The Journal of the Acoustical Society of America* **101** (4), 1899.
- XI, X. 2012 Controlled translation and oscillation of micro-bubbles near a surface in an acoustic standing wave field. PhD thesis, Imperial College London.
- YASUDA, K., UMEMURA, S. & TAKEDA, K. 1995 Concentration and fractionation of small particles in liquid by ultrasound. *Japanese Journal of Applied Physics* **34** (5S), 2715.
- YOSIOKA, K. & KAWASIMA, Y. 1955 Acoustic Radiation Pressure on a Compressive Sphere. *Acustica* **5**, 167–173.
- ZAREMBO, L. K. 1971 Acoustic streaming. In *High-Intensity Ultrasonic Fields* (ed. L. D. Rozenberg), pp. 135–199. New York: Plenum Press.
- ZAVTRAK, S. 1987 On the Bjerknes interaction force of two gas bubbles in a sound wave field. *Akusticheskii Zhurnal* **33**, 240–245.

Appendix

Estimate of motion of the sphere in an oscillatory field on the oscillation time scale

In section 7.2.2, displacement of the particle, X , is given as a function of ϵ ,

$$-X = \frac{3C_D\epsilon^2}{2m},$$

where X is the amplitude of the response of the sphere, m is the dimensionless mass, C_D is the drag force, and $\epsilon = A/D$. It is assumed that there is no coupling between the fluid and the sphere.

It is concluded that the amplitude response of the sphere is proportional to ϵ^2 . For WNF, $\epsilon \rightarrow 0$, thus, $X \rightarrow 0$, so this analysis is valid for WNF. For MFGs, mass ratio $0.75 \leq m \leq 1.00$ gives an amplitude response of $0.3D$ parallel to the imposed oscillation.

Proof: The force imposed is assumed to be $f_D = F_D \sin(\omega t)$ on the sphere induces an oscillatory motion

$$x = X \sin(\omega t + \phi). \tag{1}$$

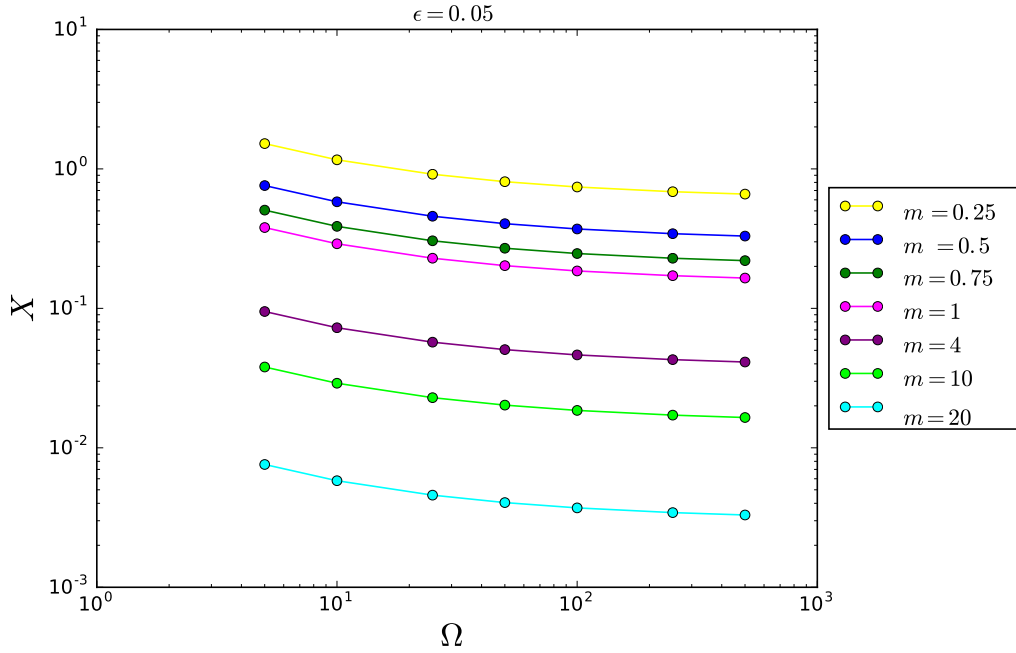


Figure 1: Vibration of particles, X , with mass ratio, m , when $\epsilon = 0.05$.

By Newton's second law of motion,

$$a = \frac{f_D}{m_b} \quad (2)$$

where m_b is the mass of the body. Using (1) for (2) and using f_D , we have

$$-X\omega^2 \sin(\omega t + \phi) = \frac{1}{m_b} F_D \sin(\omega t)$$

Comparing the coefficients,

$$\Rightarrow \phi = 0, \text{ and } -X\omega^2 = \frac{1}{m_b} F_D \quad (3)$$

Non-dimensionalization: We define

$$\Omega = \frac{\omega R^2}{\nu}, \quad X^* = \frac{X}{R}, \quad m = \frac{m_b}{m_f}, \quad \text{and} \quad C_D = \frac{F_D}{0.5\rho U_{max}^2 A_R} \quad (4)$$

where m_b and m_f are the mass of the body, and the fluid moved by it, respectively, A_R is the area of the sphere involved, and $U_{max} = A\omega$. From equations (4), we have

$$\omega = \frac{\Omega\nu}{R^2}, \quad F_D = 0.5C_D\rho U_{max}^2 A_R, \quad \text{and} \quad m_b = mm_f \quad (5)$$

where $m_f = 4/3\rho\pi R^3$. Substituting equation (5) in equation (3), we get

$$\begin{aligned} (X^*R)\left(\frac{\Omega^2\nu^2}{R^4}\right) &= \frac{C_D 0.5\rho A^2 \omega^2 \pi R^2}{4/3m\rho\pi R^3} \\ \Rightarrow -X &= \frac{0.5C_D A^2}{4/3mR^2} \end{aligned}$$

Since $\epsilon = \frac{A}{D}$, so

$$\Rightarrow -X = \frac{3C_D\epsilon^2}{2m}. \quad (6)$$

Copyright Permissions Sought for Images Used

Order Summary of Copyrights for Figure 2.1

Licensee: Swinburne University of Technology

Order Date: Feb 23, 2018

License Number: 4295051046788

Publication: Proceedings A

Title: Viscous streaming from an oscillating spherical bubble

Type of Use: Thesis/Dissertation

Order Ref: Thesis_Higgins

Order Total: 4.20 USD

Order Summary of Copyrights for Figure 2.2

Licensee: Swinburne University of Technology

Order Date: Feb 23, 2018

License Number: 4295031504093

Publication: The Journal of the Acoustical Society of America

Title: Acoustical Streaming in the Vicinity of a Sphere

Type of Use: Thesis/Dissertation

Order Ref: Thesis-Lane

Order Total: 0.00 USD

Order Summary of Copyrights for Figure 2.3

Licensee: Swinburne University of Technology

Order Date: Feb 23, 2018

License Number: 4295031338773

Publication: The Quarterly Journal of Mechanics and Applied Mathematics

Title: ON A SPHERE OSCILLATING IN A VISCOUS FLUID

Type of Use: Thesis/Dissertation

Order Ref: Thesis permissions

Order Total: 0.00 AUD

Order Summary of Copyrights for Figure 2.4

Licensee: Swinburne University of Technology

Order Date: Feb 23, 2018

License Number: 4295040571485

Publication: Experiments in Fluids

Title: Visualization of steady streaming near oscillating spheroids

Type of Use: Thesis/Dissertation

Order Ref: Thesis_Kotas

Order Total: 0.00 USD

Order Summary of Copyrights for Figure 4.5

Licensee: Swinburne University of Technology

Order Date: Feb 23, 2018

License Number: 4295040997693

Publication: International Journal of Non-Linear Mechanics

Title: Acoustic streaming on spheres

Type of Use: reuse in a thesis/dissertation

Order Ref: **Thesis-Alassar**

Order Total: 0.00 USD

List of Publications

The following papers have been published as a result of this research:

FABRE, D., JALAL, J., LEONTINI, J. S. & MANASSEH, R. 2017 Acoustic streaming and the induced forces between two spheres. *Journal of Fluid Mechanics* **810**, 378–391.

JALAL, J., LEONTINI, J. S., FABRE, D. & MANASSEH, R. 2016 Effects of forces induced by steady streaming flows on rigid oscillating spheres, at *20th Australasian Fluid Mechanics Conference (AFMC), Perth, Dec 5 - 8, 2016*.

The following presentation has been given at a conference:

JALAL, J., LEONTINI, J. S., JOHANSSON, L. & MANASSEH, R. 2015 Streaming flows around oscillating spheres, at *3rd Symposium on Fluid-Structure-Sound Interactions and Control (FSSIC), Perth, 5 - 9 July, 2015*.